POLITECNICO DI MILANO

Department of Civil and Environmental Engineering
Doctoral School in Structural, Seismic and Geotechnical Engineering

Micromechanical characterization of polysilicon films: on-chip testing, multi-uncertainty quantification and Bayesian inverse modelling

Supervisors

Stefano Mariani
Aldo F. Ghisi
Eelco L. Jansen

PhD Candidate

Ramin Mirzazadeh

March 2017

Ramin Mirzazadeh
Micromechanical characterization of polysilicon films: on-chip testing, multi-uncertainty quantification and Bayesian inverse modelling
© March 2017

e-mail:
ramin.mirzazadeh@polimi.it

Micromechanical characterization of polysilicon films: on-chip testing, multi-uncertainty quantification and Bayesian inverse modelling

A Thesis
Presented to
The Academic Faculty

by

Ramin Mirzazadeh

In Partial Fulfillment
of the Requirements for the Degree
Doctor of Philosophy
in
Structural, Seismic and Geotechnical Engineering

March 2017

page intentionally left blank

Doctoral School in Structural, Seismic and Geotechnical Engineering
Department of Civil and Environmental Engineering
Politecnico di Milano

XXIX cycle

Faculty Members

Prof. Roberto Paolucci (Coordinator)
Prof. Raffaele Ardito
Prof. Patrick Bamonte
Prof. Fabio Biondini
Prof. Gabriella Bolzon
Prof. Matteo Bruggi
Prof. Claudia Comi
Prof. Alberto Corigliano
Prof. Dario Coronelli
Prof. Gabriele Della Vecchia
Prof. Claudio di Prisco
Prof. Marco di Prisco
Prof. Roberto Fedele
Prof. Roberto Felicetti
Prof. Liberato Ferrara
Prof. Attilio Frangi
Prof. Elsa Garavaglia
Prof. Aldo Ghisi
Prof. Pier Giorgio Malerba
Prof. Stefano Mariani
Prof. Luca Martinelli
Prof. Umberto Perego
Prof. Lorenza Petrini
Prof. Luigi Zanzi

page intentionally left blank

To my loved ones:

O friend, for the morrow let us not worry
This moment we have now, let us not hurry
When our time comes, we shall not tarry
With seven thousand-year-olds, our burden carry.

— *Omar Khayyam (1048-1131)*

page intentionally left blank

Abstract

Novel applications of MEMS technology require devices featuring smaller dimensions. When the dimensions of polycrystalline structures become comparable to the average grain size or to the fabrication inaccuracies, issues related system performance can be reported for the inertial MEMS. Not only the overall behaviour of the device turns out to be affected by a large scattering, but also the sensitivity to imperfections is increased. In this work, a comprehensive study of the physics underlying system performance at the micro scale is provided. To this aim, a set of MEMS test devices is fabricated, and the results are analyzed by means of both analytical and numerical approaches.

The designed experimental campaign is consisted of several on-chip test devices realized by means of common microfabrication techniques. The main goal of these devices is to investigate the apparent mechanical properties of a polysilicon micro beam as the fundamental structural component of MEMS applications. The micro beams feature a width of 2 μm which accommodates, in average, only 3-4 silicon grains. Actuation and sensing are realized using standard electrostatic methods, similar to those in the commercial applications. The electromechanical responses of several devices have been recorded showing relatively large scatterings, despite their nominally identical specifications. Such observation can be due to the differences i) in the material properties of the beams due to their microstructure (polysilicon morphology), or ii) in the device geometry originated from fabrication inaccuracies.

In order to investigate the effects of the variations of material properties, Monte Carlo simulations are employed, taking into account the polysilicon random morphology. The results of these simulations demonstrate some degree of dependency of the electromechanical response on the polysilicon film properties, but they also show that the large scatterings cannot be explained on material properties ground only; the fabrication inaccuracies have a key role in the experimentally observed scatterings.

Taking into account both material properties variations and fabrication inaccuracies, parametric analytical/numerical models are henceforth provided for the test devices. Dealing with the unknown parameters of the models as deterministic or stochastic variables, several parameter estimation techniques are adopted in this work, including Levenberg Marquardt, genetic algorithm, particle filtering and transitional Markov chain Monte Carlo (TMCMC). Based on the experimental measurements, the unknown parameters are successfully estimated for each specimen.

Finally, a non-intrusive computation reduction method coupled with the TMCMC is used for Bayesian inverse modelling and uncertainty quantification for this specific test device. The proposed computation reduction method is a synergy between the proper orthogonal decomposition (POD) and the kriging metamodelling. This method constructs a reduced model of a finite element one at a very low computational effort and high accuracy level, while the TMCMC is a stochastic method that takes the measurements error into account and provides, not the value of the unknown parameter, but its probability distribution. The successful applicability of this method is shown for the actual measurements of the MEMS test device.

Acknowledgements

I would like to express my sincerest appreciation and gratitude to my Ph.D. advisor Dr. Stefano Mariani, for supporting me during these years. I have learnt and benefited from his scientific excellence and disciplined work attitude. I appreciate his warm encouragements, insightful guidance, time and funding as well as the freedom to explore different research paths that made this work possible.

I am grateful to Dr. Aldo Ghisi for his practical and helpful comments. He has been incredibility patient and helpful every time I came up with a question. I would like to thank Dr. Eelco Jansen who kindly facilitated my stay at Leibniz Universität Hannover. I appreciate his remarks and constructive discussions which have helped to improve this thesis. The contributions of my friend and colleague Dr. Saeed Eftekhar Azam to this work have had a great impact. I have extensively benefited from his deep knowledge and fruitful advice.

My Ph.D. has been supported by the scholarship offered by the "ministry of education, universities and research" (MIUR) of Italy; therefore, I would like to express my gratitude for the generosity of this country and its people.

These years have been full of joyful moments thanks to the amazing people I have been lucky to enjoy their company; Kiana, La Volterra Bella (Mari, Deborah e Eleonora), Gio, Rakesh, Yashar, Sara, Filippo, Ben, Mehrdad, Sahand, Lola, Gianluca, Natasha, Giovanna, Estefania, Andrea, Silvia, Francesco L., Valentina, Patrick, Luca, Simone, Grigor, Martina, Elisa, Mariana, Bruno, Francesco F., Visar and many others. Many thanks to Nidaba Theatre; even clocks there tick with the music rhythm. I am so glad that I did my research stay at Hannover, mostly because of the opportunity to meet a handful of friendly people; Roozbeh, Mehdi, Sander, Stavroula, Ayan, Omid, Abtin and Lorenzo. I also need to thank Amelie Fau and Matteo Broggi for their recommendations on reduced order modelling techniques and on how to properly watch Euro 2016 games.

I am a lucky man since I have loved ones, though physically far, yet always reachable to share my joy or distress; Larissa for her patience and endless love, Shahin for his genuine care and fine spirit, Mike for his contagious joyful attitude, Omid for his extremely kind and pure friendship and Mohammad for his never ending encouragements. We will finally end up somewhere together.

My parents are the ones who have been always there for me. My words cannot express how grateful I am to them. I wish I could be somehow close to who they want me to become.

page intentionally left blank

Contents

1 Introduction **1**
1.1 Background and motivation 1
1.2 Objectives and scope 2
1.3 Organization of the thesis 6

2 MEMS and uncertainties **9**
2.1 Introduction 9
2.2 MEMS and microfabrication 9
2.2.1 ThELMA process 11
2.3 Polysilicon elastic properties 14
2.3.1 Single crystalline silicon properties 14
2.3.2 Polycrystalline silicon properties 17
2.4 Sources of uncertainties 20
2.5 Micromechanical characterization methods 23
2.5.1 Tension tests 24
2.5.2 Bending tests 25
2.5.3 Torsional tests 27
2.5.4 Nanoindentation tests 28
2.5.5 Sensitivity Built-In Self-Tests 29
2.6 Remarks 30

3 Experimental campaign using on-chip testing **33**
3.1 Introduction 33
3.2 Test device 34
3.3 Testing set-up 37
3.4 Experimental measurements 40
3.5 Remarks 43

4 Modelling the test device **45**
4.1 Introduction 45
4.1.1 Material model 46
4.2 Analytical modelling 47
4.2.1 Mechanical field 47
4.2.2 Electrical field 52
4.3 Finite element modelling 55
4.4 Results 59

5 Mechanically induced uncertainties on the experimental measurements 63
5.1 Introduction 63
5.2 Admissible elastic properties 64
5.3 Mechanical bounds on the measurement scattering 65
5.4 MC simulation of elastic properties 68
5.4.1 Mechanical properties variations due to the microstructure 68
5.4.2 Convergence of Monte Carlo simulation 72
5.4.3 Results 74
5.5 Concluding remarks 86

6 On-line parameter estimation: particle filter 87
6.1 Introduction 87
6.2 Recursive Bayesian inference 88
6.3 Particle filtering 91
6.4 Parameter estimation: Results 94

7 Off-line parameter estimations 105
7.1 Introduction 105
7.2 Levenberg-Marquardt algorithm 106
7.3 Genetic algorithms 108
7.4 Discussion on the results 109

8 POD-kriging TMCMC 119
8.1 Introduction 119
8.2 Methods for computational reduction 121
8.3 Model order reduction: proper orthogonal decomposition 124
8.4 Kriging metamodel 128
8.5 POD-kriging method for model order reduction 132
8.5.1 Sampling strategy 135
8.6 Transitional Markov chain Monte Carlo simulation 137
8.7 POD-kriging TMCMC: Application to electromechanical problem . 145

9 Conclusions 157
9.1 Summary of contributions 157
9.2 Suggestions for future research 160

References 163

List of Figures

2.1 Fabrication steps in the ThELMA process. From [Fachin, 2007]. . . 12

2.2 Miller Indices in a cubic crystal. By convention, the directions [100], [010] and [001] are the xyz Cartesian axes. From [Hopcroft et al., 2010]. 15

2.3 Variation of linear elastic parameters versus orientation in the silicon crystal for (100) plane using the coefficients reported in Table 2.1. (**a**) Young's modulus, and (**b**) Poisson's ratio. 16

2.4 Global and local reference frame. 17

2.5 Digital realization of epitaxial polysilicon with identical out-of-plane axis and random in-plane orientation. 18

2.6 Morphology samples of polysilicon inside specimens. (**a**) Specimen with relatively high number of grains, and (**b**) specimen with relatively low number of grains. 21

2.7 A tension test configuration taken from [Corigliano et al., 2010]. The actuator beams expand in their length as they are heated by the electric current, to pull the specimen, and the induced elongation in the specimen is detected at the capacitive sensors. 25

2.8 Examples of bending test layouts: micro beam test using either (**a**) cantilever or (**b**) clamped-clamped beam, (**c**) bulge test, and (**d**) M-test. From [Pantano et al., 2012]. 26

2.9 On-chip testing device for in-plane bending configuration using rotational actuators. (**a**) General view, and (**b**) details of the bending specimen. From [Corigliano et al., 2005]. 27

2.10 Schematic diagram of a torsion test apparatus. From [Liu et al., 2012]. 28

2.11 Examples of basic BIST mechanisms used for testing the functionality of accelorometers. (**a**) Piezoresistive accelerometer, and (**b**) capacitive accelerometer. From [Mir et al., 2006]. 30

3.1 Schematic view of the specimen (not to scale). 35

3.2 (**a**) Device geometry with (**b**) details of the beam region and (**c**) in proximity of the lateral stator for beam length equal to 20 μm. . . 35

3.3 Beam region for beam length equal to 10 μm. 36

3.4 Test setup for $C-V$ measurement. 37

3.5 Details of the experimental setup for using (**a**) the same capacitors, or (**b**) different capacitors for actuation and sensing. 38

3.6 Experimental configurations: (**a**) RR (rotational actuation, rotational sensing), (**b**) RL (rotational actuation, lateral sensing), (**c**) LR (lateral actuation, rotational sensing), (**d**) LL (lateral actuation and sensing). 39
3.7 Experimental results for the device with beam length equal to 20 μm: (**a**) RR (rotational actuation, rotational sensing), (**b**) RL (rotational actuation, lateral sensing). 40
3.8 Experimental results for the device with beam length equal to 20 μm: (**a**) LR (lateral actuation, rotational sensing), (**b**) LL (lateral actuation and sensing). 41
3.9 Experimental results for the device with beam length equal to 10 μm:(a) RR (rotational actuation, rotational sensing), (b) RL (rotational actuation, lateral sensing). 42
3.10 Experimental results for the device with beam length equal to 10 μm: (**a**) LR (lateral actuation, rotational sensing), (**b**) LL (lateral actuation and sensing). 42

4.1 Deformation of a typical transverse normal line in Euler-Bernoulli and Timoshenko beam theories. u^E and u^T denote the transverse deflection (along z direction) of the beam neutral axis in Euler-Bernoulli and Timoshenko beam therories, respectively. 49
4.2 (**a**) Schematic of the behaviour of the whole test structure in the case of lateral actuation, and (**b**) close-up of the deflected micro beam. 51
4.3 (**a**) Layout of the specimen and, (**b**) Voronoi artificial tessellation used to reconstruct the micro beam polysilicon morphology, and (magnified) example of the grain morphology in the micro beam region. 56
4.4 (**a**) Adopted model of the geometry and (**b**) a random grain morphology in the micro beam region. 57
4.5 (**a**) FE discretization and (**b**) detail of the mesh in the micro beam region, accounting for random grain morphology. 58
4.6 Experimental measurements versus results of numerical and analytical model for specimen with beam length equal to 20 μm: (**a**) RR (rotational actuation, rotational sensing), (**b**) RL (rotational actuation and lateral sensing). 61
4.7 Experimental measurements versus results of numerical and analytical model for specimen with beam length equal to 20 μm: (**a**) LR (lateral actuation, rotational sensing), (**b**) LL (lateral actuation and lateral sensing). 61

4.8 Experimental measurements versus results of numerical and analytical model for specimen with beam length equal to 10 μm: (**a**) RR (rotational actuation, rotational sensing), (**b**) RL (rotational actuation and lateral sensing). 62
4.9 Experimental measurements versus results of numerical and analytical model for specimen with beam length equal to 10 μm: (**a**) LR (lateral actuation, rotational sensing), (**b**) LL (lateral actuation and lateral sensing). 62

5.1 Experimental responses in terms of capacitance change and acutation voltage vs numerical bounds obtained by using maximum, minimum and homogenized values of E and relevant ν for the devices whose beam length is equal to 20 μm: (**a**) RR, (**b**) RL. . . . 66
5.2 Experimental responses in terms of capacitance change and acutation voltage vs numerical bounds obtained by using maximum, minimum and homogenized values of E and relevant ν for the devices whose beam length is equal to 20 μm: (**a**) LR, (**b**) LL. 67
5.3 Experimental responses in terms of capacitance change and acutation voltage vs numerical bounds obtained by using maximum, minimum and homogenized values of E and relevant ν for the devices whose beam length is equal to 10 μm: (**a**) RR, (**b**) RL. . . . 67
5.4 Experimental responses in terms of capacitance change and acutation voltage vs numerical bounds obtained by using maximum, minimum and homogenized values of E and relevant ν for the devices whose beam length is equal to 10 μm: (**a**) LR, (**b**) LL. 68
5.5 Examples of 2 μm $\times$ 2 μm SVEs of polysilicon used in the preliminary MC simulations. 70
5.6 Fluctuations of the elastic properties of the SVE due to the polysilicon morphology: (**a**) Young's modulus E, and (**b**) shear modulus G. Blue lines correspond to the uniform strain BCs and orange lines correspond to the uniform stress BCs. Continuous lines show the CDFs of the MC FE simulations; dashed lines represent the lognormal distribution fits to the corresponding data. 71
5.7 Dependence of the mean value of the capacitance change at V_{ref} on the number of simulations in the MC FE analysis. 73
5.8 MC FE method versus experimental results for rotational actuation and sensing through V_R: (**a**) electromechanical response at varying voltage, and (**b**) capacitance change for V_R=37 V; continuous line corresponds the MC FE method; diamond symbols stand for experimental responses. 75

5.9 Comparisons between analytical, numerical and experimental results for the device featuring the 20 μm-length beam in the RR configuration. (**a**) 25%, (**b**) 50%, (**c**) 75%, (**d**) 100% of the reference maximum voltage $V_{\text{ref}} = 37$ V. 76
5.10 Comparisons between analytical, numerical and experimental results for the device featuring the 20 μm-length beam in the RL configuration. (**a**) 25%, (**b**) 50%, (**c**) 75%, (**d**) 100% of the reference maximum voltage $V_{\text{ref}} = 37$ V. 77
5.11 Comparisons between analytical, numerical and experimental results for the device featuring the 20 μm-length beam in the LR configuration. (**a**) 25%, (**b**) 50%, (**c**) 75%, (**d**) 100% of the reference maximum voltage $V_{\text{ref}} = 15.5$ V. 78
5.12 Comparisons between analytical, numerical and experimental results for the device featuring the 20 μm-length beam in the LL configuration. (**a**) 25%, (**b**) 50%, (**c**) 75%, (**d**) 100% of the reference maximum voltage $V_{\text{ref}} = 15.5$ V. 79
5.13 Comparisons between analytical, numerical and experimental results for the device featuring the 10 μm-length beam in the RR configuration. (**a**) 25%, (**b**) 50%, (**c**) 75%, (**d**) 100% of the reference maximum voltage $V_{\text{ref}} = 40$ V. 80
5.14 Comparisons between analytical, numerical and experimental results for the device featuring the 10 μm-length beam in the RL configuration. (**a**) 25%, (**b**) 50%, (**c**) 75%, (**d**) 100% of the reference maximum voltage $V_{\text{ref}} = 40$ V. 81
5.15 Comparisons between analytical, numerical and experimental results for the device featuring the 10 μm-length beam in the LR configuration. (**a**) 25%, (**b**) 50%, (**c**) 75%, (**d**) 100% of the reference maximum voltage $V_{\text{ref}} = 22.5$ V. 82
5.16 Comparisons between analytical, numerical and experimental results for the device featuring the 10 μm-length beam in the LL configuration. (**a**) 25%, (**b**) 50%, (**c**) 75%, (**d**) 100% of the reference maximum voltage $V_{\text{ref}} = 22.5$ V. 83
5.17 Ratio between standard deviations of MC FE model and that of the measured data for the different experimental configurations. . . 85

6.1 Sensitivity of the pull-in voltages V_R^{pull} and V_L^{pull} to a variation of (left) over-etch O, or (right) polysilicon Young's modulus E. 95
6.2 Comparison between the electromechanical responses of two devices respectively featuring $O_1 = -0.15$ μm (solid line) and $O_2 = 0.15$ μm (dashed line), with $E_1 = E_2 = \bar{E}$. 96

6.3 Evolution of the estimates of (top) O and (bottom) E, at varying filter initialization. Blue dashed lines: rotational actuation through V_R; orange solid lines: lateral actuation through V_L. (**a**) Specimen #2, leading to consistent final estimates, and (**b**) specimen #5, leading instead to non-consistent results. 97
6.4 Specimen #2, rotational actuation case, $\xi_O = \xi_E = 0.75$: evolution of the PDFs of (**a**) O and (**b**) E corresponding to the evolution of estimates represented by blue curves in Figure 6.3(a). 99
6.5 Specimen #2, lateral actuation case, $\xi_O = \xi_E = 0.75$: evolution of the PDFs of (**a**) O and (**b**) E corresponding to the evolution of estimates represented by orange curves in Figure 6.3(a). 100
6.6 Specimen #5, rotational actuation case, $\xi_O = \xi_E = 0.75$: evolution of the PDFs of (**a**) O and (**b**) E corresponding to the evolution of estimates represented by blue curves in Figure 6.3(b). 101
6.7 Specimen #5, lateral actuation case, $\xi_O = \xi_E = 0.75$: evolution of the PDFs of (**a**) O and (**b**) E corresponding to the evolution of estimates represented by orange curves in Figure 6.3(b). 102

7.1 Initial offset displacement parametrized by u_0 and θ_0. Displacements not to scale. 110
7.2 RR case, V_R =37 V, variation of the device response at varying (**a**) overetch O, (**b**) Young's modulus E and (**c**) rotation offset θ_0. . . . 112
7.3 LL case, V_L =15 V, variation of the device response at varying (**a**) overetch O, (**b**) Young's modulus E and (**c**) rotation offset θ_0. . . . 113
7.4 Effect of initialization on the estimated parameters: (**a**) Overetch O, (**b**) Young's modulus E and (**c**) rotation offset θ_0. 115
7.5 (**a**) Convergence of the objective discrepancy function at increasing generations, and (**b**) close-up of the plot and best score trend. . . . 116

8.1 Flow chart of operations to be performed in a POD-kriging procedure with k number of unknown parameters, n number of snapshot (FE simulation based on predefined parameters) and m number of output quantities from FE model (discretized response curve). . . . 134
8.2 Ilustration of Clenshaw-Crutis sample points distribution in the case (**a**) of two dimensional, and (**b**) of three dimensional problem. 138
8.3 Ilustration of Chebyshev sample points distribution in the case (**a**) of two dimensional, and (**b**) of three dimensional problem. 139
8.4 Ilustration of verification points (red circles) along the (**a**) Clenshaw-Crutis, and (**b**) Chebyshev sample points distribution (black dots). 146

8.5 Comparison between the output of direct FE model and its POD-kriging approximation using two different sparse grids; Clenshaw-Curtis (CC) and Chebyshev (Cheb). 147
8.6 Comparison between a FE model output and its POD representation by the first two prevailing modes. 148
8.7 TMCMC samples generated from the prior (left hand side) and posterior (right hand side) PDF of (**a**) RR case, and (**b**) LL case for the specimen #2. 150
8.8 Contour plot of the posterior PDF and corresponding histograms of (**a**) RR case, and (**b**) LL case for the specimen #2. 151
8.9 Comparison between the measured response of specimen #2 and model response using the estimated parameters by TMCMC for (**a**) RR case, and (**b**) LL case. 152
8.10 TMCMC samples generated from the prior (left hand side) and posterior (right hand side) PDF of (**a**) RR case, and (**b**) LL case for the specimen #5. 153
8.11 Contour plot of the posterior PDF and corresponding histograms of (**a**) RR case, and (**b**) LL case for the specimen #5. 154
8.12 Comparison between the measured response of specimen #5 and model response using the estimated parameters by TMCMC for (**a**) RR case, and (**b**) LL case. 155

List of Tables

2.1 Elastic constants of silicon at room temperature [Brantley, 1973]. . . 16

3.1 Geometric dimensions of the device. 34

5.1 Elastic constants for comparison cases. 65
5.2 Estimated distribution for E and G via MC simulations of a 2×2 $(\mu\text{m})^2$ SVE. 72

6.1 Estimated parameter values through particle filtering. 103

7.1 Estimated parameters values through GA. 117

8.1 Number of sampling points by Smolyak algorithm at different dimensions. 137

page intentionally left blank

1
Introduction

1.1 Background and motivation

The advances in the field of integrated circuits and semiconductors in the past decades not only affected the electronics industry, but also had a direct impact on the emergence of a wide range of micro-sized devices which we know today as microelectromechanical systems (MEMS) [Gad-el Hak, 2001]. They greatly benefit from their small size, short time response, low energy consumption and low cost due to their mass production techniques. Combining the electronic and structural components, MEMS have been outperforming the conventional technologies at a variety of engineering applications like accelerometers, magnetometers, scanners, pressure sensors and gyroscopes [Hsu, 2008, Choudhary and Iniewski, 2013].

Due to the ever increasing concerns on economical efficiency, environmental policies and sustainability, there is a great demand for novel sensing solutions (e.g. low cost and low energy consumption). These incentives have led to additional attention to the potentials of the MEMS applications while imposing stricter design constraints, such as smaller dimensions, elevated signal-to-noise ratio and lower energy consumption. To address the aforementioned issues, a greater push towards ever smaller and novel MEMS devices, featuring innovative fabrication processes and new materials, is necessary. However, the success of these MEMS devices critically hinges on how reliable and predictable their performance is [Brand et al.,

2013].

While these devices offer great potentials, their small dimensions set new challenges which one does not usually encounter at the macro-size applications. The miniaturization of the mechanical components may intensify uncertainty issues on the system performance linked to the *mechanical* or *geometric* properties of the final fabricated devices [Brand et al., 2013]. The small dimensions of miniaturized devices can be in fact on the same order of fabrication tolerances or the characteristic length of material heterogeneities (grain size, for instance). Therefore, improvement of our understanding on the devices' operational performance is always needed to design innovative devices [Pantano et al., 2012].

The mentioned issues show the importance of the fundamental understanding of the physics of MEMS performance in the development of ever smaller devices to meet the current industry expectations. For this study, experimental methods are indispensable. Moreover, correct interpretation of experiments requires a thorough understanding of the underlying theory and therefore they have to be combined with calculations and analytical forecasting, possibly in a stochastic framework.

1.2 Objectives and scope

The main objective of this work is to address the issues related to the performance of MEMS devices when their designed dimensions are decreased. This objective is met by studying the sources of mechanical uncertainties in MEMS thin films response through the comparison between experimental tests (with an ad hoc developed test device) and analytical/numerical simulations, accounting also for effective parameters estimation techniques. The uncertainties considered here in this work are collected in two broad groups:

- **a)** material related, i.e. linked to the intrinsic heterogeneity of the material;
- **b)** geometric, i.e. due to the limits of the production process, such as tolerances.

The plan is to study these uncertainties when the the desired dimensions of the MEMS components are comparable to the material intrinsic length scale (e.g.

grain size) or to the scale of the fabrication inaccuracies (e.g. fabrication tolerances).

Experimental investigations are first carried out by adopting MEMS test devices which feature miniaturized components (on the order of 2 μm). These designed test devices are fabricated using polycrystalline silicon (polysilicon), which is currently one of the most common materials (along with mono crystalline silicon) in the MEMS technology. The experimental set-up performs bending tests on micro cantilever-like specimens featuring two different lengths. The emphasis is put on the simplicity of the device and on conventional actuation/sensing techniques to simulate commercial MEMS. Different testing configurations (under alternative loading methods) are devised to provide data redundancy, which is useful for validation purposes. The device allows to study uncertainties related either to the material properties variations or to the fabrication inaccuracies. The experimental results, in terms of electromechanical responses of the devices, are presented for two micro beam lengths to explore the effect of geometry on the measurements. Due to the presence of the aforementioned uncertainty sources, experimental responses are not identical, though the specimens for each beam length are nominally identical. These observations yield experimental evidence on the significant effects of uncertainty sources on the operational performance of MEMS devices when their components are miniaturized (to the same order of fabrication tolerances or the characteristic length of the material heterogeneities).

As far as material related uncertainties are concerned (i.e. uncertainties linked to the intrinsic heterogeneity of the material), an investigation is conducted on the possible effects of polysilicon elastic properties variation on the experimental measurements. First, bilateral bounds on the electromechanical responses are calculated using the maximum variations of polysilicon elastic properties. Then, in a more detailed statistical study, two sets of Monte Carlo (MC) simulations are carried out using either a finite element (FE) model or an analytical model. In the former, the variations in polysilicon morphology are explicitly modelled to be used in the MC simulations. In the latter, a preliminary study is done on a set of statistical volume elements (SVEs) of polysilicon to calculate the probability density functions (PDFs) of their elastic properties. These PDFs are then fed into the MC simulations using the analytical model. The results of these two sets

of MC simulations are presented for the two specimen lengths allowing only for material properties variation and compared to the experimental measurements. Through this study, it is observed that the uncertainties due to the material properties variations intensify in the smaller specimens; relevant MEMS performance issues may arise as the dimensions of their components shrink. Similar experimental evidences at scales comparable to the considered polysilicon grain size have been only reported in works of another team [Cho and Chasiotis, 2007, Cho et al., 2005] that, unlike the present on-chip method, uses digital image correlation (DIC) analysis of atomic force microscopy (AFM) to measure displacement field, developed in their samples.

The relevant geometric inaccuracies of the test device (i.e. due to the limits of the production process) are taken into account, instead, through analytical or numerical models. Dealing with unknown parameters as deterministic or stochastic variables, several parameter estimation methods are adopted in this work, including Levenberg Marquardt algorithm, genetic algorithm, particle filtering and transitional Markov chain Monte Carlo (TMCMC) method. These methods offer different advantages depending on the way they handle the unknown parameters (i.e. deterministic or stochastic), on their computational effort demand (i.e. number of required simulations) and on the way they handle the measurement data (i.e. on-line or off-line[1]). To validate the estimations of the unknown parameters (related either to material properties or geometry), the model parameters for each specimen are independently estimated twice, according to two different sets of measurements, and successfully compared to one another. To the best of author's knowledge, the use of the particle filtering and the TMCMC technique has not been reported when dealing with MEMS applications. These methods, by allowing for measurement errors to affect the parameter estimation process, return parameter distributions rather than parameters value only; therefore, they can be advantageous over the classical algorithms (i.e. least squares minimization) which do not fully accommodate the possibility that a given set of measured data can be subjected to the sources of uncertainties [Green and Worden, 2015].

[1] The on-line parameter estimation algorithms update the estimates of the parameters of a model every time new experimental data (e.g. observation) is available during the parameter estimation operation. On the contrary, in off-line estimation, all the input/output data via experiments are first collected, and the model parameters are then estimated only once.

In the above studies, it is also attempted to assemble a novel framework for Bayesian parameter estimation whose computational effort is kept low by using model order reduction techniques. Since Bayesian approaches require a large set of model response evaluations at varying parameters (uncertainties) [Yuen, 2010], a reduced order modelling of the system is envisaged. An efficient synergy of a proper orthogonal decomposition (POD) method [Sirovich, 1987] and a kriging metamodel [Sacks et al., 1989a] is adopted, to form a non-intrusive technique drastically reducing the computational burden of a high-fidelity model and achieving high speedup. The effectiveness of the POD-kriging approach hinges on the adopted sampling strategy to train the reduced model. To avoid the well-known curse of dimensionality[1], we employ a sequential sampling strategy based on Smolyak sparse grids method [Smolyak, 1963]. Beside the huge speedup of the calculations, POD-kriging can be easily merged into the available computationally expensive models without any substantial modification. The efficiency and effectiveness of the proposed framework (i.e. the POD-kriging TMCMC) is verified via a set of experimental tests. It is shown that the algorithm successfully i) constructs the relevant reduced model and ii) identifies the parameters complex distributions based on the measurement data at a low computational cost.

It is worthwhile mentioning that the kriging metamodelling has been already coupled with the POD for computational reduction in computational fluid dynamics (CFD) [Braconnier et al., 2011, Margheri and Sagaut, 2016]. The POD decreases the cost of constructing kriging metamodel, specially when the high fidelity model generates many outputs. On the other hand, an adoption of the kriging-TMCMC is presented in [Angelikopoulos et al., 2015] and successfully tested in structural dynamics using pseudo-experimental data to obtain parameters of a finite element model. In this thesis, the POD-kriging is instead used along the TMCMC algorithm, and differently from the approach in [Angelikopoulos et al., 2015, Margheri and Sagaut, 2016], a simpler sequential sampling method is adopted to construct the POD-kriging model. The capabilities of the proposed method are demonstrated by parameter identification based on actual experimen-

[1] Curse of dimensionality refers to the exponential increase in volume associated with adding extra dimensions to a mathematical space. In sampling, it implies that the number of required samples often grows exponentially with the number of unknown parameters.

tal measurements.

1.3 Organization of the thesis

The investigations are structured in the following chapters.

- **Chapter 2** presents a concise overview of the MEMS devices, the fabrication process adopted in the current work and the mechanical properties of polysilicon. Accordingly, the existing literature addressing the evidences of uncertainties in the performance of polysilicon MEMS devices is reviewed. The chapter finishes with a list of available experimental tests for MEMS characterization.

- **Chapter 3** describes thoroughly the developed test device characteristics and its operational principles. Two specimen geometries are tested using ten samples for each one, and the measurements are reported accordingly in terms of static capacitance change versus the actuation voltage. A great amount of scattering among the specimens are recorded despite the nominally identical features of the specimens, which demonstrates the presence of the uncertainty sources in the devices.

- **Chapter 4** outlines the details of the analytical and the numerical models developed for the test device. Their outputs are compared, showing that, due to the adopted simplifications, the numerical model yields results in better agreement with the experimental measurements.

- **Chapter 5** presents the overall bounds on the electromechanical response of the devices, based on the maximum variation of polysilicon mechanical properties. Next, two sets of Monte Carlo simulations are adopted, to relate the variations in the polysilicon morphology and grain orientations to the scatterings observed in the electromechanical responses. It is shown that the impact of this source of uncertainty (i.e. variations in the mechanical properties) is intensified for the smaller specimens (which is not often expected in relatively large structural components with respect to the grain

size). It is also concluded that the effects of fabrication inaccuracies must be taken into account to explain the measured data.

- **Chapter 6** proposes a particle filtering approach for stochastic parameter estimation allowing for two prevailing unknown parameters: the Young's modulus and a fabrication inaccuracy related term called over-etch. The sensitivity of the responses to the variation of these two unknown parameters is firstly investigated and then a particle filter is adopted to estimate their values for each single specimen, based on the relevant measurements. The parameter estimation is individually carried out for two measured responses for each specimen, and the estimated parameters are compared as a cross-validation test of the consistency of estimated parameters. It is seen that the particle filter, as an on-line parameter estimation method, is stable in terms of the estimations in the present problem, but the two parameters are not sufficient to accommodate the experimentally observed scatterings.

- **Chapter 7** takes into account another geometric source of uncertainty in addition to the previous two, the rotation offset of the specimen. Among remaining possible uncertainty sources, the rotation offset is more likely to be present in the fabricated devices and its effect in the device response can be important. Unlike the previous chapter, two deterministic and intrinsically off-line parameter estimation methods, namely a genetic algorithm and the Levenberg-Marquardt algorithm, are employed. It is shown that, by adding the third parameter in the formulation, the genetic algorithm can carry out a successful estimation; a remarkable improvement in the consistency of the estimated values is also obtained.

- **Chapter 8** proposes a framework for a model order reduction and probabilistic parameter estimation technique. First, a comprehensive review on the available reduction methods is provided and then the adopted POD and kriging metamodel are explained in detail. Next, a short review of Bayesian inference methods is addressed and the TMCMC is employed in conjunction with the opted model order reduction. The exemplary results of the proposed method for the experimental measurements are reported, exhibiting the capabilities of the POD-kriging TMCMC.

- **Chapter 9** summarizes the achieved results and presents conclusions and prospects for future work.

2

MEMS and uncertainties

2.1 Introduction

Dealing with mechanical systems at the micro scale needs special attention due to the relevant uncertainties. In this regard, we initially provide a brief introduction to microelectromechanical systems (MEMS) and their common fabrication process in Section 2.2. Since polysilicon is by far the most widely used structural material for the deformable components in such systems, the basic mechanical properties of single crystalline silicon and polycrystalline silicon, also known as polysilicon, are reviewed in Section 2.3. Thereafter, Section 2.4 provides a list of possible sources of uncertainties in the MEMS operational performance, and Section 2.5 describes some standard mechanical characterization techniques at the micro scale available in the literature. This chapter finishes with some concluding remarks gathered in Section 2.5.

2.2 MEMS and microfabrication

MEMS technology has been a successful engineering field since late eighties. Nevertheless, the first attempts to develop micro scale systems can be traced back to 1967 when [Nathanson et al., 1967] proposed first silicon based mechanical micro-device that never commercialized. It was late seventies when the first suc-

cessful MEMS were manufactured: gas microchromatographs (1975), inkjet head printers (1977), micromirrors (1980), and read/write hard disk heads (1981) [Petersen, 1982]. The MEMS technology experienced a boost only by the end of nineties when advanced manufacturing methods in microelectronic fabrications were finally augmented with adaptive manufacturing techniques; complex MEMS devices at low price and high quality could be then developed. These devices merge mechanics and electronics either to sense, control, and actuate mechanical processes at the micro scale, or to be integrated into a macro system to perform a second task.

Beside the apparent benefits, such as mass production, low price and ease of integration with other systems due to their small size, MEMS devices offer advantages linked to a range of unconventional physical phenomena at the small scales [Gad-el Hak, 2001, see Chapter 2]. Shrinking the size of the devices to the micro scale, the dominance of physical phenomena alters, as the surface-to-volume ratio for the systems increases. For instance, the Reynolds number, i.e. the ratio of inertial forces to viscous ones, will remain low for micro scale machines. This means that the flow in the microchannels is almost entirely dominated by laminar flow rather than turbulent flows which exist at the macro scale. Another evident example occurs in electrostatic applications, where the attraction forces between opposite charges can be exploited for actuation/sensing purposes in a MEMS device. Similarly, rapid heat removal may be also realized since head conduction accelerates where the surface-to-volume ratio increases. These effects can be advantageous for some applications, while casting limitations for others.

Three major types of micromachining techniques for MEMS fabrication in industrial context are surface micromachining, bulk micromachining and LIGA (German acronym for Lithographie, Galvanoformung, Abformung). The first process is based on consecutive deposition of layers of different materials (e.g. silicon, aluminum, nickel or tungsten) on a silicon wafer [Bustillo et al., 1998]. These layers will be removed or kept selectively through successive stages of microlithography or etching (either dry or wet). This method does not face a limitation on the number of material layers; therefore, a complex structure can be realized. It is a well-established method and can be used repetitively for MEMS production in large numbers. In contrast to surface machining, in which the structure is made

from the deposited layer on the substrate, the bulk machining method aims to realize the structure from the substrate by similar removing techniques used in surface machining. This method is simpler and less expensive than surface machining, and is more suitable for applications which do not require much complexity and are price sensitive. In LIGA process, the microlithography, electroplating and molding processes are combined. First, a X-ray radiation sensitive polymethyl methacrylate (PMMA) is cast on a substrate, then this layer is selectively exposed to a X-ray radiation through a mask. After the PMMA development, this patterned layer can be used as polymer mold for electroplating the device on the substrate. In the final stage, the PMMA layer is removed and the metallic microstructure will remain. This method allows using materials other than silicon and is more suitable for applications requiring higher aspect ratio devices than what is achievable in surface micromachining. However, its use is limited due to its high cost and the health hazards of X-ray exposure.

In the following, detailed information is provided on the available technique used in this work to realize the MEMS devices.

2.2.1 ThELMA process

The specific fabrication technique used in this work is slightly different from the conventional methods explained above. The ThELMA (Thick Epipoly Layer for Micro Actuators and Accelerometers) developed by STMicroelectronics to realize silicon based inertial sensors and actuators and allows for structures with large thicknesses and complex layers [Corigliano et al., 2004]. This process can realize suspended structures of polycrystalline silicon anchored to the substrate through very compliant components (springs) and thus capable of moving on a plane parallel to the underlying silicon substrate (such as the structure defined in Chapter 3). This process is based on several conventional integrated circuit technology steps, together with dedicated MEMS operations, like dry etch and sacrificial layer removal for structure release. Figure 2.1 summarizes the steps involved in this process. These steps include:

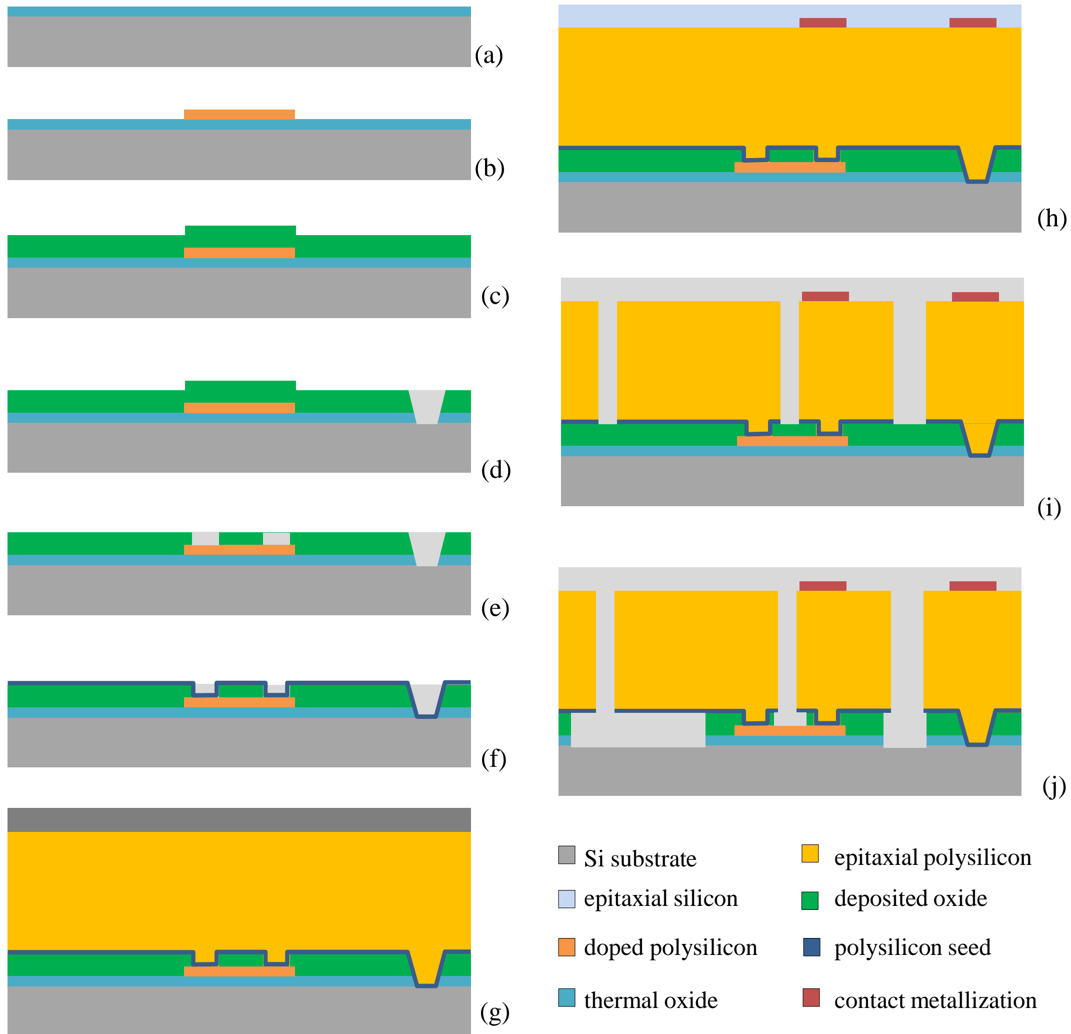

Figure 2.1: Fabrication steps in the ThELMA process. From [Fachin, 2007].

(a) *thermal oxidation of substrate:* the silicon substrate is covered by a 2.5 μm thick oxide layer through a thermal process at 1100 °C;

(b) *deposition and masking of polysilicon:* the first polysilicon layer is masked and doped with phosphorus and attached to the oxide layer by using plasma in order to act as buried runners. The task of these interconnections is to deliver the electrical signals from/to the pads located at the exterior part of device;

(c) *deposition of sacrificial oxide layer:* an oxide layer is deposited and condensed using a Plasma Enhanced Chemical Vapor Deposition (PECVD) process. The set of this layer and the thermal oxide will be subsequently removed to accommodate a gap spacing between the moving components of the structure and the substrate;

(d) *anchoring to the substrate:* a wet etching process with hydrofluoric acid and controlled by an appropriate mask permits the selective excavation of oxide layers for necessary contacts with the substrate;

(e) *anchoring to the polysilicon runners:* the oxide is once again removed to facilitate the contact with the polysilicon buried runners. In contrast to the previous step, the dry removal process is carried out using plasma in order to define vertical profiles with high precision;

(f) *deposition of silicon seed crystals:* in this step, the silicon seed crystals (also known as reactors) are deposited to facilitate the growth of polysilicon in the next step;

(g) *growth and doping of the epitaxial polysilicon:* the main body of the structure is formed in this step by growing epitaxial polysilicon. In this step, all the lower layers are covered and a single crystalline epitaxial silicon is also grown corresponding to the alignment marks;

(h) *masking and deposition of the contact metalization:* the contact metalization is deposited through appropriate masks on the surface which experiences a second wet etching;

(i) *trench etching:* this step consists of masking the epitaxial layer and etching it by a deep dry etch technique with sulfur hexafluoride acid. The etch depth reaches to the oxide layer; therefore, the moving components of the structure are realized.

(j) *sacrificial oxide layer removal:* finally, the process is concluded by removing the sacrificial oxide layer by means of a dry etch in vapor phase acid, to avoid the adhesion phenomenon. Such phenomenon can occur if a liquid acid is used, creating strong capillary attractive forces which can damage the structure.

Nevertheless, the ThELMA process inherits some technological limitations. The most evident defect is rooted in the chemical etching process for creating the trenches. Since a perfect control of etchant is not possible, the epitaxial removal

is not performed exactly as it is designed. This effect is explained more in details in the following of this chapter. Another problem which can arise for devices fabricated by ThELMA process is the developed residual stresses due to the thermal treatments. They are usually of a compressive nature in the polysilicon layer parallel to the substrate. This issue may result in a lack of planarity of the whole device, or partial buckling of springs depending on the structure design, anchoring type and its size [Corigliano et al., 2004].

Since the structural components in ThELMA process are formed from polysilicon, it is necessary to review this material in the following of this chapter from a mechanical point of view.

2.3 Polysilicon elastic properties

Polysilicon has been the material of choice for the MEMS fabrication to date because of its advantageous electrical/mechanical properties as well as the well-established fabrication processes for intricately shaped devices [Yagnamurthy et al., 2015]. Polysilicon is an aggregate of single crystalline silicon grains. Its elastic properties clearly depend on its constituents behaviour: mechanical properties of the single grains, their shape and their orientation (i.e. polysilicon morphology). Though polysilicon is a heterogeneous material, it can be modelled appropriately as a homogeneous one in the macro or meso scale applications where the structural details are large compared to the polysilicon grain size [Cho et al., 2005]. These properties are well characterized either experimentally or numerically by standard homogenization methods on random samples of polysilicon [Mariani et al., 2011]. At the micro scale, the local behaviour is of interest; therefore, a heterogeneous model is needed to take into account the behaviour of each silicon crystal and their granular organization. Therefore, reviewing the elastic properties of single crystalline is necessary.

2.3.1 Single crystalline silicon properties

The silicon lattice, i.e. the periodic arrangement of the atoms in the crystal, is formed by diamond-like unit cells, that displays the face-centered cubic structure. To describe crystal orientation dependent material properties, we need to first

describe crystal orientations which are described by Miller indices in a format of three integer triples "*hkl*", corresponding to an xyz coordinate system. In particular, (hkl) and $[hkl]$ refer to a plane and a direction in the crystal, respectively. The triple *hkl* values are the reciprocals of the coordinates of the intercepts on the xyz axes, multiplied by the lowest common denominator. An upper bar on the index denotes a negative direction. When referring to directions and angles within a cubic crystal, the xyz axes are aligned with the $\langle 100 \rangle$ family of directions unless otherwise specified. The important directions for silicon are shown in Figure 2.2.

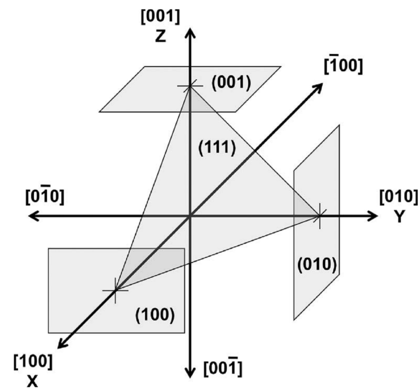

Figure 2.2: Miller Indices in a cubic crystal. By convention, the directions [100], [010] and [001] are the xyz Cartesian axes. From [Hopcroft et al., 2010].

As usual for crystalline materials, silicon displays an anisotropic behaviour, that can be defined as a function of the crystallographic orientation. Figure 2.3 reports the values for Young's modulus and Poisson's ratio as a function of the orientation in the (100) plane. Due to the present cubic symmetry of the structure, it is possible to describe the general anisotropic elasticity tensor in the form of the strain-stress relation Eq. (2.1), fully determined by only three independent

constants.

$$\begin{bmatrix} \sigma_1 \\ \sigma_2 \\ \sigma_3 \\ \sigma_4 \\ \sigma_5 \\ \sigma_6 \end{bmatrix} = \begin{bmatrix} c_{11} & c_{12} & c_{12} & 0 & 0 & 0 \\ c_{12} & c_{11} & c_{12} & 0 & 0 & 0 \\ c_{12} & c_{12} & c_{11} & 0 & 0 & 0 \\ 0 & 0 & 0 & c_{44} & 0 & 0 \\ 0 & 0 & 0 & 0 & c_{44} & 0 \\ 0 & 0 & 0 & 0 & 0 & c_{44} \end{bmatrix} \begin{bmatrix} \epsilon_1 \\ \epsilon_2 \\ \epsilon_3 \\ \epsilon_4 \\ \epsilon_5 \\ \epsilon_6 \end{bmatrix} \tag{2.1}$$

This formulation holds for a specific Cartesian reference aligned to the silicon cubic crystal, i.e. when the $\langle 100 \rangle$ directions are the default xyz axes. The three independent coefficients in the stiffness tensor are reported accordingly in Table 2.1. Having these stiffness coefficients, stress or strain can be obtained by solving Eq. (2.1).

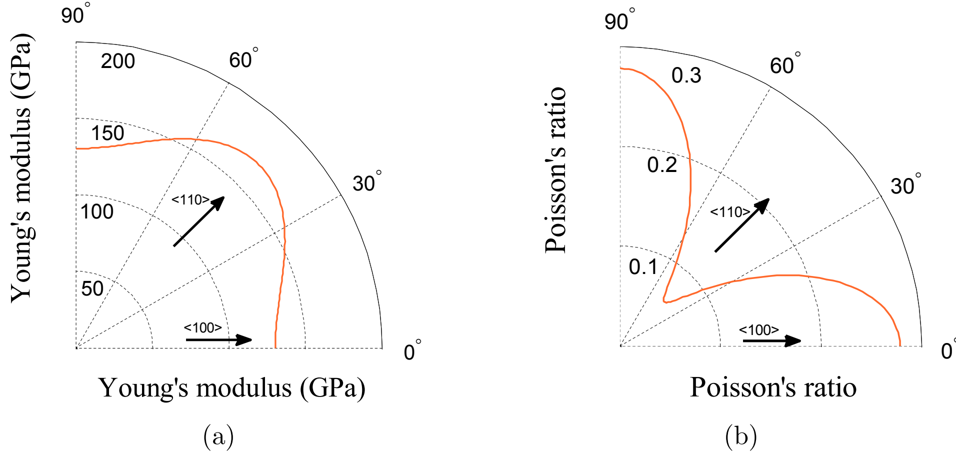

Figure 2.3: Variation of linear elastic parameters versus orientation in the silicon crystal for (100) plane using the coefficients reported in Table 2.1. (**a**) Young's modulus, and (**b**) Poisson's ratio.

Table 2.1: Elastic constants of silicon at room temperature [Brantley, 1973].

Parameter	Value
c_{11}	165.7 GPa
c_{12}	63.9 GPa
c_{44}	79.6 GPa

2.3.2 Polycrystalline silicon properties

The main body of the MEMS devices under study are formed through the epitaxial growth of silicon grains on a substrate, to ultimately achieve a polysilicon structure. Though a constitutive model for single crystalline silicon can be obtained as it has been shown in Section 2.3.1, such expression can not be furnished for polysilicon. Since the grains are sharing (almost) the same growth orientation, a preferential direction for the reference frame of each grain is therefore achieved, i.e. direction of the growth which is perpendicular to the substrate. However, in-plane (perpendicular to the growth direction) orientation of each silicon lattice is arbitrary. In conclusion, we will suppose that the in-plane x'- and y'-axes of the local reference for each grain are unique to that grain but the out of plane z'-axis is shared by all grains (see Figure 2.4).

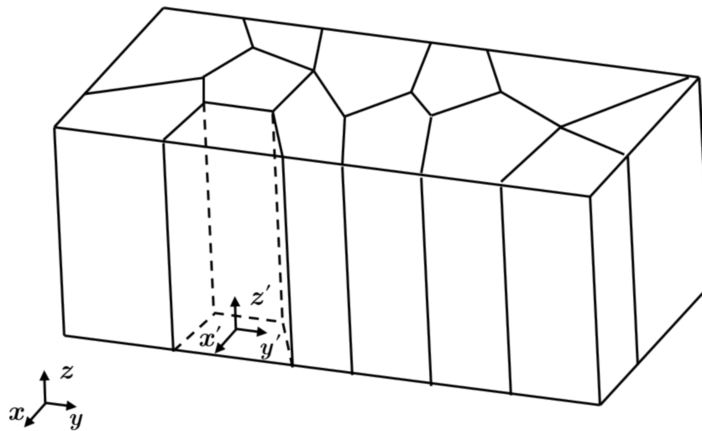

Figure 2.4: Global and local reference frame.

To model the polysilicon random morphology, a centroidal Voronoi tessellation (CVT) can be used. The advantage of CVT is that it employs a strategy similar to the actual silicon seed crystals deposition on the substrate and growth stage as in the ThELMA process [Martini, 2008]. At the growth stage of silicon grains, each seed starts to occupy the neighboring space with the same rate till two neighboring grains reach each other, forming the grain boundaries. Similarly, the CVT algorithm uses a uniform distribution function to generate random

Figure 2.5: Digital realization of epitaxial polysilicon with identical out-of-plane axis and random in-plane orientation.

seeds on the surface. Then, the domain is divided in polygonal sets, in which the boundaries are the perpendicular bisectors of the lines joining each two neighboring seeds. Each formed polygon can be then extruded to finalize the three dimensional columnar grain crystals (see Figure 2.5). A comprehensive review on properties and implementation of CVT can be found in [Du et al., 1999].

CVT provides the polysilicon grain morphology and then random grain boundaries and a random in-plane orientation for each grain can be attributed. The constitutive law within each grain is described by Eq. (2.1) in the local reference system (x',y',z'). This relation can be stated in the global reference frame (x,y,z) using the direction cosine matrix, i.e.

$$\mathbf{N} = \begin{bmatrix} \cos_{x'x} & \cos_{x'y} & \cos_{x'z} \\ \cos_{y'x} & \cos_{y'y} & \cos_{y'z} \\ \cos_{z'x} & \cos_{z'y} & \cos_{z'z} \end{bmatrix} \tag{2.2}$$

The elements of this matrix are the cosine of the angle between the two corresponding axes stated in the subscript.

Let σ' be the stress tensor in the local reference frame aligned with the grain crystallographic orientation, and σ its counterpart in the global reference frame. Theses two are related through

$$\sigma' = \mathbf{N}\sigma \tag{2.3}$$

This equation can be reorganized in the Voigt's notation as

$$\sigma' = \mathbf{T}\sigma \tag{2.4}$$

Similarly, it is

$$\epsilon' = \mathbf{T}\epsilon \tag{2.5}$$

and $\mathbf{T}$ is [Martini, 2008]

$$\mathbf{T} = \begin{bmatrix} c_{x'x}^2 & c_{x'y}^2 & c_{x'z}^2 & 2c_{x'y}c_{x'z} & 2c_{x'x}c_{x'z} & 2c_{x'x}c_{x'y} \\ c_{y'x}^2 & c_{y'y}^2 & c_{y'z}^2 & 2c_{y'y}c_{y'z} & 2c_{y'x}c_{y'z} & 2c_{y'x}c_{y'y} \\ c_{z'x}^2 & c_{z'y}^2 & c_{z'z}^2 & 2c_{z'y}c_{z'z} & 2c_{z'x}c_{z'z} & 2c_{z'x}c_{z'y} \\ c_{z'x}c_{y'x} & c_{z'y}c_{y'y} & c_{z'z}c_{y'z} & c_{z'y}c_{y'z}+c_{z'z}c_{y'y} & c_{z'z}c_{y'x}+c_{z'x}c_{y'z} & c_{z'x}c_{y'y}+c_{z'y}c_{y'x} \\ c_{z'x}c_{x'x} & c_{z'y}c_{x'y} & c_{z'z}c_{x'z} & c_{z'y}c_{x'z}+c_{z'z}c_{x'y} & c_{z'z}c_{x'x}+c_{z'x}c_{x'z} & c_{z'x}c_{x'y}+c_{z'y}c_{x'x} \\ c_{y'x}c_{x'x} & c_{y'y}c_{x'y} & c_{y'z}c_{x'z} & c_{x'y}c_{y'z}+c_{x'z}c_{y'y} & c_{x'y}c_{y'z}+c_{x'x}c_{y'z} & c_{x'x}c_{y'y}+c_{x'y}c_{y'x} \end{bmatrix} \tag{2.6}$$

where the cosines elements are indicated by 'c'. The relation between stress and strain in the local reference frame is

$$\sigma' = \mathbf{C}_{local}\epsilon' \tag{2.7}$$

which can be rewritten using Eq. (2.4) and Eq. (2.5) and the orthonormality of transformation matrix

$$\sigma = \mathbf{T}^{-1}\mathbf{C}_{local}\mathbf{T}\epsilon = \mathbf{C}_{global}\epsilon \tag{2.8}$$

This relation will be used in the numerical model developed in Chapter 4 to transform the stiffness matrix in the local reference frame into the global one and to assemble a global stiffness matrix.

2.4 Sources of uncertainties

The constant need for smaller MEMS devices requires miniaturization of the constituent structural components. At the same time, reliability issues related to the devices' operation should be addressed for new designs. The challenging issue in designing such new devices is that the miniaturization appears to aggravate the performance of the device operation [Brand et al., 2013]. These devices have typically structural components that deform either for actuation or sensing purposes; stiffness, thus, represents a key factor to characterize their behaviour. Whether the operational principle is statical or dynamical, the final performance depends strongly on how close the actual stiffness of the deformable components is to the designed one, and this issue turns more critical as the characteristic size of the components shrinks. The stiffness variation is originated from uncertainties in the fabricated geometry or in the mechanical properties of the material. The geometry uncertainties depend strongly on the fabrication process [Hong et al., 2000, Alper et al., 2008], while uncertainties in mechanical properties can have intrinsic origins. This is especially the case for the micro-size components made of polycrystalline materials like polysilicon. This issue is illustrated in Figure 2.6; the two samples of polysilicon are essentially different in terms of the ratio between the specimen size and the average grain size. As it has been shown in [Ballarini et al., 1999], the macroscopically isotropic behavior of polysilicon can be obtained only by domains that include at least a few tens of grains, see Figure 2.6(a). The elastic properties for such samples can be computed from homogenization procedures with a high degree of confidence. In contrast, for smaller domains with few grains (see Figure 2.6(b)), the assumption of in-plane isotropy will not hold any more and the material must be treated as locally anisotropic. Consequently, the closed form solutions such as Eq. (2.1) must be replaced deterministically by a finite element analysis, or statistically by considering probability distributions of the mechanical properties [Cho and Chasiotis, 2007].

Many of MEMS devices have deformable structures. To ensure the working efficiency of these devices, a large class of methods have been developed to adjust the stiffness after fabrication. These methods employ a wide range of physical phenomena to cope with stiffness variation; some use electrostatic effects to ma-

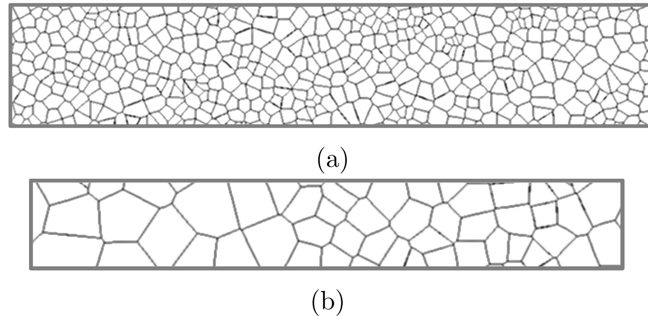

(a)

(b)

Figure 2.6: Morphology samples of polysilicon inside specimens. (**a**) Specimen with relatively high number of grains, and (**b**) specimen with relatively low number of grains.

nipulate the overall system stiffness [Torun et al., 2007]; or, some use mechanical tuning like changing the effective beam length [Zine-El-Abidine and Yang, 2009]; or, another method is changing the cross section shape and consequently the second moment of area by activating/deactivating employed piezoelectric layers [Kawai et al., 2006] and some others take advantage of the axial stressing effect [Syms, 1998]. A recent review on these methods can be found in [de Laat et al., 2016]. Nevertheless, these workarounds can influence the electrical and mechanical performance of the designed device. In addition, they require specific tunning for each application. These techniques may provide solutions to cope with the existing uncertainties, but there is still a need for an improved understanding of the origins and the extent of stiffness deviation from the desired value, as the required degree of miniaturization grows for novel applications. To this goal, reliable micromechanical characterization methods are necessary.

A wide range of micromechanical tests have been developed in literature using MEMS technology [Pantano et al., 2012, Zhu and Chang, 2015]. The published results outline an effective, isotropic polysilicon Young's modulus on the range of 100-173 GPa, with reported scatterings up to 15% [Corigliano et al., 2010, Gravier et al., 2009, Kamiya et al., 2007, Sharpe Jr. et al., 2001, Tsuchiya et al., 2005, Oh et al., 2005, Espinosa et al., 2007]. The difference between the estimated average values can be explained by the dependence of Young's modulus on the fabrication facilities and the deposition techniques that varies from one study to another [Hopcroft et al., 2010]. On the other hand, some of these studies have reported

a greater scattering when specimen features a smaller characteristic size [Gravier et al., 2009, Sharpe Jr. et al., 2001]. This deviation can be due either to measurement errors or to the fact that the number of grains in the specimen is not large enough to consider the polysilicon film statistically representative [Cho and Chasiotis, 2007, Mariani et al., 2011]. As a consequence, the measured Young's modulus of polysilicon can feature a large standard deviation [Kanit et al., 2003, Mullen et al., 1997, Bromley et al., 1999]. It has been shown experimentally in [Cho and Chasiotis, 2007] that, when the size of components decreases, the effective behaviour of the specimen can deviate from that described by the isotropy hypothesis. It has been observed that at least a material domain including $15 \times 15 = 225$ columnar grains is necessary to ensure a scattering of effective Young's modulus lower than 5% [Cho and Chasiotis, 2007]. The same research group in a recent work [Yagnamurthy et al., 2015] studied polysilicon film tensile test specimens with varying microstructure and grain size, while keeping the number of grains at gauge section large enough (gauge length 150 μm, average grain size 285 nm). It has been reported that the effective Young's modulus was independent of the film microstructure and the grain size: this conclusion confirms that the key criterion to obtain the effective elastic properties is the number of grains in the material domain rather than the absolute size of grains. A similar numerical study [Reedy et al., 2011] on tensile test specimens comprising about 50 grains along the gauge length showed a small ratio of the standard deviation in Young's modulus to its average equal to 0.025. Variations in effective material properties can be particularly more pronounced for bending specimens, where a non uniform stress/strain profile and more sensitivity to the surface effects is expected [Sadeghian et al., 2009].

An additional source of uncertainties in evaluating the mechanical properties at the micro scale is the deviations of the specimen dimensions. In bulk mechanical structures, the dimensions of structures are made highly accurate by means of machining tools with a precision of more than one thousandth of its dimensions. However, in MEMS structures, although the absolute error in fabrication is smaller than at the macro scale, the relative accuracies are not good [Brand et al., 2013]. These errors can be manifested in the over-etch [Jang et al., 2012], i.e. the surplus/dearth of etch with respect to the expected one. According to

[Xiong et al., 2005], *"an etch variation defect is one that the thickness of the device structure does not meet the design expectation due to the etch variations caused by fluctuation of temperature, etchant concentration, and other reasons"*. Though the order of such variation is less than 1 μm (depending on the production process and on the geometry), its relative importance can increase when the components shrink down to a comparable size. Overall, a variation of 10 % in the geometry can be expected [Hong et al., 2000] in the conventional MEMS devices. In [Alper et al., 2008], capacitive gaps (in electrostatic actuation/sensing) of 5.3 and 5.6 μm were reported for a layout value of 5 μm; in [Gad-el Hak, 2001], it was stated that for a 2 μm thick structural polysilicon, patterned by a wafer stepper and etched with a reactive-ion etcher, a reasonable estimate for the variation in the linear dimension of etched features was about 0.2 μm (with 10 % relative tolerance). These variations have dominant effects on the bending rigidity of beams, due to variations of the in-plane thickness, or on the actuation and sensing at electrostatic mechanisms, due to variations of the gap at capacitors.

In addition to these two primary sources of uncertainty, other uncertainties may arise due to specific design or fabrication process. These additional uncertainties will be described later in Section 3.5 for the particular device developed in this work.

2.5 Micromechanical characterization methods

A reliable knowledge of mechanical properties of the MEMS materials is essential not only for design and fabrication purposes but also to feed the predictive models. Though standard well-assessed mechanical characterization methods at the macro scale have been present for a long time, these methods are not transferable to the MEMS dimension. Therefore, in the last two decades, many techniques have been developed to investigate the mechanical properties at smaller length scales. This investigation at these small dimensions is important as to explore the effects of small length scales and the fabrication process on the mechanical properties of the materials. The number of these researches is grown exponentially, but still micro scale material characterization is a challenging issue.

It is worth defining two terms that will be used in this work. Limiting the

attention to silicon based MEMS, a general classification of test procedures can be made between *off-chip* and *on-chip* devices [Corigliano et al., 2005]. In both cases, the specimen is generally produced by deposition and etching procedures (e.g. in ThELMA process). An off-chip testing approach generally resorts to some sort of external gripping mechanism, load application (actuation) or measurement sensors. Consequently, the correct alignment of the specimen in the external mechanism or the gripping mechanism are crucial and must be dealt with extra attention. On the contrary, on-chip test devices are real MEMS in which actuation and sensing is performed with the same working principles of MEMS. Therefore, the experimental conditions are similar to those occurring in conventional MEMS devices. In the following a list of common tests for MEMS characterization (mostly for the material properties or fabrication inaccuracies) is discussed in brief as adopted from [Sharpe, 2008, Pantano et al., 2012, Lucon, 2014].

2.5.1 Tension tests

This is a conventional category of tests which uses the same idea of the macro scale counterpart. The elastic properties are obtained by fixing (gripping) one end and applying an increasing tensile load at the other end. This type of tests is popular at microcharacterization; nevertheless, their realization at the micro scale (and the nano scale) faces difficulties. For instance, the specimen alignment at the testing structure is vital to obtain accurate results. Additional issues requiring high levels of microfabrication techniques include preparation of free standing, stress free samples and appropriate gripping. Regarding the displacement and force measurements a wide range of methods has been developed since the conventional solutions are usually not suitable at the micro scale. An example of this testing method is illustrated in Figure 2.7 where an electro-thermo mechanical actuator and a set of parallel plate capacitors are adopted for loading and elongation measurement at the specimen, respectively. Despite these difficulties, it is an effective method when the obtained properties are supposed to be used for MEMS with component size much larger than the grain size [Yagnamurthy et al., 2015]. As the length of the specimen decreases, the effects of uncertainties are intensified and the measured elastic properties can feature large value of standard

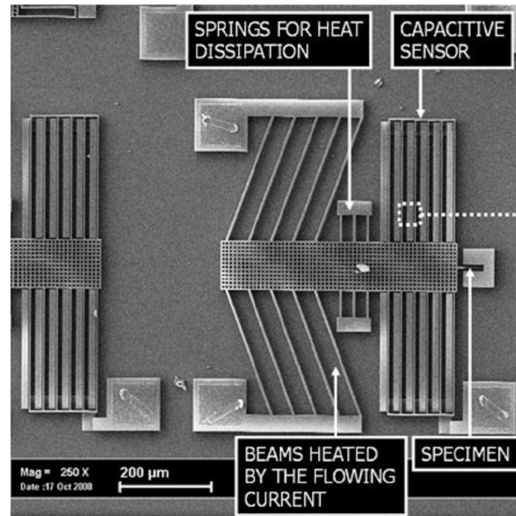

Figure 2.7: A tension test configuration taken from [Corigliano et al., 2010]. The actuator beams expand in their length as they are heated by the electric current, to pull the specimen, and the induced elongation in the specimen is detected at the capacitive sensors.

deviations. An extensive list of methods and examples of tension tests can be found in [Espinosa et al., 2012].

2.5.2 Bending tests

This class is an alternative for tension tests. This test sometimes is preferred over the tension tests since it can produce larger displacements with smaller forces. However, the deduction of elastic properties is more complicated; it usually involves solving inverse problems exploiting analytical models. Furthermore, the specimens are sensitive to the fixing technique which can induce errors in the measurements; the realization of ideal rigid constraints in a micro scale testing configuration is a challenging issue. Several configurations have been developed for bending tests, such as micro beam tests, bulge tests and M-test.

In the micro beam tests, the specimen is a rectangular beam loaded with a concentrated bending force; the beam can be either a cantilever loaded at the free end (see Figure 2.8(a)) or clamped-clamped beam loaded at the midspan

(see Figure 2.8(b)). The elastic properties can be obtained from the analysis of the collected load-deflection data. The specimen in the bulge test is instead a membrane which is clamped around its periphery on a supporting frame. The membrane is deflected by applying a pressure difference on its two surfaces (for instance by compressed air) and the resulting deflection in the center of the membrane is recorded as a function of the pressure via a laser interferometer. The elastic properties can be then obtained from the developed biaxial stress/strain exploiting continuum mechanics models. A layout of this test is demonstrated in Figure 2.8(c). In the M-test, the specimen can be either a beam or a membrane which is loaded by an electrostatic force until the onset of instability phenomenon (i.e. pull-in), see Figure 2.8(d). The mechanical properties could be then linked to the corresponding voltage (pull-in voltage) using analytical formulae or numerical simulations of the coupled electromechanical problem.

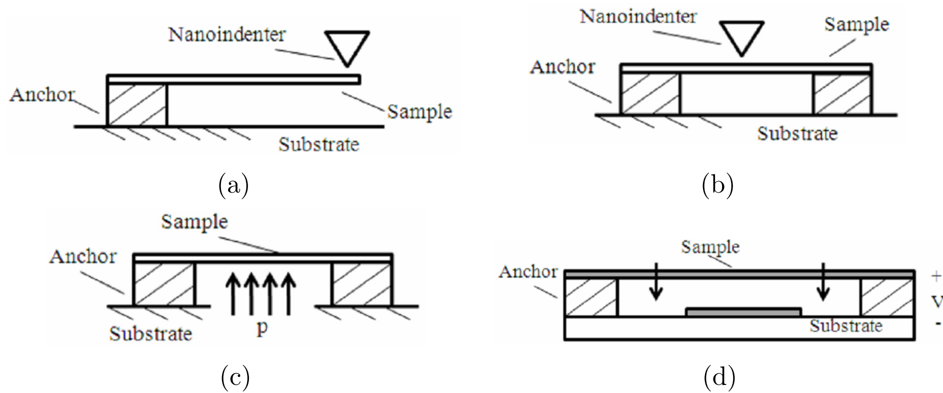

Figure 2.8: Examples of bending test layouts: micro beam test using either (**a**) cantilever or (**b**) clamped-clamped beam, (**c**) bulge test, and (**d**) M-test. From [Pantano et al., 2012].

Another variety of bending based test devices has been realized using on-chip (see Section 2.5) test devices with integrated specimen. The basics of on-chip devices are not different from the ones mentioned above, but they benefit from the fact that they permit the mechanical characterization of the specimen in conditions almost identical to those found in the commercial applications, thus avoiding external disturbances coming form off-chip laboratory tests [Corigliano

et al., 2010]. An example of on-chip test devices is illustrated in Figure 2.9. It features a central ring connected to the substrate by means of two specimens and a set rotational electrostatic capacitor arrays for actuation and sensing. By imposing potential difference at two electrodes of capacitors, a torque will be applied to the central ring, and therefore, the specimens will be loaded in bending in the plane parallel to the substrate. A more detailed review of bending tests can be found in [Pantano et al., 2012].

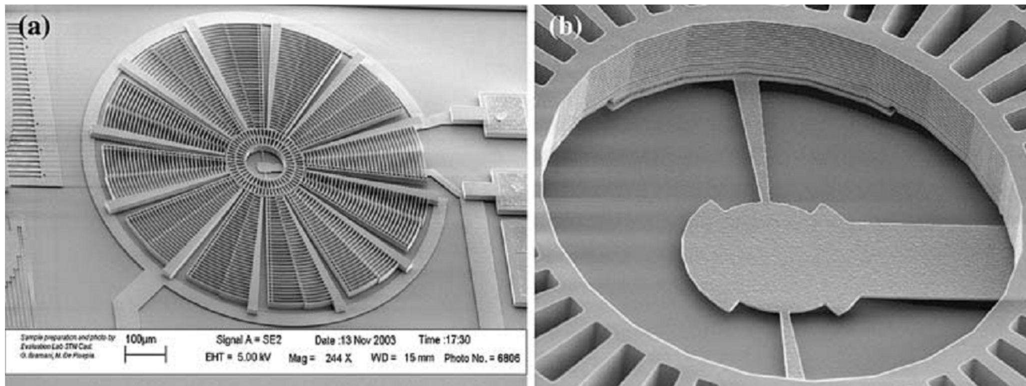

Figure 2.9: On-chip testing device for in-plane bending configuration using rotational actuators. (**a**) General view, and (**b**) details of the bending specimen. From [Corigliano et al., 2005].

2.5.3 Torsional tests

These tests are mostly employed for measuring the shear modulus and the maximum shear stress. Another common use of torsional tests is for the study of the size effects, since they produce strong stress and strain gradients. On-chip device for this testing configuration is also reported in [Saif and MacDonald, 1998]. Torsional tests have not been extensively used due to several limitations related to their implementation, e.g. calibration of torquemeter, the detection of torsion angle, and the alignment between the specimen and the torquemeter [Liu et al., 2012]. An example of this testing configuration is reported in Figure 2.10. Some other examples of such tests can be found in [Fleck et al., 1994, Walter and

Kraft, 2011, Chen, 2013]. Although these methods can be effective on measuring the shear modulus, but deriving the Young's modulus from their output is not possible.

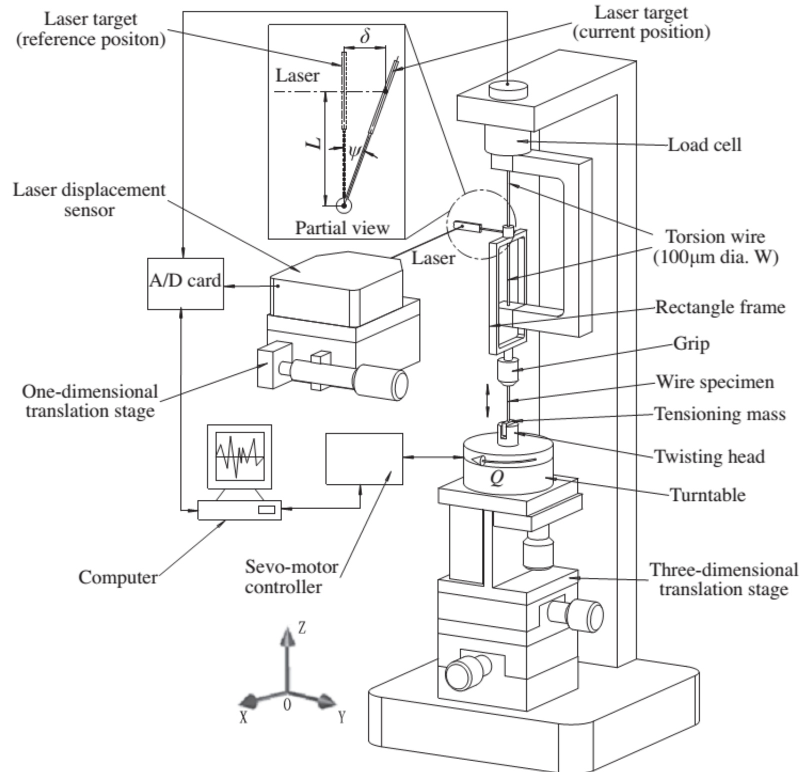

Figure 2.10: Schematic diagram of a torsion test apparatus. From [Liu et al., 2012].

2.5.4 Nanoindentation tests

Nanoindentation is a popular method for microcharacterization of materials due to the simplicity of sample preparation. However, it requires complex data reduction and inverse analysis procedures. In this method, an indenter is pressed on the surface of the specimen causing a local yielding of the material; when the indenter is removed, a permanent imprint is produced. The elastic properties of the material can be evaluated using the load-penetration depth curve. Numerous

research papers on nanoindentation can be found; several articles have reviewed the advances of this technique, see e.g. [Cohen and Kalfon-Cohen, 2013, Gibson, 2014]. However, this method is heavily effected by the presence of substrate supporting the specimen (i.e. substrate effect) and usually is less accurate than the tension tests. It must be noted that the substrate effect is different from the uncertainties stemmed from specimen or real working conditions of the MEMS devices (for instance, anchoring condition in micro beam bending test) which are often present in the commercial MEMS.

2.5.5 Sensitivity Built-In Self-Tests

This kind of test devices is not aimed to characterize a material property but instead their goal is MEMS performance and reliability testing. Combining new types of functioning components, exploiting new material layers, and the interaction with the environment can lead to coexistence of deferent unwanted mechanism which can degrade the performance and reliability of newly designed devices. Different on-chip built-in self-test (BIST) techniques are proposed by researchers to address this issue. These types of test devices have been recently attracting considerable industrial interest since they help to reduce the cost of reliability tests. One of simple applications of BIST techniques is to ensure the functionality of sensors. For example, the mechanism in Figure 2.11(a) includes an electrostatic actuation/sensing to verify that the suspended mass is moving in response to the external actuation, or similarly the mechanism in Figure 2.11(b) exhibits a secondary set of electrodes for ensuring the accelerometer functionality. Another practice of BIST mechanisms is for characterization of the fabrication process; e.g. the device in [Xiong et al., 2005] suggests a method to detect three different defects (stiction, finger height mismatch and over-etch variation) simultaneously, or the device in [Rocha et al., 2008] allows for identifying the value of the Young's modulus in addition to the nonideal fabrication effects. Other examples of BIST devices and techniques can be found in [Mir et al., 2006, Deb and Blanton, 2002, Ramadoss et al., 2008, Matabosch et al., 2014, Legendre et al., 2013, Balachandran et al., 2016].

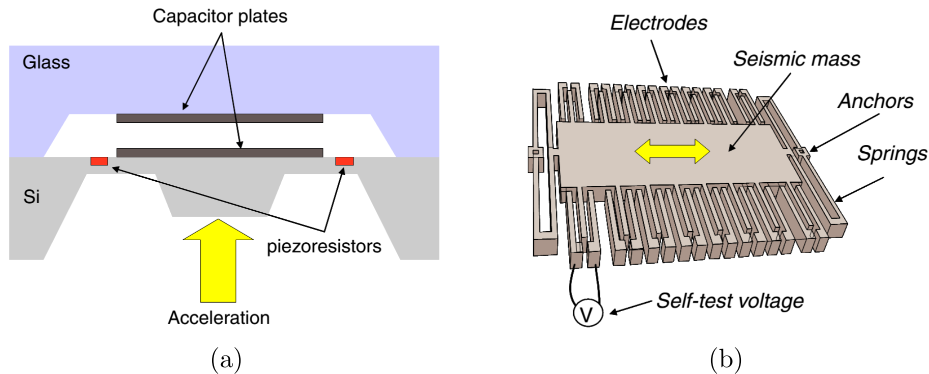

(a) (b)

Figure 2.11: Examples of basic BIST mechanisms used for testing the functionality of accelorometers. (**a**) Piezoresistive accelerometer, and (**b**) capacitive accelerometer. From [Mir et al., 2006].

2.6 Remarks

As mentioned in Section 2.4, the operational performance of the MEMS devices can be influenced by the uncertainties related to the mechanical properties and fabrication process. To address these issues, one might use methods based on surface inspection of the devices through scanning electron microscopy (SEM) or laser interferometry [Hanhijrvi et al., 2012, Hart et al., 2000]; these methods are not only slow to perform but also limited to the devices on open wafers, while commercial ones are usually packed in order to protect the system from the environment.

In the next chapter, we introduce an on-chip testing device which uses a bending mechanism of a cantilever-like beam. Although, the tension tests are the most accurate of the methods above, we are interested to use the bending configuration as it is the prevailing mechanism at the deformable components in the MEMS devices. Moreover, an on-chip testing is preferred over an off-chip methodology, since on-chip test devices exploit the standard microfabricaiton techniques to integrate actuation and sensing principles with the microsystem, so that the experiment resembles the conditions of the commercial MEMS devices [Corigliano et al., 2010]. Adopting on-chip bending configuration, we aim to assess the uncertainties in the elastic properties as well as the ones related to the fabrication inaccuracies that

are present in the real MEMS devices. It is worth noting that we focus on elastic properties rather than the post elastic ones. The motivation for this choice is mainly based on the crucial effect of elastic properties on the operational performance of MEMS devices as they are designed to work within the elastic regime.

page intentionally left blank

3

Experimental campaign using on-chip testing

3.1 Introduction

It was mentioned in Section 2.6 that on-chip testing is preferred over off-chip as it resembles the commercial MEMS devices operational conditions. Therefore, an on-chip test device whose structural components are fabricated using polysilicon is introduced in this chapter. The device features a cantilever-like beam (with different lengths) as specimen and uses a conventional MEMS actuation and sensing technique. The device is capable of performing several testing configurations providing result redundancy that can be used for cross-validation purposes. Two beam lengths are adopted for investigations and for each length ten specimens are tested. Although the specimens for each beam length are nominally identical, large scattering among the measurements are evident which can be caused by the presence of uncertainties mentioned in Chapter 2.

This chapter starts with a detailed description of the test device, its operational principles, and geometric specifications, in Section 3.2. In Section 3.3, the features of the testing set-up are reported and it is explained how four testing configurations are devised in one single device. Section 3.4 reports the measured data for 20 specimens at the four testing configurations. This chapter finishes by some final remarks on the measurements gathered in Section 3.5.

3.2 Test device

The test devices developed for this work are produced through the already mentioned ThELMA process in Chapter 2 by STMicroelectronics which features epitaxial growth of polysilicon with average grain size (in terms of diameter) equal to 0.5 μm. The SEM image of the top view of the whole structure is reported in Figure 3.2. The specimen undergoing deformation is a cantilever like beam (see Figure 3.2 (b)) which is connected to a fixed body of polysilicon called "anchor" in the figure. The anchor itself is mechanically connected to the substrate. The micro beam is connected on the other side to a massive 200 μm $\times$ 200 μm perforated plate denoted as "rotor". The perforations are incorporated in the design to facilitate the etching process of the sacrificial oxide layer (see Figure 2.1 (j)). This step is necessary for complete removal of sacrificial oxide layers to avoid stiction of the suspended components of the device [Comi et al., 2010]. On the other hand, the massive rotor is devised to provide the necessary mass allowing for dynamic tests. The beam's nominal dimensions are: length l=10 μm or 20 μm, out-of-plane thickness w=22 μm, and width h=2 μm (see Figure 3.1). Figures 3.2 and 3.3 report the SEM image of length l=20 μm or 10 μm, respectively. The MEMS devices are placed in a die cavity where a pressure lower than the ambient one, and nominally equal to 0.35 mbar, has been imposed. These MEMS are packaged at low pressure so that the device conditions are close to ones of operational MEMS; for instance at accelerometers where low pressure limits the fluid (i.e. air) damping to ensure low energy consumption [Comi et al., 2010]. The geometric characteristics of the test device are summarized in Table 3.1.

Table 3.1: Geometric dimensions of the device.

Parameter	Value	Parameter	Value
beam length (l)	20,10 μm	initial gap at capacitors (g_0)	2 μm
beam width (h)	2 μm	a	17 μm
out-of-plane film thickness (w)	22 μm	L	200 μm

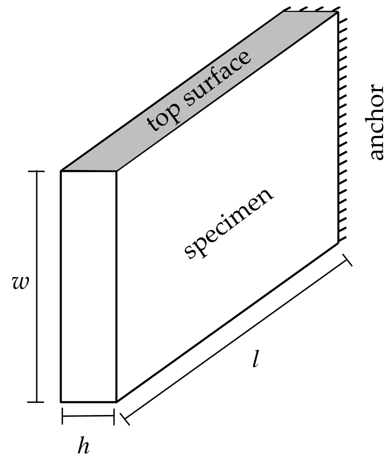

Figure 3.1: Schematic view of the specimen (not to scale).

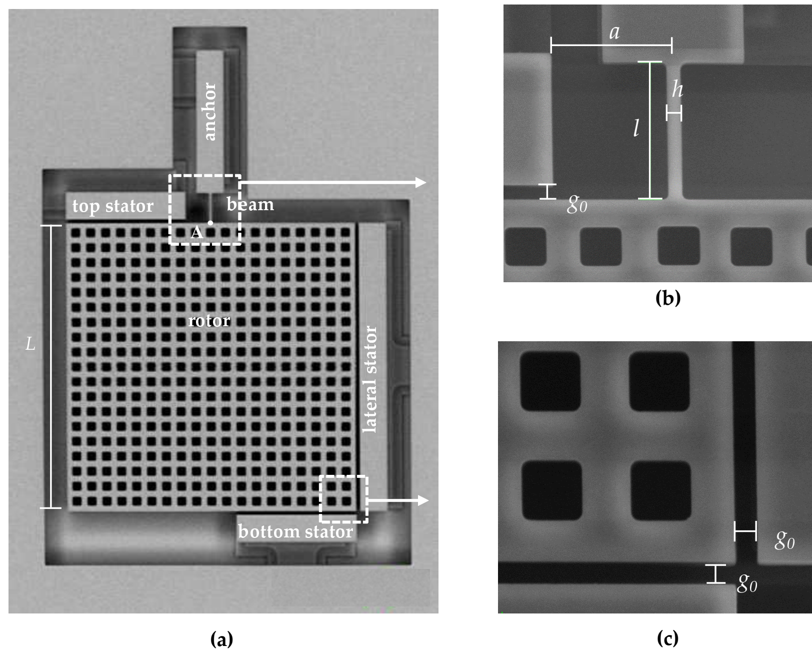

Figure 3.2: (**a**) Device geometry with (**b**) details of the beam region and (**c**) in proximity of the lateral stator for beam length equal to 20 μm.

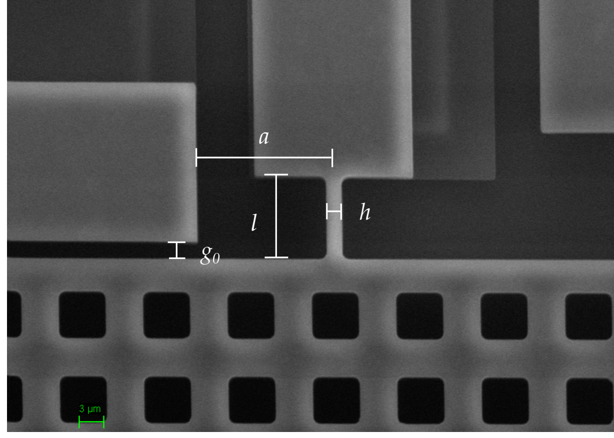

Figure 3.3: Beam region for beam length equal to 10 μm.

The measurement of the system actuation is realized using a standard electrostatic technique by employing the stators around the rotor. By applying an electrical potential difference between the stator and the rotor, an attractive force will be generated to move the rotor toward the stator(s), i.e. the gap between the rotor and the stator(s) is decreased. Since the devices are capped, a visual investigation of the deformations is not possible; therefore, the capacitance between the stators and the rotor can be measured. The resulting input-output relationship is then in the form of capacitance changes versus actuation voltage, or $C-V$ curves. These measurements can be later transformed into the sought beam deformation through appropriate (either analytical or numerical) models.

An Agilent 6614C power supply and an Agilent E4980A digital capacimeter (also known as impedance analyzer) have been used for signal generation and the capacitance measurements. The capacimeter accuracy is on the order of tens of aF while the measured change in capacitance are on the order of a few fF, or hundreds of aF. The capacimeter uses auto-balancing bridge method with an AC current to characterize the device under test (usually referred as DUT), while a bias DC signal is used to provide actuation of the system [Okada and Sekino, 2003]. In the experiments, AC signal of 200 mV-1 GHz is superimposed on an increasing/decreasing DC voltage. The probe station with the micromanipulators (see Figure 3.4) are located in an unclean room, whose registered temperature

is about 25 °C and the relative humidity is between 50–55%; a glassfrit sealing assures the closure of the die.

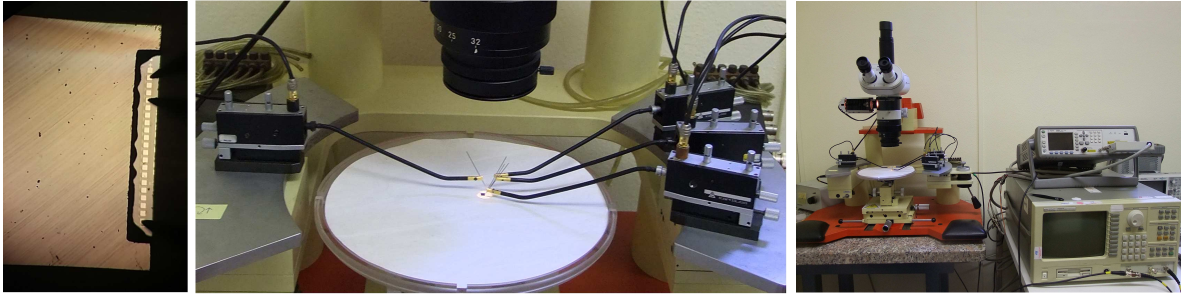

Figure 3.4: Test setup for $C - V$ measurement.

3.3 Testing set-up

Two sets of stators are devised for the testing. One is located on the right side of the rotor (see Figure 3.2) and is called "lateral" capacitor. Other two stators located on the top and the bottom sides of the rotor are electrically connected; they are called "rotational" capacitors as they mainly induce a rotation of the rotor due to their position. Thus, two alternative set-up configurations, depicted in Figure 3.5, are possible for the $C - V$ measurements. In the first (see Figure 3.5 (a)), only the capacimeter is used to a maximum DC of 40 V[1], for both actuation and sensing at the same capacitor. The sensing electrodes and moving mass are connected in the same circuit; consequently the $C - V$ curves increase monotonically. In the second configuration (see Figure 3.5 (b)), a DC power supply provides the DC signal at one of the capacitor systems (actuation). The capacimeter instead measures the change in capacitance at the second capacitance system. In the latter case, actuation and sensing are realized at two different capacitances. In this case, an Agilent 6614C power supply allows to reach up to 100 V, and the $C - V$ curves decrease monotonically because the rotor is moving far from the sensing capacitor. Generally, each point in the curves (either first or

[1] Maximum available DC voltage by Agilent E4980A digital capacimeter is 40 V [Okada and Sekino, 2003].

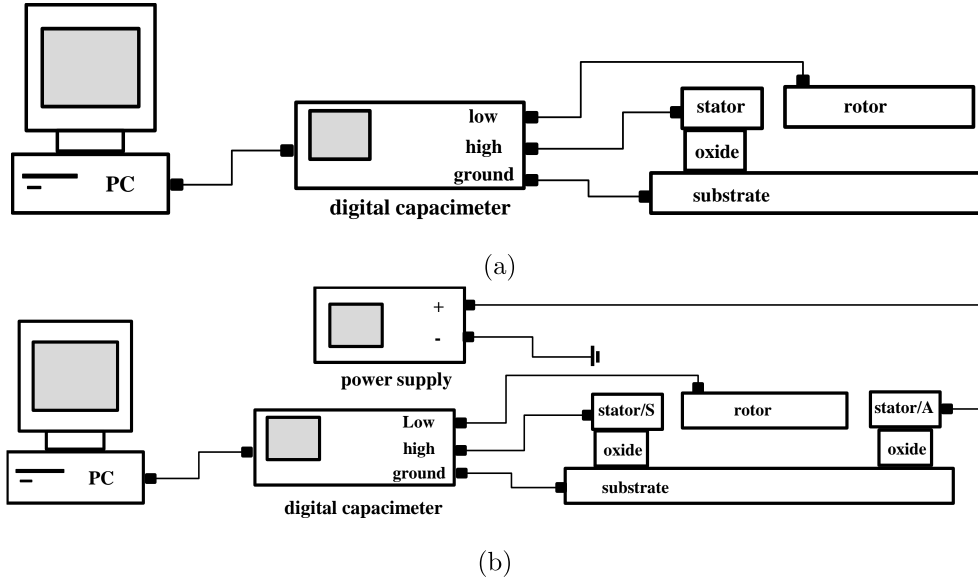

Figure 3.5: Details of the experimental setup for using (**a**) the same capacitors, or (**b**) different capacitors for actuation and sensing.

second configurations) has been obtained by averaging 32 actual measurements.

We will use the following convention to indicate the measurement set-up: we use the character "L" to indicate lateral actuation/sensing, i.e. when a voltage difference is applied (or the change in capacitance is sensed) between the rotor and the lateral stators; instead, we adopt the character "R" to indicate rotational actuation/sensing, i.e. when actuation (sensing) is applied (measured) through the rotational stators. Henceforth, there are four possible configurations (see Figure 3.6), labeled with a two character code: RR, RL, LR, LL. In our convention, the first character refers to the actuation while the second to the sensing; therefore, LL means that we actuate and sense along the lateral capacitor, while RL indicates an actuation is imposed via the top and bottom capacitors (i.e. at the rotational capacitors), and sensing is instead obtained through the lateral capacitor. Repeated digits measurements (RR, LL) are obtained by using only the digital capacimeter (limited to a maximum DC voltage of 40 V); different-in-characters coded measurements (RL, LR or cross ones) are instead related to configurations made possible by adding the DC power supply.

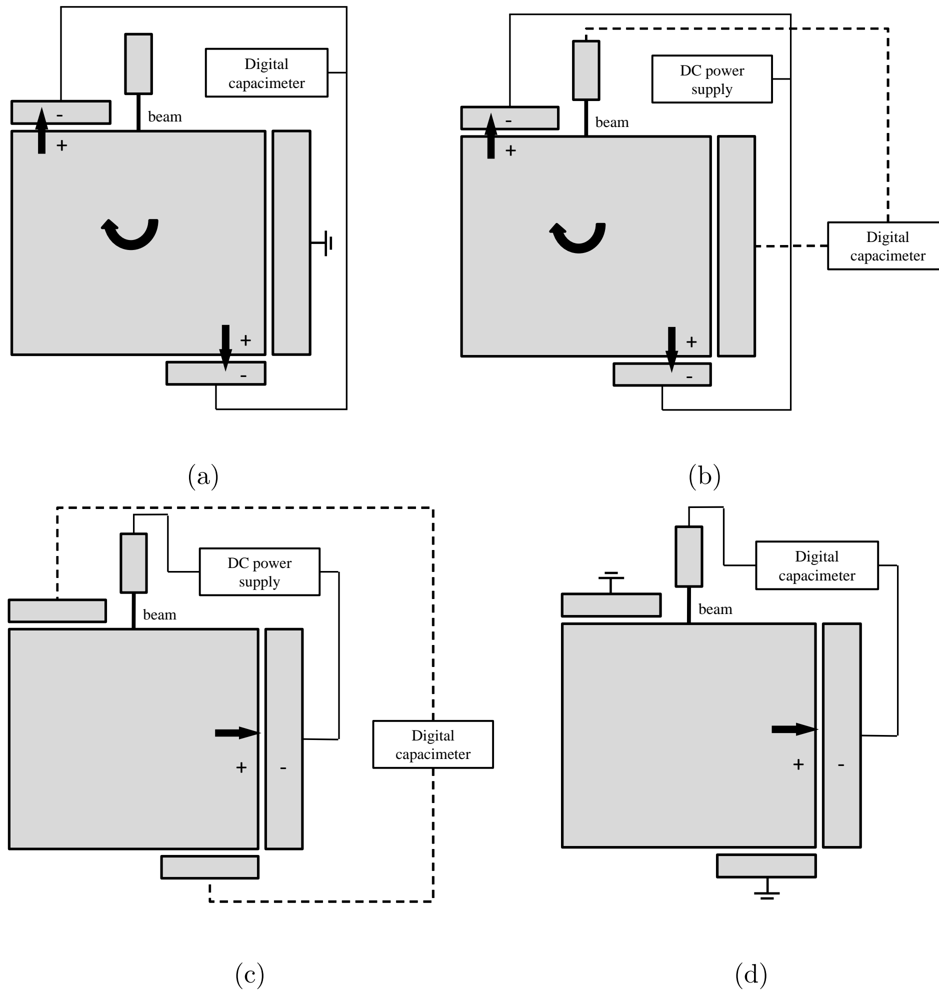

Figure 3.6: Experimental configurations: (**a**) RR (rotational actuation, rotational sensing), (**b**) RL (rotational actuation, lateral sensing), (**c**) LR (lateral actuation, rotational sensing), (**d**) LL (lateral actuation and sensing).

These four testing configurations allow to obtain different experimental measurements from the same device. Therefore, the conclusions formed on the basis of one set of data can be confronted with those formed based on another set of data (i.e. another configuration). Such property can be used as a cross-validation method for the forthcoming analyses.

It is worth noting that the movable components of the system are expected

to undergo in-plane (shown in Figure 3.2) motions only. This is ensured by i) electrically grounding the substrate so no bias voltage difference is created between the substrate and the rotor, and ii) realizing the stators and the rotor at the same plane[1]. It is also worthy of notice that, the structure is designed to be statically determinate to avoid developing major residual stresses due to the thermal processes (involved in the ThELMA process, see Chapter 2).

3.4 Experimental measurements

In what follows, we gather the results on the basis of the type of actuation: when the rotational capacitors are biased by DC voltage V_R, and when the lateral capacitor is biased by DC voltage V_L. Ten specimens are taken randomly from the same wafer for each beam length. Each module in the wafer accommodates different-in-length devices. The responses of these ten different devices, in terms of change in the capacitance values at increasing applied voltage for the rotational and lateral cases, are respectively reported in Figures 3.7 and 3.8 for $l = 20$ μm, and Figures 3.9 and 3.10 for $l = 10$ μm.

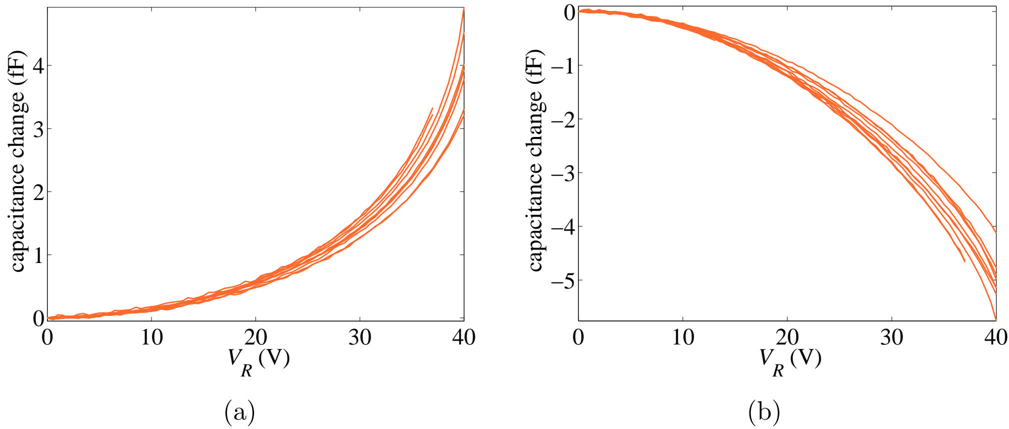

Figure 3.7: Experimental results for the device with beam length equal to 20 μm: (**a**) RR (rotational actuation, rotational sensing), (**b**) RL (rotational actuation, lateral sensing).

[1] The self-weight is not an issue in this device because of large up-scaling effect on the strength-to-weight ratio occurring at the micro sized devices.

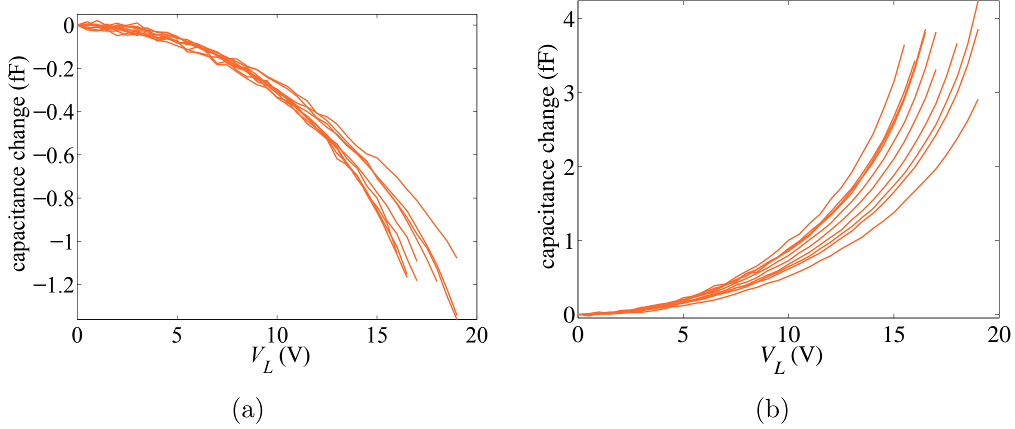

(a) (b)

Figure 3.8: Experimental results for the device with beam length equal to 20 μm: (**a**) LR (lateral actuation, rotational sensing), (**b**) LL (lateral actuation and sensing).

Full loading and unloading measurements have been carried out for each device; since an excellent repeatability has been observed, without hysteresis along loading and unloading cycles, only one measurement (loading) curve is reported for each device. Regarding the ultimate applied voltage, the actuation has been increased close up to the pull-in instability; since the target of the experimental campaign is not the assessment of the pull-in instability itself, which can damage the functionality of the devices by the consequent electrical short-circuit, some devices that have more compliant responses have been actuated up to lower voltage levels. The same strategy has been also adopted for the lateral actuation.

In the measured capacitance changes, either positive or negative values of the capacitance change are reported; the first ones appear when actuation and sensing are obtained with the same capacitors (RR or LL configurations), whereas the second ones in the case of cross capacitors (RL or LR configurations). Positive values mean that, due to the beam deformation, on the average a reduction of the gap with respect to the initial one has been induced; on the contrary, negative values mean that, once again on the average, conductors are moving away from one another. It can be also seen that the lateral actuation and sensing are more configurational responsive, as pull-in is approached for values of the applied voltage V_L amounting to around half of those necessary to approach pull-in under

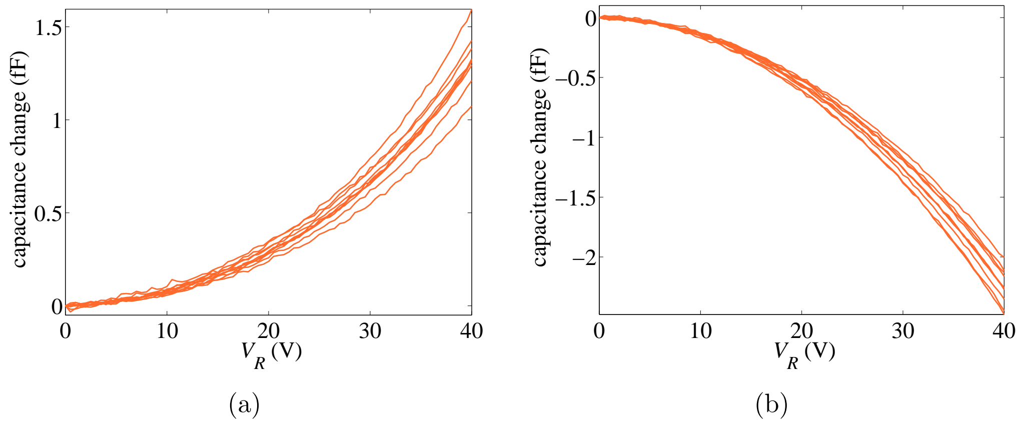

(a) (b)

Figure 3.9: Experimental results for the device with beam length equal to 10 μm:(a) RR (rotational actuation, rotational sensing), (b) RL (rotational actuation, lateral sensing).

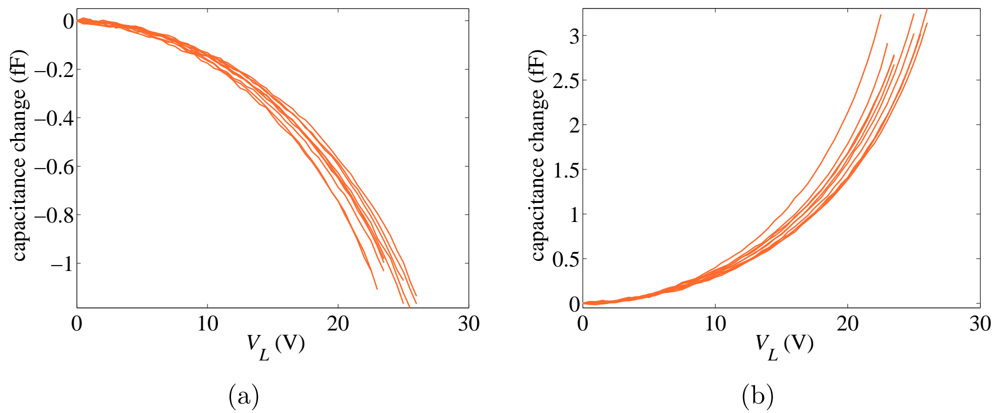

(a) (b)

Figure 3.10: Experimental results for the device with beam length equal to 10 μm: (**a**) LR (lateral actuation, rotational sensing), (**b**) LL (lateral actuation and sensing).

applied voltage V_R, measuring basically the same capacitance change. The effects of measurement noise are shown at low actuation levels but the measurement to error ratio improves as the level of actuation rises. This can be particularly seen in Figure 3.8(a), LR case, where the experimental curves are not smooth and several dips can be observed. It is worth noting once more, that each data point of each single curve in these figures are obtained via averaging 32 measurements to partly remove the random measurement noises.

3.5 Remarks

The measured $C - V$ curves show that the response of the devices is rather scattered. These large scatterings demonstrate the presence of uncertainties mentioned earlier in Chapter 2. The uncertainty sources can be related to the differences in grain structures or slight geometric differences among the specimens. These uncertainty sources have been also reported in a recent work, where variations of the measured Young's modulus are observed for micro cantilever bending test made of granular aluminum alloy [Bergers et al., 2014]. Though our study is on polysilicon, but the underlying phenomena are the similar.

Regarding the test devices in this work, the uncertainties linked to the micromechanical features of the polysilicon film is probably present since the specimens dimensions are in the same order of the grains average size. In addition to this source of uncertainty, there are items that can be taken into account to describe the reported scattering in the measurements. The most important one is the over-etch (see Chapter 2) that can affect the final layout of the device, such as the in-plane thickness of the micro beam or the electrostatic gap at the capacitors. The value of over-etch is dependent on the specific process adopted in the fabrication of the MEMS and in present work can be up ± 0.15 μm. Another candidate can be initial offset displacement of the central rotor which is prone to changes due to the fabrication process. This offset can affect the electromechanical; small rotor transversal displacement (in order of tens of nanometers) or rotation (in order of 1 milliradian) can be relatively large when the nominal gap in capacitors is only 2 μm. The over-etch in the ThELMA process is usually assumed to be homogeneous over the all regions of the device (i.e. constant value of over-etch),

however slight variations of over-etch value might be present in a device. Another possible fabrication inaccuracy can be linked to the assumption of planarity of the rotor. Though the structure is statically determinate and major residual stresses will not develop in the rotor, the rotor can be slightly out of plane with respect to the stators due to the fabrication errors at the beam anchor.

The uncertainties mentioned above can be similarly present in the commercial MEMS devices featuring similar components. In the rest of this work, an effort is put to address the main sources of uncertainties mentioned above to appropriately explain the observed scatterings. To this aim, in the next chapter we introduce two models developed to relate the recorded $C - V$ curves to the mechanical properties and geometric features of the device.

4

Modelling the test device

4.1 Introduction

Based on the experimental measurements carried out in the previous chapter, several investigations will be pursued in this thesis. Some of these investigations require models of the test device featuring low computational burden, and some others require models with specific details which are computationally demanding to be incorporated. In this chapter, we develop two different models that can relate the two electrical quantities: actuation voltage and the resultant capacitance changes at the capacitor sets. The first model is analytically derived by use of the beam theory and thus is computationally affordable. The second model is numerical and computationally demanding, though it is capable of taking into account more details of the device, such as the detailed polysilicon morphology.

In the following of this section, the description of the material models for the specimen are provided. The detailed formulation of the analytical model is then developed in Section 4.2, allowing for two physical domains: mechanical and electrical domains. Next, the finite element (FE) modelling of the test device, and the adopted stochastic strategy for accommodating the polysilicon morphology of the micro beam is described in Section 4.3. Finally, the features of these two models are explored in Section 4.4, by comparing their results to the experiments.

4.1.1 Material model

In order to derive appropriate models explaining the electromechanical behaviour of the devices, one should first describe the mechanical properties of polysilicon. A detailed material model description for polysilicon needs to take into account the generic morphology of silicon grains; so a heterogeneous description is needed. However, a simple homogeneous model is here first introduced as it turns worthwhile for the upcoming comparative analyses. It should be noted that due to the relatively small rigidity of the specimen with respect to the rotor, the deformation is expected to occur only at specimen, and the rotor just experiences a rigid body motion. So, we here focus on the material model for the specimen only.

Homogeneous case

The specimen (micro cantilever) is made of silicon grains with their crystallographic orientation statistically distributed rather than deterministically. We adopt a homogeneous model to investigate the possible bounds on the overall response. It is possible to define an in-plane isotropic or orthotropic model for the specimen in two extreme situations.

The isotropic paradigm can be associated to the situation where silicon grains are relatively small and the beam is composed of many grains. The values of isotropic model parameters, Young's modulus E and Poisson's ratio ν can be obtained via averaging the analytical Voigt and Reuss bounds on the elastic properties of silicon as: $E = 149.3$ GPa, $\nu = 0.172$ [Mariani et al., 2011].

The orthotropic model can be instead associated to two situations: the grains are relatively large enough to let the beam being composed of a single grain, or all grains share the same crystallographic orientation. Though these two cases are unlikely to occur, they are necessary to identify the range of possible response (also known as interval analysis) [Zhang et al., 2013].

Heterogeneous case

As mentioned earlier, the effective mechanical behaviour of the specimen depends on the characteristics of each single grain. Therefore, the constitutive behaviour of the material in the beam can be regarded as a piece-wise function of position

which varies from one grain to another. The mechanics inside each grain can be described by an orthotropic material model which depends on its crystallographic orientation. This behaviour can be expressed in terms of Eq. (2.7) in the local frame. Taking into account the random silicon crystal orientation, this relation can be expressed in the global frame through Eq. (2.8). The relevant elastic coefficients have been reported earlier in Table 2.1. The numerical model in Section 4.3 can accommodate this description.

4.2 Analytical modelling

4.2.1 Mechanical field

As explained in Section 3, the electrostatic actuation through any of the two sets of conductors induces a motion of the rotor plate which can be properly assumed to be an in-plane rigid body motion type, since its rigidity is relatively large with respect to the specimen. In view of this assumption, all the deformation is localized at the beam connecting the rotor to the substrate. Noting the large dimensions of rotor with respect to the gap g, the rotation of the rotor is expected to be within [-0.02 rad 0.01 rad] around the anchor point A (see Figure 3.2) at which the vertices of rotor get in touch with the capacitor surfaces (counterclockwise rotation is positive). The actual range of the rotation will be smaller since the pull-in instability occurs much earlier[1]. Regarding the set of tests featuring the 20 μm long beam, the shear effects can be neglected and the Euler-Bernoulli beam theory can be appropriately deployed. This assumption does not hold true for the beam length 10 μm, featuring a slenderness ratio of $l/h = 5$ and thus, the Timoshenko beam theory is accordingly adopted [Timoshenko and Woinowsky-Krieger, 1959]. In the following, the superscript E and T are used to denote the variables corresponding to the Euler-Bernoulli and Timoshenko theories, respectively.

Consider the tested micro beam with its length along the coordinate x, its cross section with area A and moment of inertia $I = wh^3/12$. Due to the mentioned admissible range of rotor rotation, we assume the deflections and strains at beam

[1] The actual rotation range will be shown in Chapter 7 to be approximately [-0.0088 rad 0.0042 rad].

scale linearly with load. The equations of equilibrium read

$$\frac{dF^E(x)}{dx} = -q(x) \tag{4.1}$$

$$\frac{dM^E(x)}{dx} = F^E(x) \tag{4.2}$$

where q is the transverse load and F^E and M^E denote transversal shearing force and bending moment of the Euler-Bernoulli beam, respectively. According to the Euler-Bernoulli beam theory for isotropic elastic materials, the stress resultants of the beam with Young's modulus E are given by

$$F^E(x) = -EI\frac{d^3u^E(x)}{dx^3} \tag{4.3}$$

$$M^E(x) = -EI\frac{d\theta^E(x)}{dx} = -EI\frac{d^2u^E(x)}{dx^2} \tag{4.4}$$

u^E and θ^E are, respectively, the Euler-Bernoulli transverse deflection of the beam neutral axis and the rotation of the cross section of the beam. Eq. (4.4) is derived under assumption of Euler-Bernoulli kinematics: the cross sections remain plane and normal to the deflected neutral axis, as shown in Figure 4.1. The governing equations of Euler-Bernoulli beam can be obtained by substituting Eq. (4.1) and Eq. (4.2) into Eq. (4.3) and Eq. (4.4) as

$$EI\frac{d^4u^E(x)}{dx^4} = -\frac{d^2M^E(x)}{dx^2} = q(x) \tag{4.5}$$

The mechanical response of the beam end-point $x = l$ due to end-point shear load $F^E(l)$ and moment $M^E(l)$ can be calculated from Eq. (4.5) using the boundary conditions $u^E(0) = \theta^E(0) = 0$ (i.e. constraints at the connection to the anchor) as

$$\left\{ \begin{array}{c} F^E(l) \\ M^E(l) \end{array} \right\} = \frac{EI}{l^3} \left[\begin{array}{cc} 12 & -6l \\ -6l & 4l^2 \end{array} \right] \left\{ \begin{array}{c} u^E(l) \\ \theta^E(l) \end{array} \right\} \tag{4.6}$$

Eq. (4.6) can be used to describe the mechanical deflection of the micro beams

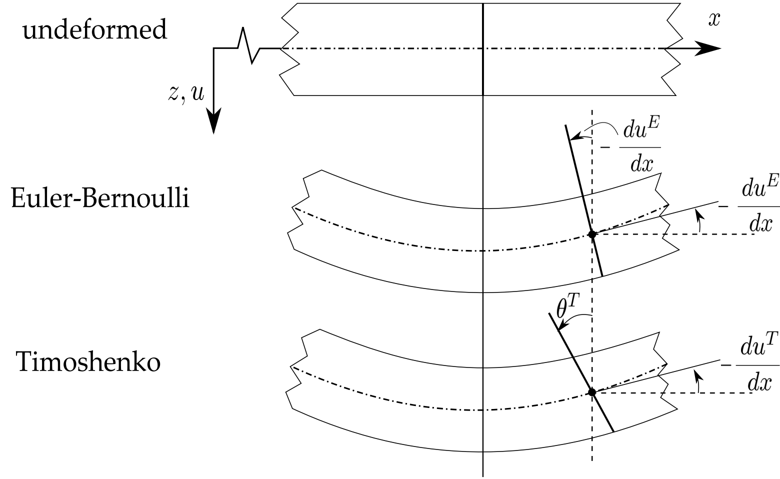

Figure 4.1: Deformation of a typical transverse normal line in Euler-Bernoulli and Timoshenko beam theories. u^E and u^T denote the transverse deflection (along z direction) of the beam neutral axis in Euler-Bernoulli and Timoshenko beam therories, respectively.

with $l = 20\ \mu$m. However, to correctly describe the mechanical response of the shorter beams, the Timoshenko beam model should be used. In this model, any cross section rotation along the beam axis is not anymore equal to the beam neutral axis rotation, as shown in Figure 4.1, and the stress resultants read

$$F^T(x) = -GA_s\kappa_s \left(\theta^T(x) - \frac{du^T(x)}{dx}\right) \tag{4.7}$$

$$M^T(x) = -EI\frac{d\theta^T(x)}{dx} \tag{4.8}$$

where G stands for the material shear modulus and κ_s is the shear correction factor which amounts to 5/6 for rectangular shape cross section. Similarly, substituting Eq. (4.7) and Eq. (4.8) into the equilibrium equations yields the the following governing equations for the Timoshenko beam

$$GA_s\kappa_s \left(\theta^T(x) - \frac{du^T(x)}{dx}\right) = EI\frac{d^2\theta^T(x)}{dx^2} \tag{4.9}$$

$$GA_s\kappa_s\left(\frac{d\theta^T(x)}{dx}-\frac{d^2u^T(x)}{dx^2}\right)=q(x) \tag{4.10}$$

The mechanical response of the beam can be again derived using the present boundary conditions $u^T(0) = \theta^T(0) = 0$ and expressed as a function of Euler-Bernoulli counterparts as

$$u^T(x) = u^E(x) + \frac{\Omega l^2}{EI}\left(M^E(x) - M^E(0)\right) \tag{4.11}$$

$$\theta^T(x) = \theta^E(x) \tag{4.12}$$

where the shear parameter Ω is defined as

$$\Omega = \frac{E}{G\kappa_s}\left(\frac{l}{r}\right)^{-2} \tag{4.13}$$

$r = \sqrt{I/A_s}$ is the radius of gyration and l/r is the slenderness ratio of the beam. It should be noted that Eq. (4.11) and Eq. (4.12) are derived according to the assumed boundary conditions and do not generally hold true. Therefore, the following system of equations can be written to describe the mechanical response of the end-point of of short micro beams with $l = 10$ μm

$$\left\{\begin{array}{c} F^T(l) \\ M^T(l) \end{array}\right\} = \frac{EI}{l^3}\left[\begin{array}{cc} 12 & -6l \\ -6l & 4l^2 \end{array}\right]\left\{\begin{array}{c} u^T(l) - \frac{\Omega l^3}{EI}F^T(l) \\ \theta^T(l) \end{array}\right\} \tag{4.14}$$

Eq. (4.6) and (4.14) link the load vector $\{F(l) \quad M(l)\}^{\mathrm{T}}$ as the mechanical input to the mechanical response of the micro beams in terms of the deflection and rotation of the end-point $\{u(l) \quad \theta(l)\}^{\mathrm{T}}$ as the output. Superscript $^{\mathrm{T}}$ stands for transpose. These two quantities then need to be translated to the electrical actuation and sensing. In the rest of this work, the end-point variables $u(l), \theta(l), F(l)$ and $M(l)$ are simply referred as u, θ, F and M, respectively.

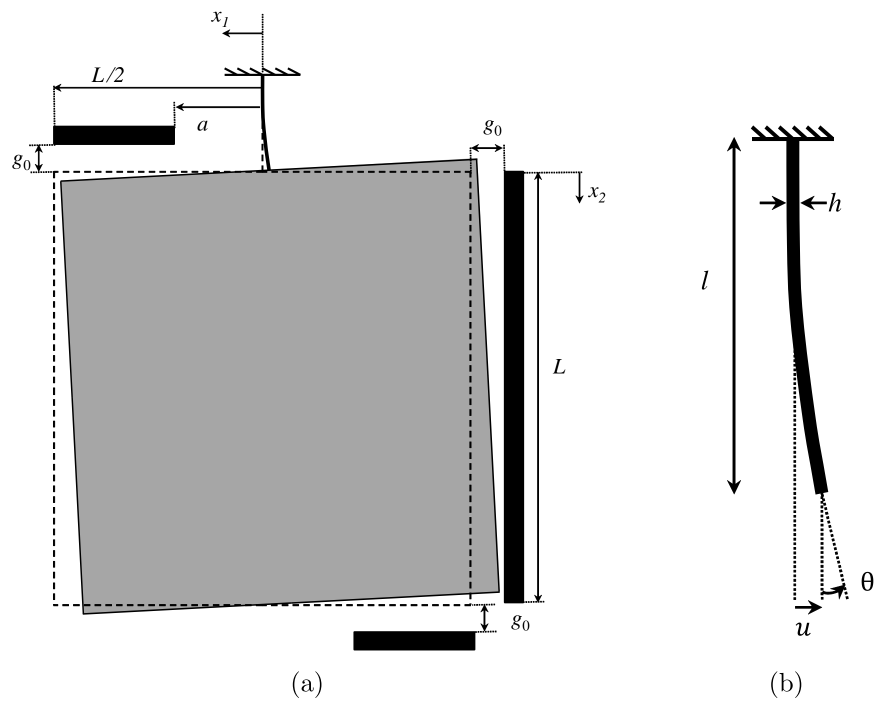

Figure 4.2: (**a**) Schematic of the behaviour of the whole test structure in the case of lateral actuation, and (**b**) close-up of the deflected micro beam.

4.2.2 Electrical field

Actuation

As mentioned, the mechanical quantities should be transformed into the electrical counterparts since the direct output of the experiments are $C-V$ curves. To this aim, the capacitance per unit area c of the parallel plate capacitor with a gap space g reads

$$c = \frac{\epsilon}{g} \tag{4.15}$$

where $\epsilon = \epsilon_r \epsilon_o$, ϵ_r is the relative permittivity of the medium, and ϵ_0 is the dielectric constant in the free space. Accordingly, the potential energy of the capacitance is

$$\mathbb{E} = \frac{1}{2} c V^2 \tag{4.16}$$

By definition, the attraction electrostatic force per unit area is the change in the potential energy due to changes in the gap space, that is

$$f = \frac{\epsilon V^2}{2g^2} \tag{4.17}$$

Assuming that the electrical potential difference between plates remains constant, the unit attraction force is simply a nonlinear function of the gap space g.

At a constant voltage V, Eq. (4.15) and Eq. (4.17) show that the capacitance and the electrostatic force are inherently nonlinear functions of the gap space g in case of parallel plate capacitors. In the following, the values of F and M are calculated for the rotational and lateral actuations cases separately. In all calculations, the electric fringe field is neglected. In electrostatic problems involving unguarded parallel plate capacitors, the inter-conductor electric field departs from uniformity near the plate edges, and extends into space beyond the conductors. The departures from ideal uniform field behaviour are often referred to as fringe field effect [Sloggett et al., 1986]. Thanks to the designed capacitors, we can adopt parallel plates approximation, large ratio between capacitor length and the gap, and neglect the fringe field effect.

In rotational actuation, the stators are set to an electrical potential V_R, while the rotor is electrically grounded. Under the assumption of rotation dominated

motion and negligible effect of lateral displacements on the configuration along the capacitor surfaces, the gap g_R between the conductors of the rotational capacitors can be expressed as a function of rotation angle given by:

$$g_R = g_0 + x_1 \sin\theta \tag{4.18}$$

where g_0 is the initial gap in the absence of any electrostatic actuation, and x_1 is reported in Figure 4.2. Since the rotation angle θ is supposed to be small for any possible actuation up to pull-in, Eq. (4.18) is assumed to hold true for both the top and bottom capacitors. For this configuration, the shear force is thus zero, i.e.

$$F_R = 0 \tag{4.19}$$

while the bending moment reads

$$\begin{aligned} M_R &= -2\int_a^{L/2} \frac{\epsilon w V_R^2}{2(g_0 + x_1 \sin\theta)^2} x_1 dx_1 \\ &= \frac{\epsilon w V_R^2}{\sin^2\theta}\left(\frac{(g_0 + a\sin\theta)\log(g_0 + a\sin\theta) + g_0}{g_0 + a\sin\theta}\right. \\ &\quad \left. - \frac{\left(g_0 + \frac{L}{2}\sin\theta\right)\log\left(g_0 + \frac{L}{2}\sin\theta\right) + g_0}{g_0 + \frac{L}{2}\sin\theta}\right) \end{aligned} \tag{4.20}$$

where a and L are the geometric parameters defined in Figure 4.2(a) and w is the polysilicon layer thickness.

The relevant relations for the lateral actuation case can be similarly derived. In this second case, the rotor is still electrically grounded, while the stator conductor of the lateral capacitor is set to an electrical potential V_L. Unlike the rotational case, the gap along the lateral surface of the proof mass is not only a function of the rotation angle θ but also of the lateral displacement u. Accordingly, the gap can be written as:

$$g_L = g_0 - u - x_2 \sin\theta \tag{4.21}$$

where the local coordinate axis x_2 is shown in Figure 4.2. The shear force and the bending moment are thus provided by

$$F_L = \int_0^L \frac{\epsilon w V_L^2}{2(g_0 - u - x_2\sin\theta)^2} dx_2 = \frac{\epsilon w V_L^2 L}{2\,(g_0 - u)\,(g_0 - u - L\sin\theta)} \tag{4.22}$$

and

$$\begin{aligned} M_L &= \int_0^L \frac{\epsilon w V_L^2}{2(g_0 - u - x_2 \sin\theta)^2} x_2 dx_2 \\ &= \frac{\epsilon w V_L^2}{2\sin^2\theta} \left(\frac{g_0 - u}{g_0 - u - L\sin\theta} + \log\left(-g_0 + u + L\sin\theta\right) - \log\left(-g_0 + u\right) - 1 \right) \end{aligned} \tag{4.23}$$

Since sensing, either the rotational or the lateral one, is independent of the adopted actuation strategy, a discussion is reported next separately.

Sensing

A similar methodology can be adopted for sensing. Neglecting once again the electric fringe field, the capacitance between the plates is computed through Eq. (4.15), handling the gap g as a function of the kinematic variables u and θ and integrating over the surfaces of the capacitors. In the initial configuration with a gap equal to g_0 all around the rotor, values of rotational and lateral capacitances, respectively, read

$$C_{R0} = 2\int_a^{L/2} \frac{\epsilon w}{g_0} dx_1 = 2\frac{\epsilon w(\frac{L}{2} - a)}{g_0} \tag{4.24}$$

$$C_{L0} = \int_0^L \frac{\epsilon w}{g_0} dx_2 = \frac{\epsilon w L}{g_0} \tag{4.25}$$

In the displaced configuration they instead amount to

$$\begin{aligned} C_R &= 2\int_a^{L/2} \frac{\epsilon w}{g_0 + x_1\sin\theta} dx_1 \\ &= \frac{2\epsilon w}{\sin\theta} \left(\log\left(g_0 + \frac{L}{2}\sin\theta\right) - \log\left(g_0 + a\sin\theta\right) \right) \end{aligned} \tag{4.26}$$

$$\begin{aligned} C_L &= \int_0^L \frac{\epsilon w}{g_0 - u - x_2\sin\theta} dx_2 \\ &= \frac{\epsilon w}{\sin\theta} \left(\log\left(-g_0 + u\right) - \log\left(-g_0 + u + L\sin\theta\right) \right) \end{aligned} \tag{4.27}$$

where the same approximations introduced for the actuation have been exploited.

Analytical modelling is beneficial as it is computationally fast, nonetheless it suffers from some limitations that can be improved by finite element modelling. We assumed a homogeneous material in the beam model while the real beam is made from polysilicon which is a heterogeneous material. Furthermore, the beam is assumed to be perfectly anchored, but small deformations of anchor is possible in MEMS application [Lam et al., 2003]. In addition, we assumed equal electrical fields at top and bottom capacitors. In reality, they are slightly different as the rotor rotation is not around its center but around its connecting point to the beam (point “A” in Figure 3.2). To overcome these issues, a finite element model is further developed.

4.3 Finite element modelling

To model the quasi static behaviour of the device, the coupling between electrostatic and elastic forces needs to be established. As the mechanical deformation increases due to the electrical actuation, the electrical domain changes accordingly and the space discretization should properly account for these changes. The technique adopted here belongs to the family of staggered procedures, iterating between the mechanical and electric fields, transferring the load vectors between these two domains. The coupled-field finite element (FE) model of the test device has been elaborated in the commercial code ANSYS Mechanical APDL (Release 15.0). In the two-dimensional model (plane strain assumption; out of plane thickness of the device w is 11 times larger than the beam thickness h), the structural components are modeled by 6-node, quadratic, triangular elements with displacement degrees of freedom, while the electric domains (air) between the conductors are modeled by 3-node, linear, triangular elements with both displacement and voltage degrees of freedom. It is necessary to take the geometric nonlinearities into account in order to appropriately model the distortions of the narrow gap between the conductors when the value of actuation voltage approaches pull-in (which are taken into account analytically through Eq. (4.18) and Eq. (4.21)).

To create the polysilicon morphology at the beam, a phenomenological approach has been adopted. In the real fabrication procedure, the silicon grains are first grown on the substrate independent of the final structure features as

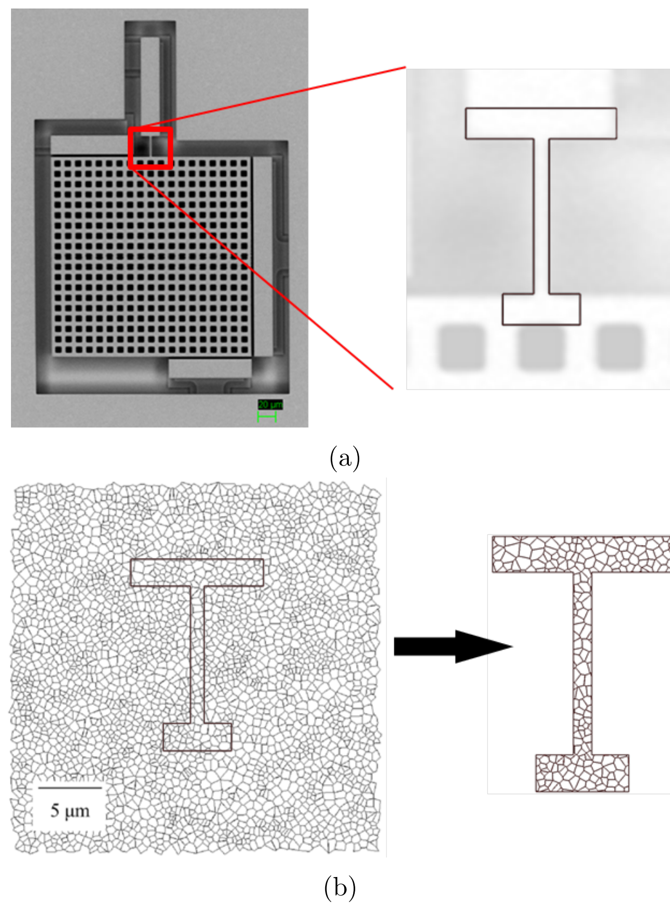

Figure 4.3: (**a**) Layout of the specimen and, (**b**) Voronoi artificial tessellation used to reconstruct the micro beam polysilicon morphology, and (magnified) example of the grain morphology in the micro beam region.

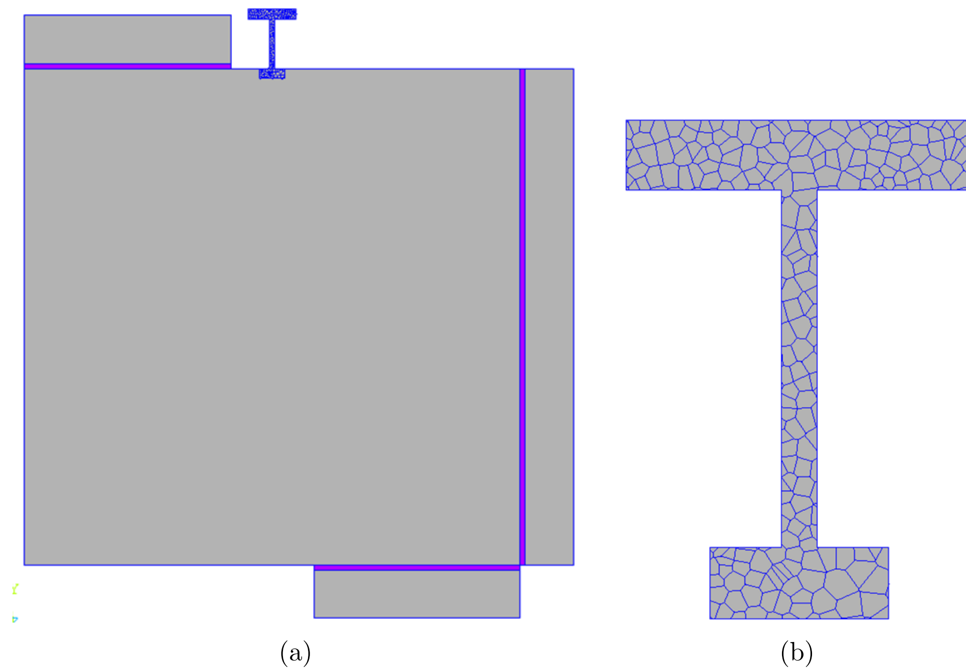

(a) (b)

Figure 4.4: (**a**) Adopted model of the geometry and (**b**) a random grain morphology in the micro beam region.

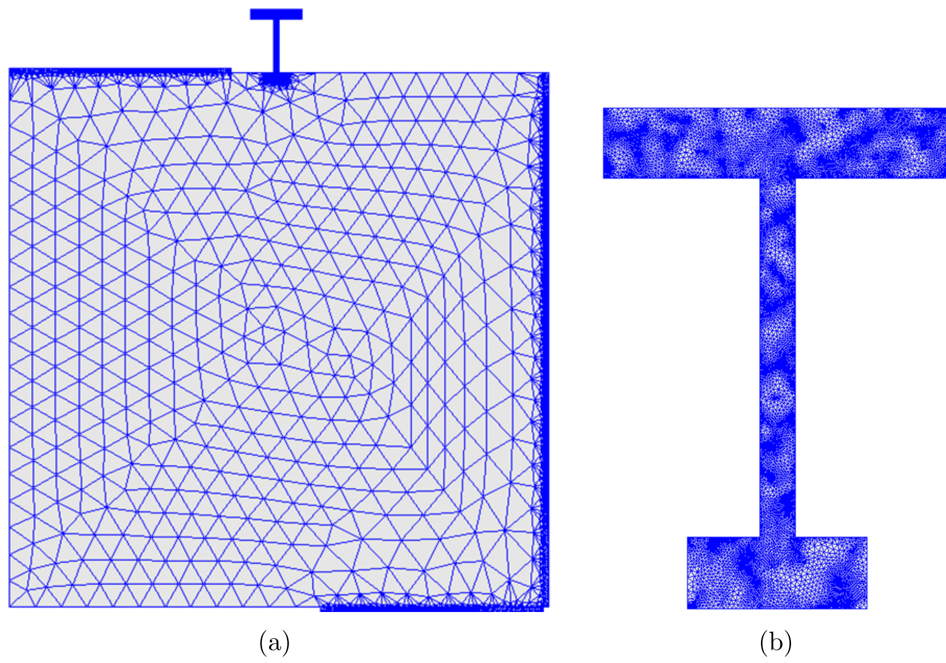

Figure 4.5: (**a**) FE discretization and (**b**) detail of the mesh in the micro beam region, accounting for random grain morphology.

described in Chapter 2. Then the outline of the structure is etched through appropriate masks. As a result, the final device is composed of some whole grains and some others locating in the device border where they are cut by the etching process. Similarly, considering the Voronoi tessellation explained in Chapter 2, the layout of the specimen can be extracted from the tessellation through appropriate Boolean operations. The area at the two ends of the beam are also considered to allow for the polysilicon morphology effect in the overall response. This so-called moving window technique is reported schematically in Figure 4.3. The adopted model of the device geometry and an example of resulting grains at the beam (including the two beam ends) are also depicted in Figure 4.4. The corresponding generated FEs are exemplified in Figure 4.5. It is noted that the mesh size is very fine at the beam area where the grains are modelled, and large at the rotor where we expect no deformation to develop. The adopted FE model consists a total number of 30500 3-node elements at the gaps and around 4800 6-node elements for $l = 20$ μm resulting a total number of 75300 nodes. As for $l = 10$ μm, the elements at the gaps are identical, but the number of structural elements decreases to 25500, resulting a total number of 62200 nodes. These numbers vary as the adopted grain morphology changes.

4.4 Results

The models provided in the previous section naturally depend on the geometric and material parameters. Despite the scattering observed in the experimental measurements, here we report examples of analytical/numerical predictions using the nominal design parameters for the geometry and the homogenized isotropic constitutive model for polysilicon. Figures 4.6 and 4.7 illustrate the $C-V$ curves of the beam length equal to 20 μm for rotational and the lateral actuation cases, respectively. Similarly, Figures 4.8 and 4.9 report the results for beam length equal to 10 μm. These figures compare the analytical/numerical results versus the experimental measurements.

It is clear from the responses that both the analytical/numerical models can provide results in agreement with the experimental measurements for the four testing configurations. The analytical model can model the capacitance changes

at actuation voltage values up to the pull-in, while the numerical model stops slightly before pull-in voltage. Overall, both the models predict moderately less capacitance change compared to the measured values. This implies that the models are either mechanically stiffer or the electrical domain is not representing the generated field perfectly. This issue can be related to the assumptions adopted to develop each model. As the numerical model is concerned, the electric fringe field at the two ends of the capacitors and at the out-of-plane edges has been neglected. These assumptions have been also used to develop the analytical model. In addition, in the mechanical part of the analytical model we assumed a perfect anchor at the beam ends; during bending, the load-displacement behaviour is potentially affected by the compliance of the anchor which depends on the specific shape, size and detailed material properties of the anchor (which can be included in a finite element analysis, for instance) [Lam et al., 2003]. The anchor effect is more evident when the results are compared for the two beam lengths: by decreasing the length of the beam from 20 μm to 10 μm the difference between the two models increases. Therefore, the effect of deformations at the anchors are more evident in the shorter beams [Lam et al., 2003], suggesting that the developed finite element model is more appropriate for the shorter beams.

Another important issue that must be noted is the computational effort needed for these models. A personal computer with an Intel®Core™ i7 3.00 GHz processor is used for the simulations. Computing time for the FE model on this computer can be up 30 min depending on the beam length and the testing configuration (i.e. RR, RL, LR and LL) considered. On the contrary, the analytical model is extremely cheaper taking only up to 2 seconds depending on the testing configuration.

In the rest of this work, we use the developed models to carry out several investigations to link the experimentally measured scatterings to different uncertainty sources.

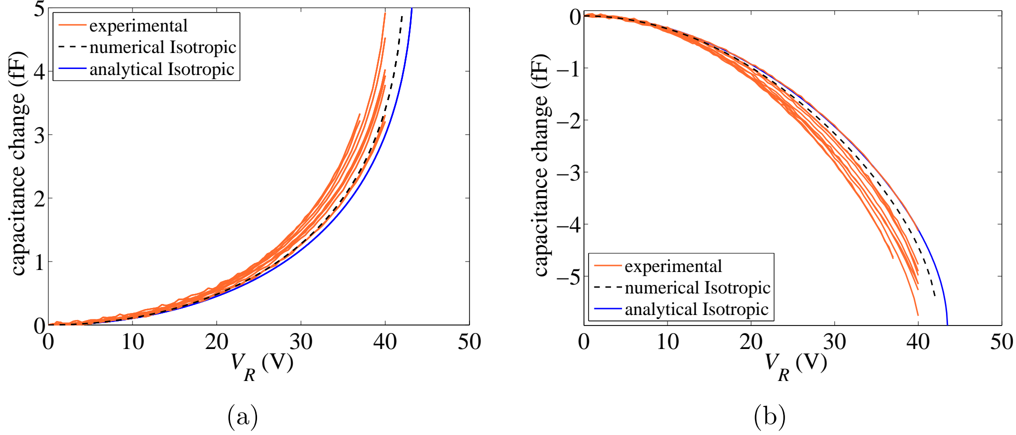

Figure 4.6: Experimental measurements versus results of numerical and analytical model for specimen with beam length equal to 20 μm: (**a**) RR (rotational actuation, rotational sensing), (**b**) RL (rotational actuation and lateral sensing).

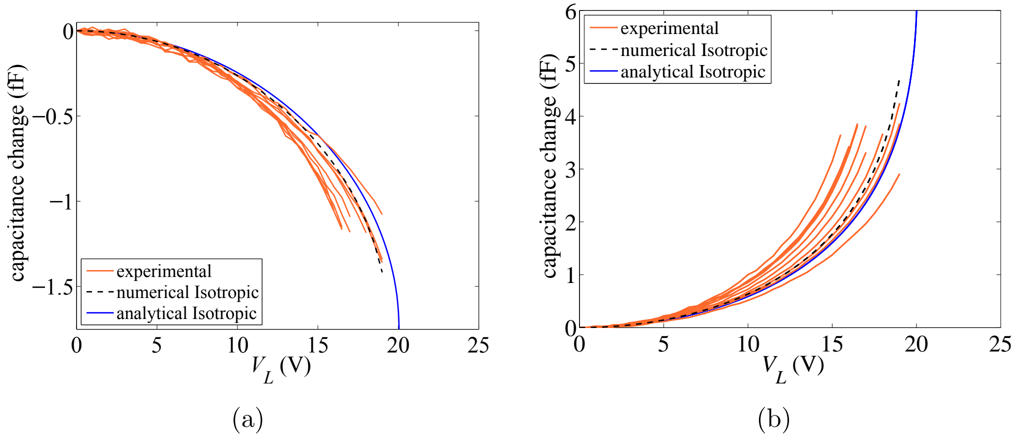

Figure 4.7: Experimental measurements versus results of numerical and analytical model for specimen with beam length equal to 20 μm: (**a**) LR (lateral actuation, rotational sensing), (**b**) LL (lateral actuation and lateral sensing).

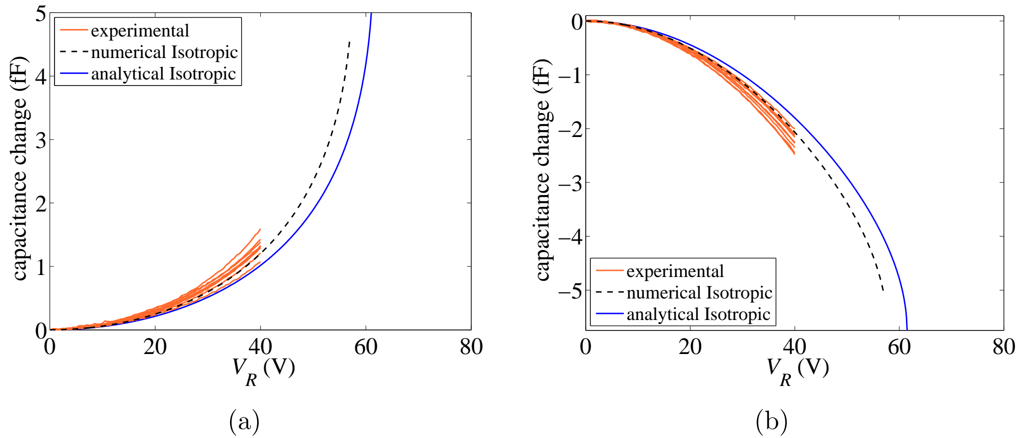

Figure 4.8: Experimental measurements versus results of numerical and analytical model for specimen with beam length equal to 10 μm: (**a**) RR (rotational actuation, rotational sensing), (**b**) RL (rotational actuation and lateral sensing).

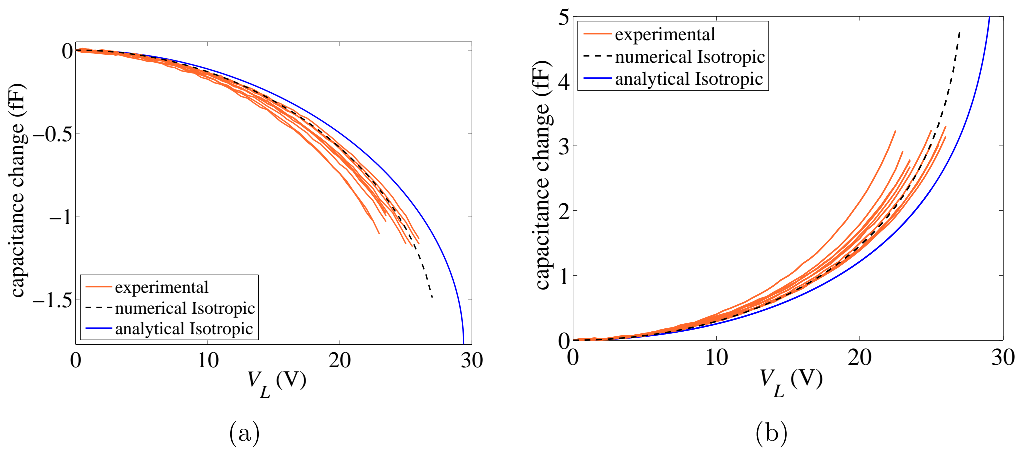

Figure 4.9: Experimental measurements versus results of numerical and analytical model for specimen with beam length equal to 10 μm: (**a**) LR (lateral actuation, rotational sensing), (**b**) LL (lateral actuation and lateral sensing).

5

Mechanically induced uncertainties on the experimental measurements

5.1 Introduction

In this chapter, we conduct a thorough study on the effects of polysilicon morphology on the observed scattering in the experimental measurements. Several sources of uncertainties may co-exist effecting the response of the devices (see Chapter 3); therefore, a clear distinction among their individual effects is not obvious. The sources of uncertainties can be categorized into two groups: ones related to the variation of the mechanical properties, and ones instead linked to the fabrication inaccuracies. We focus in this chapter on the former which is not particular to our device but may exist in any device fabricated from granular materials and featuring components with characteristic size comparable to the average grain size.

To this aim, we use the admissible elastic properties of the silicon grains to establish a set of bounds for the electromechanical response of the tested devices. These bounds do not take into account the microstructure of polysilicon and provide only the maximum scattering that could have developed due to the variations in the polysilicon mechanical properties. In the next step, the effort is put to relate the details polysilicon microstructural variations to the scatterings of the device

response. This is done using two Monte Carlo simulations by adopting either the analytical model or numerical model developed in Chapter 4. In the former one, a preliminary Monte Carlo simulation is first employed to derive the probability density function (PDF) of the effective elastic properties of stochastic samples of polysilicon morphology. These PDFs are then fed into the analytical model in the frame of the main Monte Carlo study, to reproduce the $C - V$ curves for each testing configuration. In the latter, we generate random grains directly at the specimens to compute the $C - V$ curves. It is observed that the Monte Carlo simulation using the numerical model yields results in better agreement with the experimental measurements. Two important conclusions are drawn accordingly: i) the variation of mechanical properties due to the polysilicon morphology is more important in the shorter beam, ii) the fabrication inaccuracies induce larger uncertainties in the electromechanical response.

The chapter starts with reviewing the admissible elastic properties of silicon in Section 5.2 and then in Section 5.3 the bounds on the $C-V$ curves are derived using these elastic properties. In Section 5.4, the investigations using Monte Carlo simulations are introduced. First, Section 5.4.1 addresses the the strategies adopted to allow for elastic properties variations and then Section 5.4.2 discusses the convergence of the Monte Carlo simulations. Finally, Section 5.4.3 reports and discusses the results of the Monte Carlo studies using the analytical and the numerical models.

5.2 Admissible elastic properties

To study the possible effect of the uncertainties in the mechanical properties of polysilicon micro beam on the electromechanical response of the devices, one can assume that the micro beam is composed of fictitious single crystalline silicon, featuring either the maximum or the minimum effective Young's modulus along the beam axis (see Chapter 4). These two conditions are called in this work "stiff" and "compliant" case, respectively. These two cases feature the longitudinal axis of the beam aligned with either crystal orientation $\langle 110 \rangle$ or $\langle 100 \rangle$, respectively. These two situations are reported in Figure 2.3. Accordingly, we have Young's modulus $E = 130$ GPa, shear modulus $G = 79.6$ GPa and Poisson's ratio $\nu = 0.28$

for the compliant case, and after an in-plane rotation of the reference coordinate system by $\pi/4$, we have the stiff case as E = 169 GPa, G = 50.9 GPa and $\nu = 0.064$. These two sets of values show, respectively, the minimum and the maximum of the effective mechanical properties of silicon at the silicon plane (100), see again Figure 2.3.

Another interesting comparison can be also made by using for the overall elastic properties the mean values between analytical Voigt and Reuss bounds[1]: Young's modulus E =149.3 GPa and Poisson's ratio $\nu = 0.172$ [Mariani et al., 2011]. This case is identified here as the "isotropic" case. The elastic properties of all these cases are gathered in Table 5.1. These cases can be used to either obtain bounds on the measured response or define a nominal expected response. In the next section, these cases are discussed.

Table 5.1: Elastic constants for comparison cases.

	E (GPa)	G (GPa)	ν
stiff	169	50.9	0.064
isotropic	149.3	63.7	0.172
compliant	130	79.6	0.28

5.3 Mechanical bounds on the measurement scattering

The measured $C - V$ curves in Chapter 3 are scattered due to the presence of some sources of uncertainties. It is useful to investigate the maximum effects that variations in the specimen mechanical properties can have on the electromechanical responses. Figures 5.1 and 5.2 report the response bounds for the beam length $l = 20$ μm with rotational and lateral actuation, respectively. Similarly, Figures 5.3 and 5.4 report the bounds for $l = 10$ μm. These responses have been obtained using the mechanical properties in Table 5.1 using the numerical model introduced in Chapter 4. We use the numerical model since it can provide more appropriate estimates of the system behaviour (see Chapter 4). It can be seen that

[1] Voigt and Reuss approaches are known to provide bilateral bounding for the elastic moduli of multiphase systems by assuming, respectively, the state of strain and stress to be uniform inside the corresponding representative volume element.

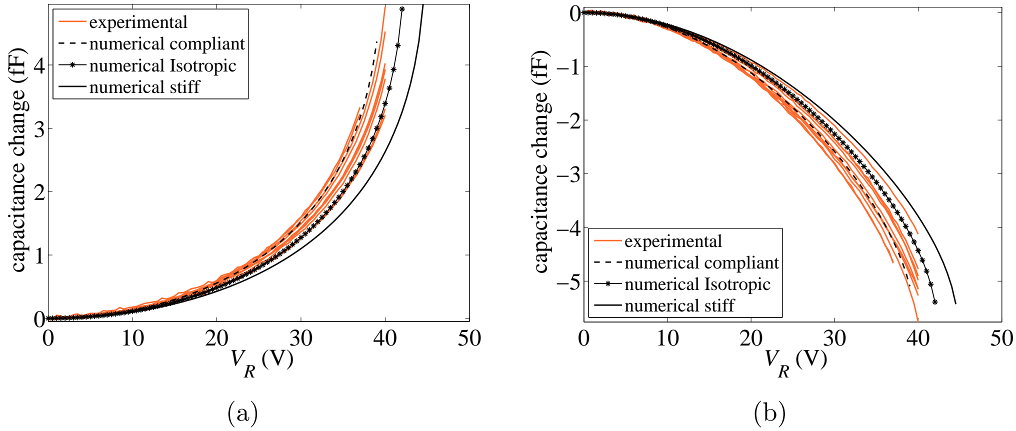

Figure 5.1: Experimental responses in terms of capacitance change and acutation voltage vs numerical bounds obtained by using maximum, minimum and homogenized values of E and relevant ν for the devices whose beam length is equal to 20 μm: (**a**) RR, (**b**) RL.

the isotropic case shows a moderate agreement with the measured responses. The bounds instead can cover most of the measured responses at both beam lengths. If one takes the effects of electric fringe field into account, a slight shift of the curves toward larger capacitances is expected. The fringe fields at the two ends of the conductors can contribute in the electrostatic traction force, but its value is expected to be low due to the long length of the conductors with respect the gap space (see Section 4.2).

Despite the good coverage of the bounds, some measured data fall out of these bounds. Nevertheless, the bounds provided by the stiff and compliant cases are unlikely to happen, as they would imply either that all grains in the micro beam share the same crystalline orientation or that the beam is formed from one large single crystal. Such observation clearly shows that the scattering of the responses cannot be explained only through variations of the mechanical properties of the polysilicon film.

Though this analysis can give the maximum possible scattering of electromechanical responses due to the variations in the mechanical properties, it fails to provide a clear understanding of the response probability. In order to get such insight, statistical studies through Monte Carlo simulations are carried out in

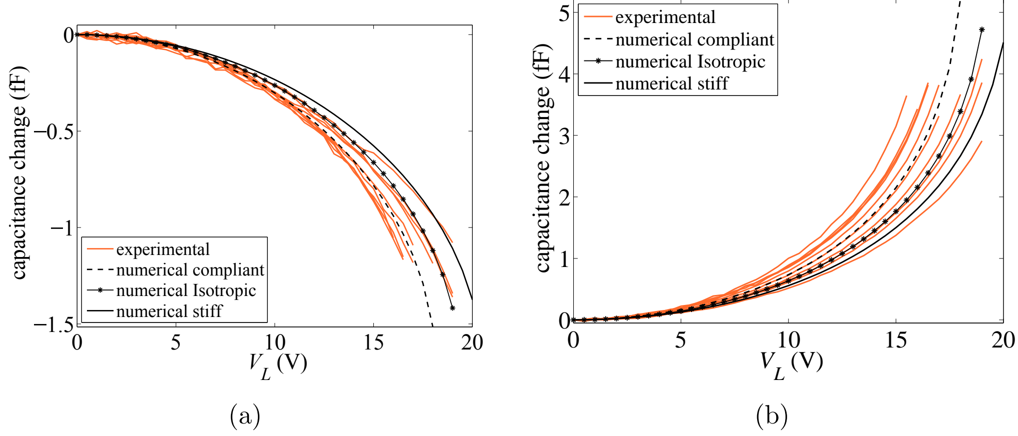

(a) (b)

Figure 5.2: Experimental responses in terms of capacitance change and acutation voltage vs numerical bounds obtained by using maximum, minimum and homogenized values of E and relevant ν for the devices whose beam length is equal to 20 μm: (**a**) LR, (**b**) LL.

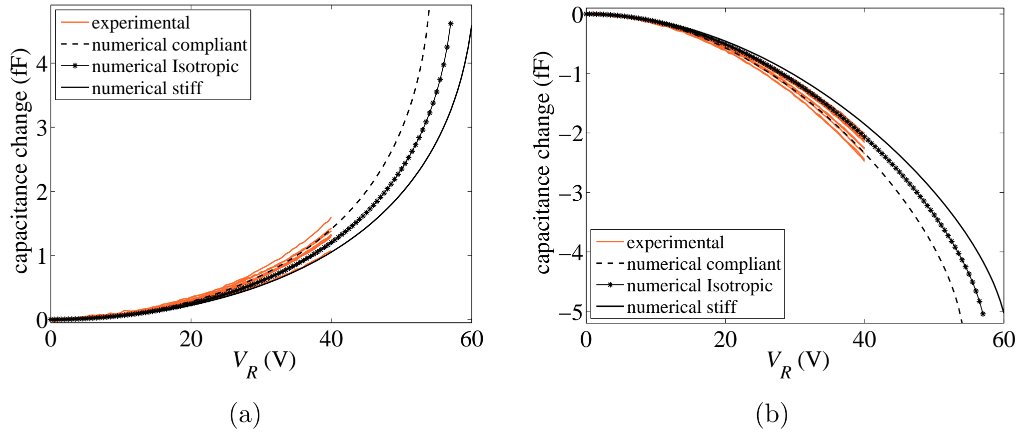

(a) (b)

Figure 5.3: Experimental responses in terms of capacitance change and acutation voltage vs numerical bounds obtained by using maximum, minimum and homogenized values of E and relevant ν for the devices whose beam length is equal to 10 μm: (**a**) RR, (**b**) RL.

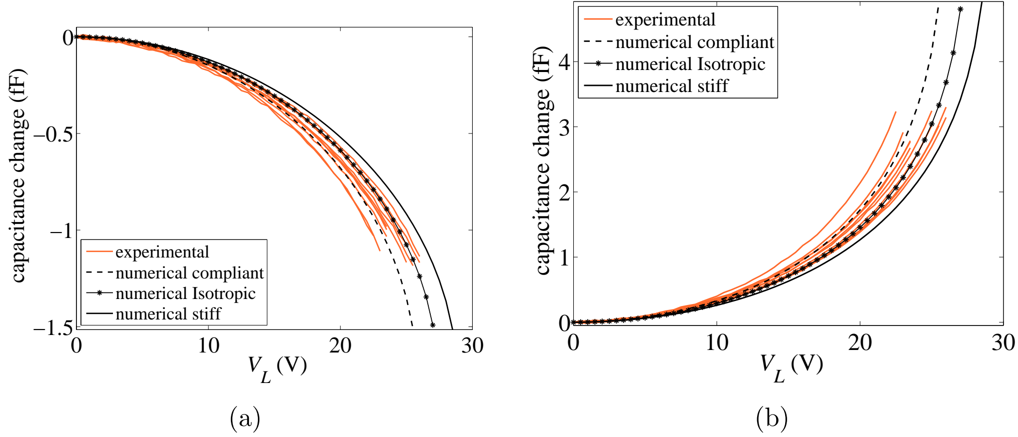

(a) (b)

Figure 5.4: Experimental responses in terms of capacitance change and acutation voltage vs numerical bounds obtained by using maximum, minimum and homogenized values of E and relevant ν for the devices whose beam length is equal to 10 μm: (**a**) LR, (**b**) LL.

the next section. In the simulations that follow, we investigate the effects of the variations of polysilicon morphology (including grains orientations) on the electromechanical response of the devices.

5.4 Monte Carlo simulation allowing for elastic properties variation

5.4.1 Mechanical properties variations due to the microstructure

In order to have a more precise understanding of the effects of material properties variations on the observed scattering of the electromechanical responses in Chapter 3, a Monte Carlo (MC) approach is adopted. The idea behind MC is to propagate the uncertainties present in the inputs of a nonlinear model to its output by carrying out a (usually large) number of simulations at varying inputs. We follow two sets of Monte Carlo simulations adopting either the FE model or the analytical model of the test device introduced earlier.

The FE model is advantageous because we can explicitly model the polysilicon morphology. The idea of using the FE model in the Monte Carlo study is to assign

random polysilicon morphology and grain orientation and obtain the $C-V$ curves corresponding to that specific polysilicon film at the micro beam. Therefore, the reconstructed scattering of the $C-V$ curves can be confronted to that of experimental campaign. In order to use the FE model, we resort to the moving window technique described in Section 4.3. For each simulation (of Monte Carlo method), a different morphology with an orientation randomly assigned to each grain is considered for the specimen and the region around its two ends, see Figure 4.3. A FE discretization is then applied; since several FEs have to be assigned to each grain, it is easily understood that the method is computationally expensive, taking also into account the large number of simulations necessary to ensure the convergence of the Monte Carlo simulations. To overcome the drawback of the computational burden, in addition to the previously mentioned MC FE-based model, a MC based on the simple analytical model reported in Chapter 4 has been also developed.

In the analytical model, the polysilicon grains cannot be reproduced in an explicit manner; the model accepts the elastic moduli. The MC using this model is in turn based on the statistics of the elastic properties of polysilicon film, built on the basis of the method proposed in [Mariani et al., 2011]. This approach, in fact, is able to numerically characterize the statistics of the overall elastic moduli of polysilicon with a given morphology. To obtain this result, we focus on an aggregate of silicon grains within a two-dimensional statistical volume element (SVE) and generate the polycrystal morphologies using the Voronoi tessellation-based method. A preliminary MC approach accounts for the stochastic features of the polysilicon morphology in the SVE, such as the grain boundary geometry and the crystal lattice orientations of each grain.

Allowing for estimation fluctuations thanks to the just described procedure, we can obtain bounds on the overall elastic moduli by adopting uniform strain as well as uniform stress along the boundaries of the SVE. If the SVE has a statistically representative number of grains (i.e. the SVE contains a larges enough number of grains), the estimated values for elastic moduli should not depend on the type of adopted BCs. As such condition is not valid for the problem in hand, using the uniform strain and stress BCs result in an statistical upper and lower bound, respectively [Mariani et al., 2011]. The elastic moduli for each SVE are then

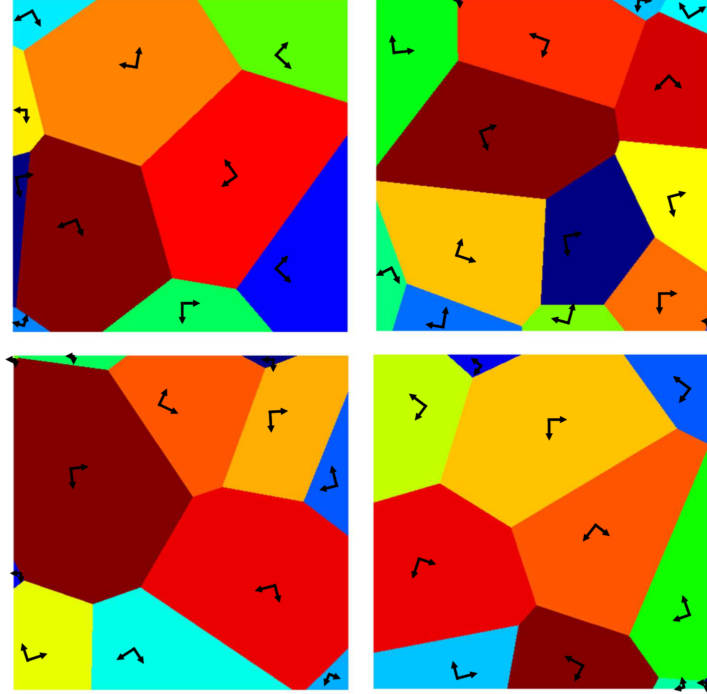

Figure 5.5: Examples of 2 μm $\times$ 2 μm SVEs of polysilicon used in the preliminary MC simulations.

computed with standard FE simulations with these BCs. Overall, 100 random SVEs are obtained from an artificial Voronoi tessellation featuring an average silicon grain size (in terms of diameter) equal to 0.5 μm, typical for our MEMS devices. Examples of these SVEs are shown in Figure 5.5. The SVE side length is chosen to be 2 μm in accordance with the in-plane width of the micro beam.

The results of this preliminary MC simulations are reported in the form of a statistical cumulative distribution function (CDF), shown in Figure 5.6 for the Young's modulus E and the shear modulus G (inputs of Eq. (4.14)). The analytical representations of these distributions are established in the form of lognormal distribution whose probability density function (PDF) reads

$$f(\chi) = \frac{1}{\chi \sigma_{LN} \sqrt{2\,\pi}} \exp\left[-\frac{1}{2\,\sigma_{LN}^2} \left(\log(\chi) - \mu_{LN}\right)^2 \right] \tag{5.1}$$

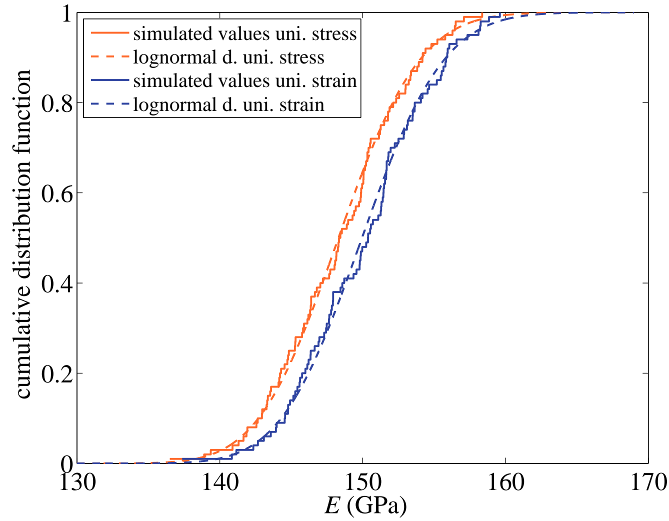

(a)

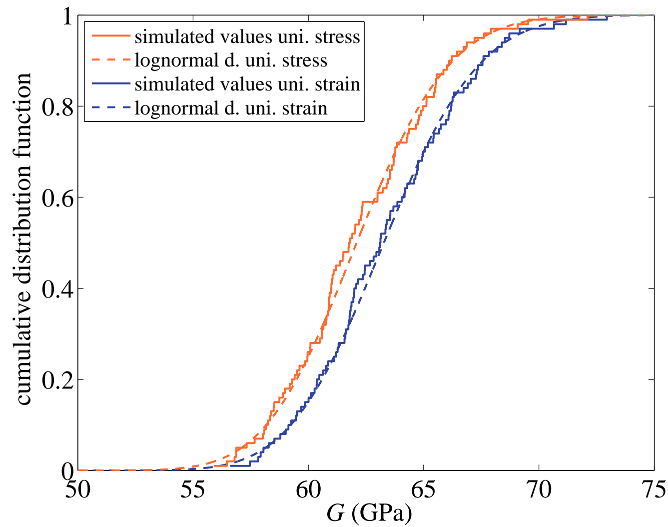

(b)

Figure 5.6: Fluctuations of the elastic properties of the SVE due to the polysilicon morphology: (**a**) Young's modulus E, and (**b**) shear modulus G. Blue lines correspond to the uniform strain BCs and orange lines correspond to the uniform stress BCs. Continuous lines show the CDFs of the MC FE simulations; dashed lines represent the lognormal distribution fits to the corresponding data.

Table 5.2: Estimated distribution for E and G via MC simulations of a 2×2 $(\mu\text{m})^2$ SVE.

	E (GPa)		G (GPa)	
	uniform strain	uniform stress	uniform strain	uniform stress
mean (GPa)	150.02	148.38	63.36	62.18
standard deviation (GPa)	4.51	4.46	3.26	3.17
μ_{LN}	5.01	5.00	4.15	4.13
σ_{LN}	0.030	0.301	0.051	0.051

Table 5.2 gathers the PDF parameters of Equation (5.1) for each set of BC and their statistics in terms of mean and standard deviation. As expected, uniform strain BC provides an upper bound on the elastic moduli with respect to uniform stress BC. The standard deviation is instead marginally affected by the type of BC employed in each set of simulations. The scattering of the estimates can be described looking at the standard deviations, which are about 3% and 5% of the mean values for Young's modulus and shear modulus, respectively. The mean values of the elastic moduli are varying less than 2%, depending on the type of BCs, implying that a relatively tight set of bounds is achieved. These PDFs (obtained via the preliminary MC) show the variations of the elastic properties due to the polysilicon morphology. Their effect on the scattering of the electromechanical response of the devices (i.e. $C-V$ curves) can be next obtained using the analytical model into another MC study (the main MC).

5.4.2 Convergence of Monte Carlo simulation

When the analytical model is used in the MC, material properties are drawn from the CDFs depicted in Figure 5.6, obtained through MC simulations of 2 μm $\times$ 2 μm SVEs previously carried out. The $C-V$ curves can then be calculated at very low computational cost. Therefore, the number of calculations can be conveniently increased till the convergence of the main MC using this model is reached and scattering of $C-V$ curves are reproduced.

As for the Monte Carlo simulations using the finite element models (MC FE), within each MC FE simulation, the polysilicon morphology (i.e. the grain boundary geometry and the in-plane crystalline orientation of each grain) is changed using a Voronoi tessellation (see Figure 4.4). Unlike the MC using the analytical

model, it is not convenient to increase the number of simulations excessively to ensure statistical convergence of MC FE; therefore, a convergence study is carried out. A number FE models is generated using different polysilicon morphologies and their $C-V$ curves are calculated. Since the output of the simulations is not a single scalar, we resort to a single actuation voltage and its response. Figure 5.7 reports the mean value of capacitance change at $V_{\rm ref} = 37$ V for the RR 20 μm beam length case versus the number of simulations up to 200. The voltage value is chosen as it is the smallest final actuation among the ten devices measured experimentally. Through this choice, we are choosing the largest signal-to-noise ratio in the recorded measurements. The specimens are not actuated up to the same maximum actuation voltage, as their pull-in voltages are different and we have avoided the possible systems failure due to the pull-in instability (see Chapter 3). A set of horizontal dashed lines are plotted in Figure 5.7, representing the $\pm 1\%$ of the difference between the maximum and minimum simulated capacitance change (within the 200 simulations), centered at the final mean value obtained after 200 simulations. As the number of simulations increases, the variations of the mean becomes smaller. Although it can be stated that the convergence has been obtained around 100 simulations, a cautious total number of 200 numerical simulations has been carried out for all MC studies in this work.

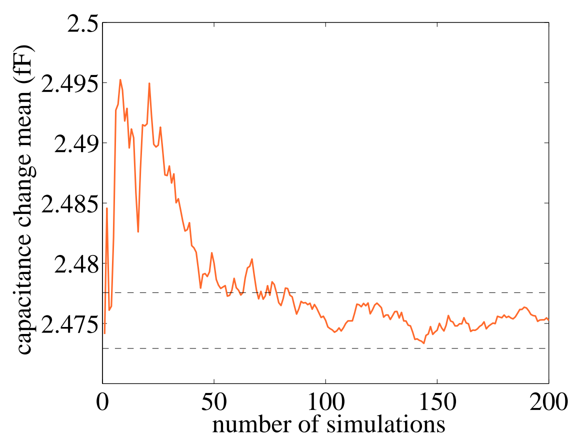

Figure 5.7: Dependence of the mean value of the capacitance change at $V_{\rm ref}$ on the number of simulations in the MC FE analysis.

5.4.3 Results

To account for the different number of results (i.e. capacitance change versus different actuation voltages) from numerics and experiments, the results of each approach are represented together by the CDF of the capacitance change at a given voltage value. To exemplify the procedure for the RR 20 μm-length case, in Figure 5.8 we consider, for simplicity, only MC FE and experimental results: the numerical and experimental $C-V$ curves would appear as depicted in Figure 5.8(a). We fix the maximum reference voltage V_{ref}, namely 37 V in this case, identified by the vertical continuous line in Figure 5.8(a); then, with respect to this value we calculate the corresponding capacitance change for each numerical or experimental curve (this step could be visualized as "moving along the vertical direction" between the curves along the aforementioned continuous line). Hence, a CDF for these data can be produced as a function of the change in capacitance; the unit value of the CDF corresponds, along the abscissae, to the maximum change in capacitance observed in the (either numerical or experimental) curves, while the lowest value of the CDF corresponds to the minimum change in capacitance. In Figure 5.8(b) the CDF for the ten experimental curves at the reference voltage 37 V is indicated by diamonds, while the CDF for the MC simulations is represented by a continuous curve (as we have 200 data points). The larger spread of the experimental results is therefore not only evident, but it can be also appreciated quantitatively.

It is possible to repeat the procedure in correspondence of other voltage values to follow the evolution of the CDFs: in this work we consider 25%, 50%, 75% of the reference voltage V_{ref}, as indicated in Figure 5.8(a) via the vertical dashed lines.

In the following Figures 5.9-5.12 and 5.13-5.16 the four configurations (RR, RL, LR, LL) are investigated for the two devices whose beam length is 20 μm and 10 μm, respectively. Given the maximum reference voltage, in each figure the CDFs for the analytical (dashed lines), MC FE model (continuous line), and experimental results (diamonds) are presented. Two CDFs are actually shown for the analytical model, according to the type of BCs adopted for the SVE used to determine the effective material properties: in blue uniform strain imposed BCs,

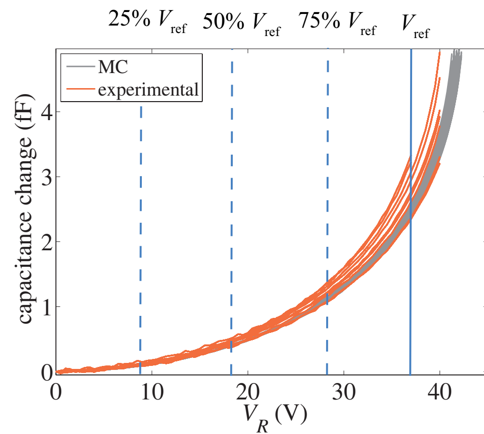

(a)

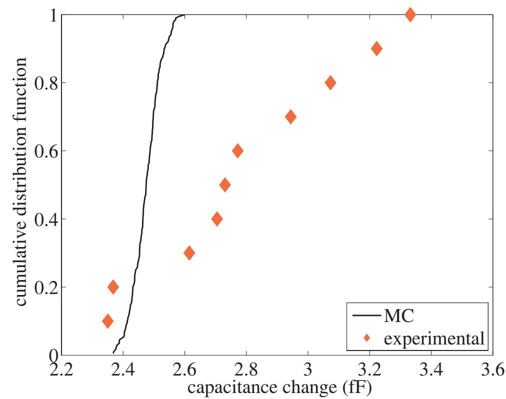

(b)

Figure 5.8: MC FE method versus experimental results for rotational actuation and sensing through V_R: (**a**) electromechanical response at varying voltage, and (**b**) capacitance change for V_R=37 V; continuous line corresponds the MC FE method; diamond symbols stand for experimental responses.

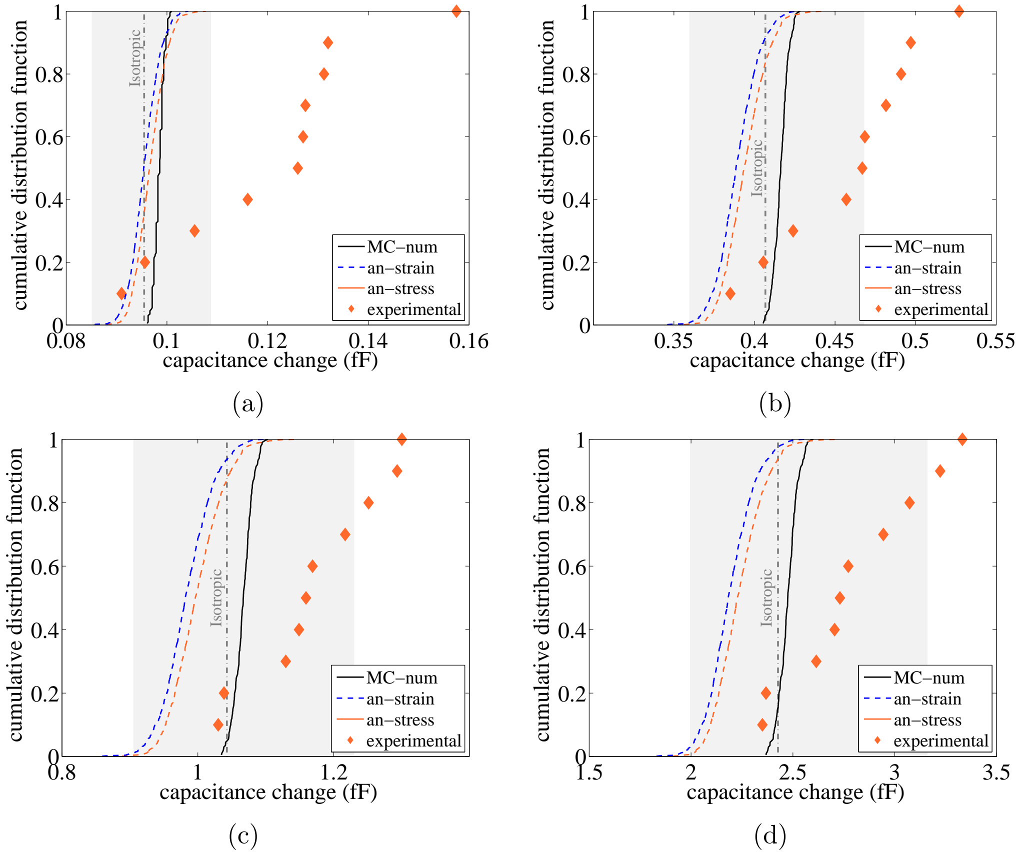

Figure 5.9: Comparisons between analytical, numerical and experimental results for the device featuring the 20 μm-length beam in the RR configuration. (**a**) 25%, (**b**) 50%, (**c**) 75%, (**d**) 100% of the reference maximum voltage $V_{\text{ref}} = 37$ V.

in orange uniform stress imposed BCs are represented. The grey shaded area in the graphs and the dotted line show the stiff/compliant case bounds and the isotropic case (mentioned in Section 5.3) at the specific input voltage, respectively (see Figures 5.1–5.4).

As already observed, the bounds computed by considering the maximum and the minimum in-plane effective Young's modulus (and corresponding values of Poisson ratio) of the polysilicon can cover most of the measured data, but the MC results yield a detailed observation on the actual polysilicon morphology effect. By looking first at the comparison between analytical and MC FE model

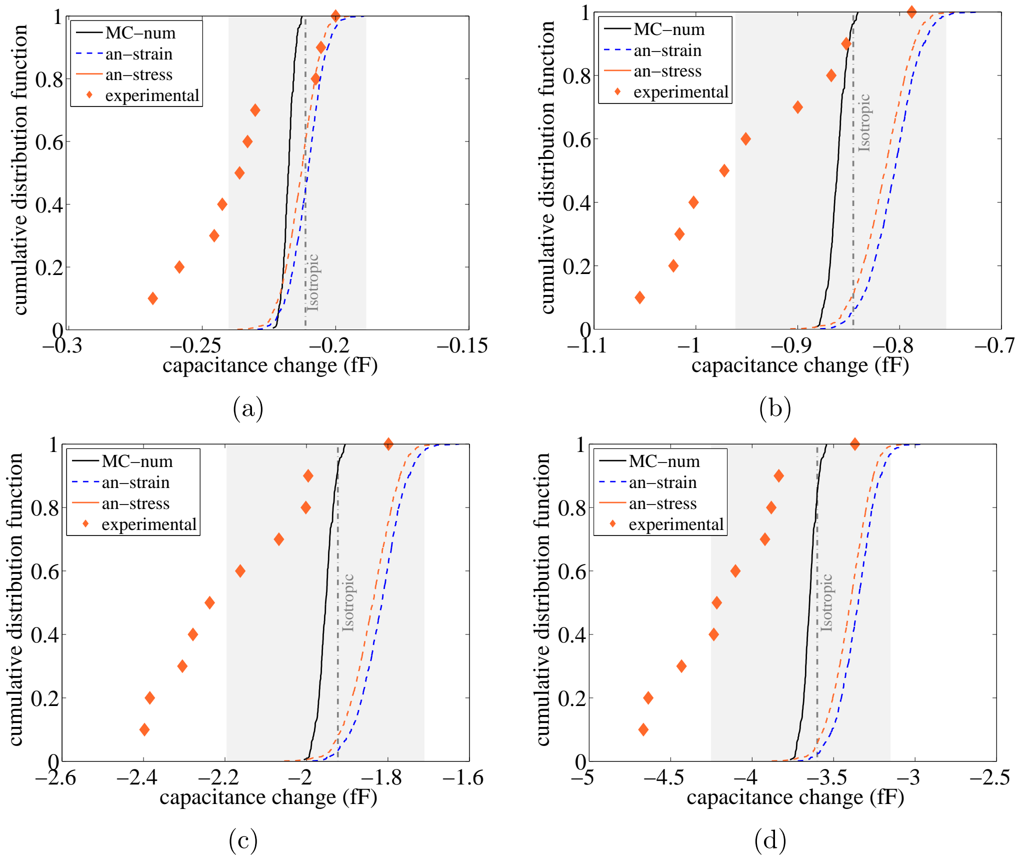

Figure 5.10: Comparisons between analytical, numerical and experimental results for the device featuring the 20 μm-length beam in the RL configuration. (**a**) 25%, (**b**) 50%, (**c**) 75%, (**d**) 100% of the reference maximum voltage $V_{\text{ref}} = 37$ V.

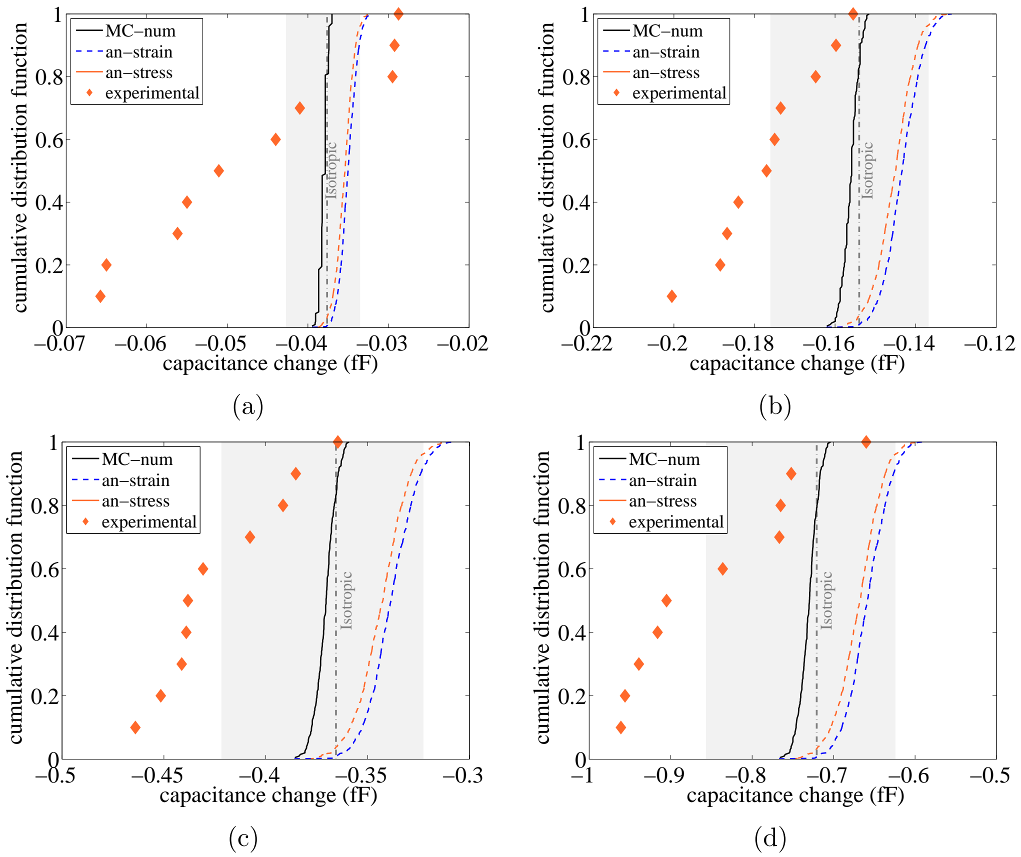

Figure 5.11: Comparisons between analytical, numerical and experimental results for the device featuring the 20 μm-length beam in the LR configuration. (**a**) 25%, (**b**) 50%, (**c**) 75%, (**d**) 100% of the reference maximum voltage $V_{\text{ref}} = 15.5$ V.

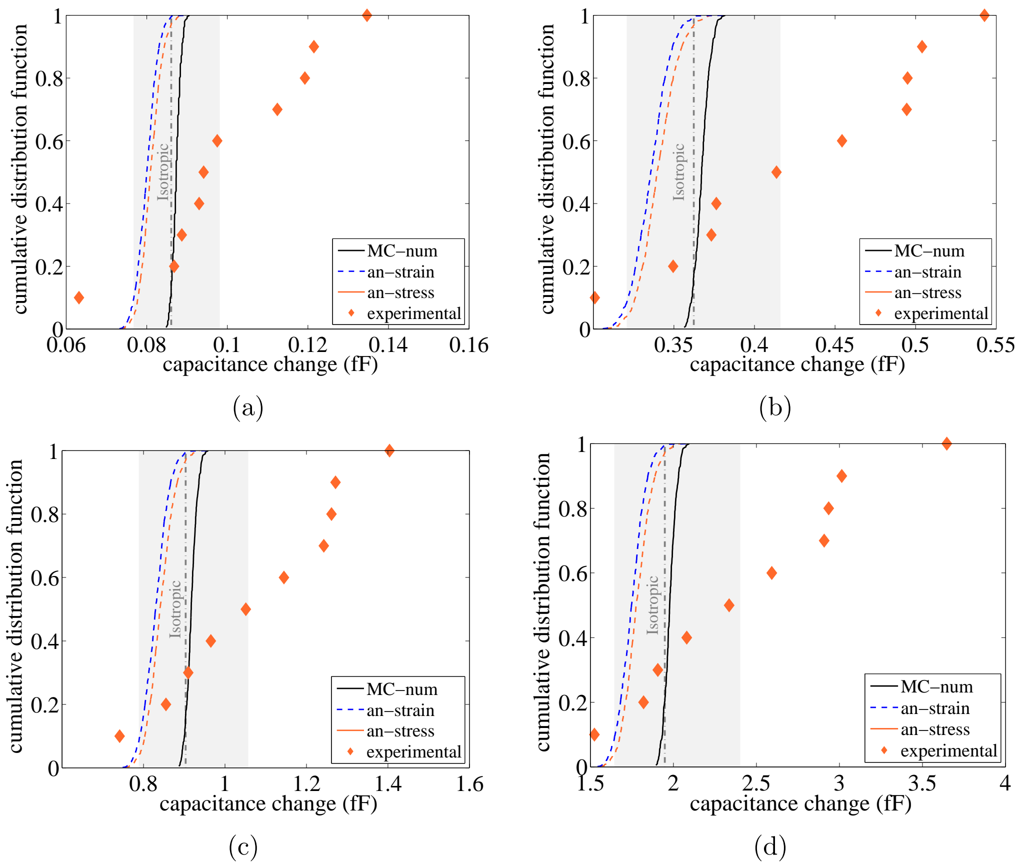

Figure 5.12: Comparisons between analytical, numerical and experimental results for the device featuring the 20 μm-length beam in the LL configuration. (**a**) 25%, (**b**) 50%, (**c**) 75%, (**d**) 100% of the reference maximum voltage $V_{\mathrm{ref}} = 15.5$ V.

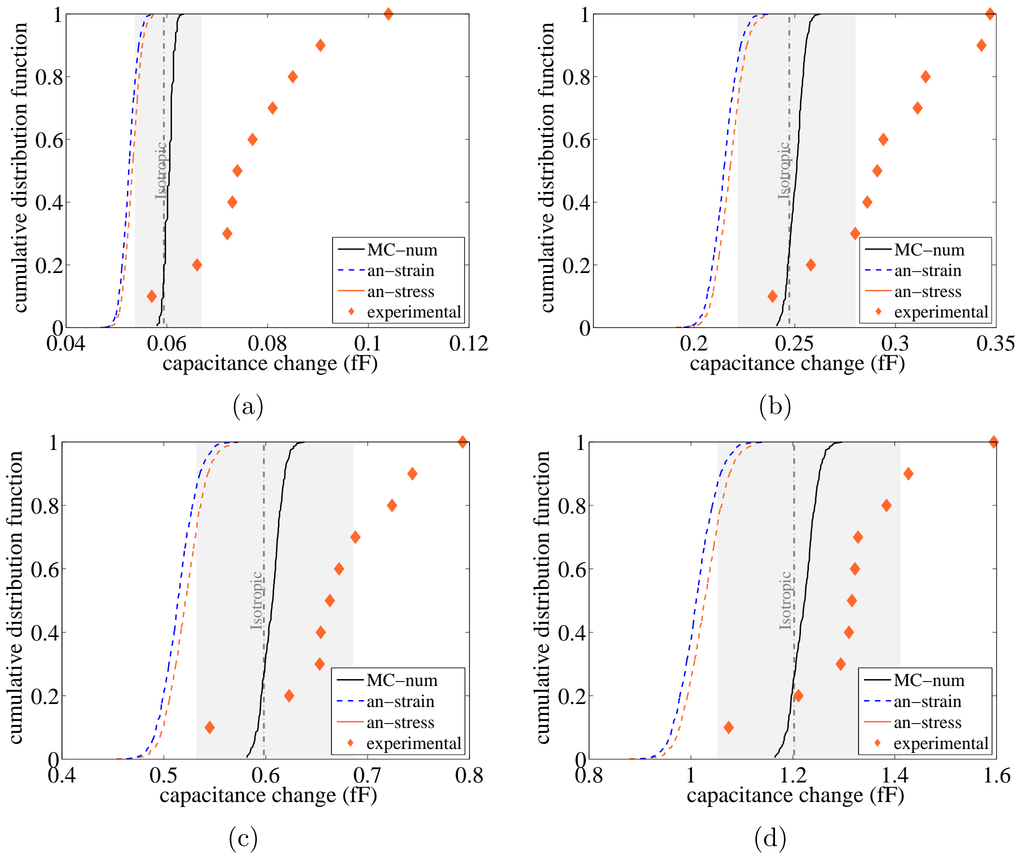

Figure 5.13: Comparisons between analytical, numerical and experimental results for the device featuring the 10 μm-length beam in the RR configuration. (**a**) 25%, (**b**) 50%, (**c**) 75%, (**d**) 100% of the reference maximum voltage $V_{\text{ref}} = 40$ V.

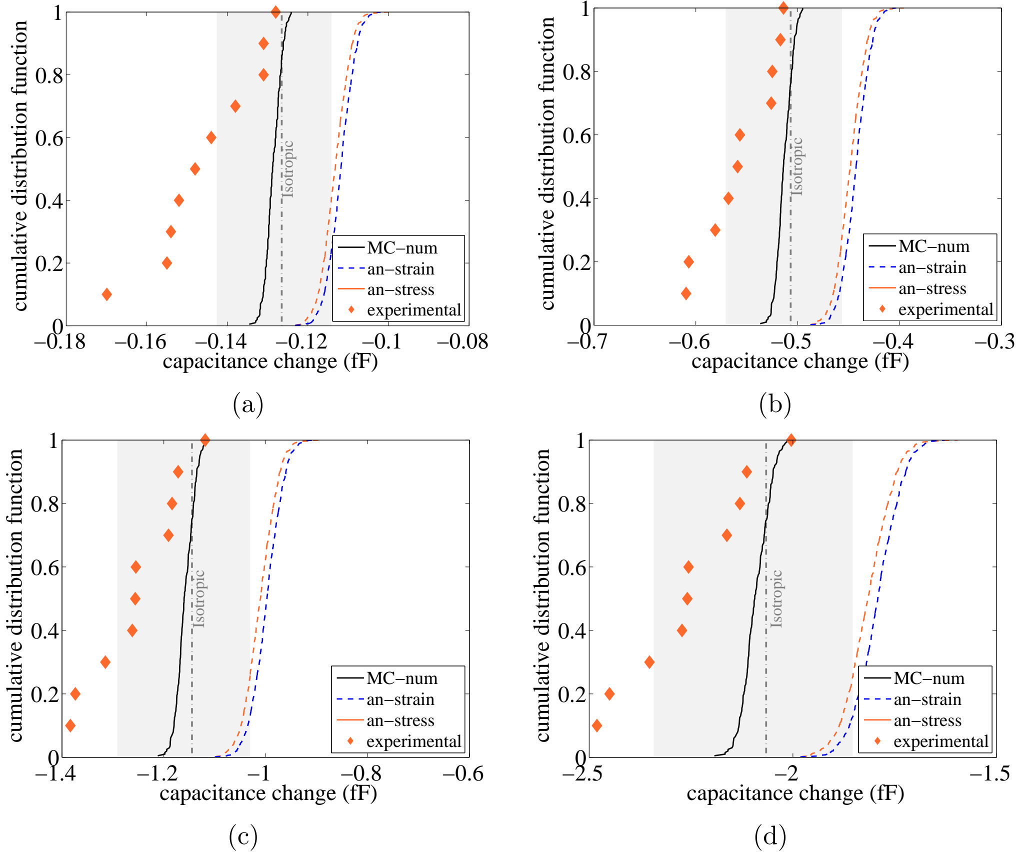

Figure 5.14: Comparisons between analytical, numerical and experimental results for the device featuring the 10 μm-length beam in the RL configuration. (**a**) 25%, (**b**) 50%, (**c**) 75%, (**d**) 100% of the reference maximum voltage $V_{\text{ref}} = 40$ V.

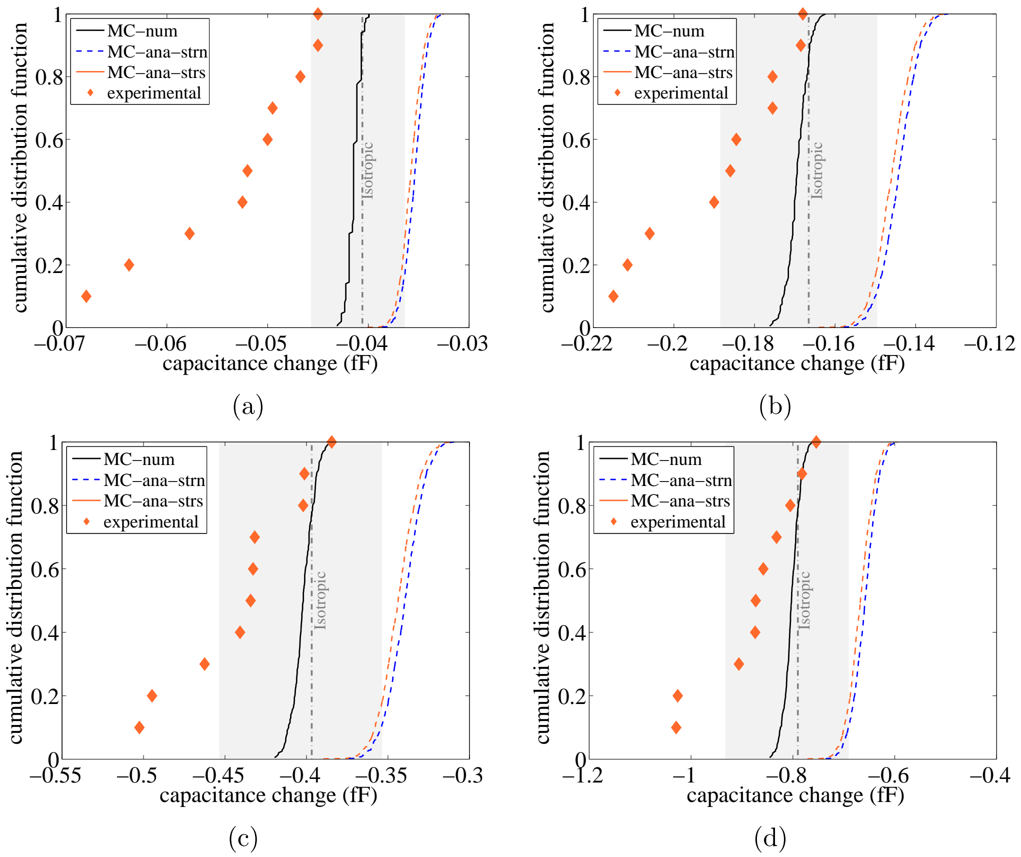

Figure 5.15: Comparisons between analytical, numerical and experimental results for the device featuring the 10 μm-length beam in the LR configuration. (**a**) 25%, (**b**) 50%, (**c**) 75%, (**d**) 100% of the reference maximum voltage $V_{\text{ref}} = 22.5$ V.

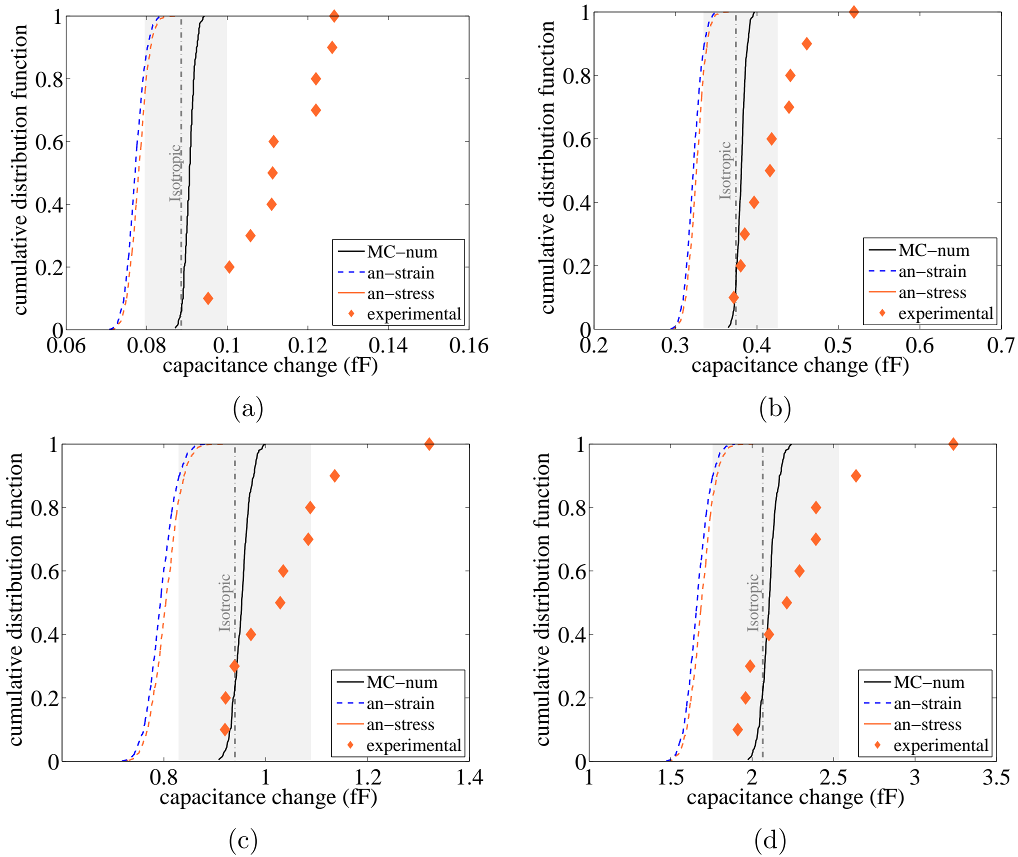

Figure 5.16: Comparisons between analytical, numerical and experimental results for the device featuring the 10 μm-length beam in the LL configuration. (**a**) 25%, (**b**) 50%, (**c**) 75%, (**d**) 100% of the reference maximum voltage $V_{\text{ref}} = 22.5$ V.

CDFs, it can be observed that the distance between the CDFs rises as the voltage increases in all the cases. Moreover, the MC FE model CDF corresponds always to larger changes in capacitance (in absolute term) with respect to the ones obtained by the analytical approach: in other words, lower capacitance change at the same actuation is due to the lower displacements of the rotor which is linked to the rigidity of the micro beam. From the mechanical point of view, the analytical response is therefore stiffer than the purely numerical MC response. This difference can be mainly linked to two points. First, the assumption of perfect anchor at the analytical modelling while in the numerical model the elastic field at the anchor is taken into account. Second, the geometric nonlinearities in the electrical field between the conductors are handled better in the numerical model, see Chapter 4.

The MC FE model yields a steeper CDF, i.e. the fluctuation of the change in capacitance value is limited in comparison with the analytical cases; again, the analytical CDFs tend to become less steep (and therefore the change in capacitance values are more spread out) as the voltage increases, see e.g. Figure 5.9. This difference in slope of the curves is lower in the beam length l =10 μm case; this implies that the statistics of mechanical properties in Figure 5.6 is more appropriate for the shorter beam. This outcome was expected, since the number of grains in the l =10 μm beam is lower than in the l =20 μm case; therefore, a 2 μm $\times$ 2 μm SVE is more appropriate for the former (recalling that the beam width is 2 μm). Only a small increase of the distance between analytical and MC FE model CDFs can be detected by moving from beam length l=20 μm to l=10 μm. The stiffest response corresponds always to the analytical case with imposed displacement BCs to the SVE; however, for all the considered configurations and beam lengths, the difference with imposed force BCs is small.

The most interesting observations can be drawn from the comparison with the experimental data. In all the cases, the most relevant issue is that they appear rather spread out with respect to the analytical and MC FE results; moreover, the experimental points mostly represent more compliant responses with respect to the MC approach (and therefore also with respect to the analytical approaches). While the number of experiments is limited to ten, this trend is very clear and it manifests itself from the beginning, at 25% V_{ref}, and does not seem to follow a

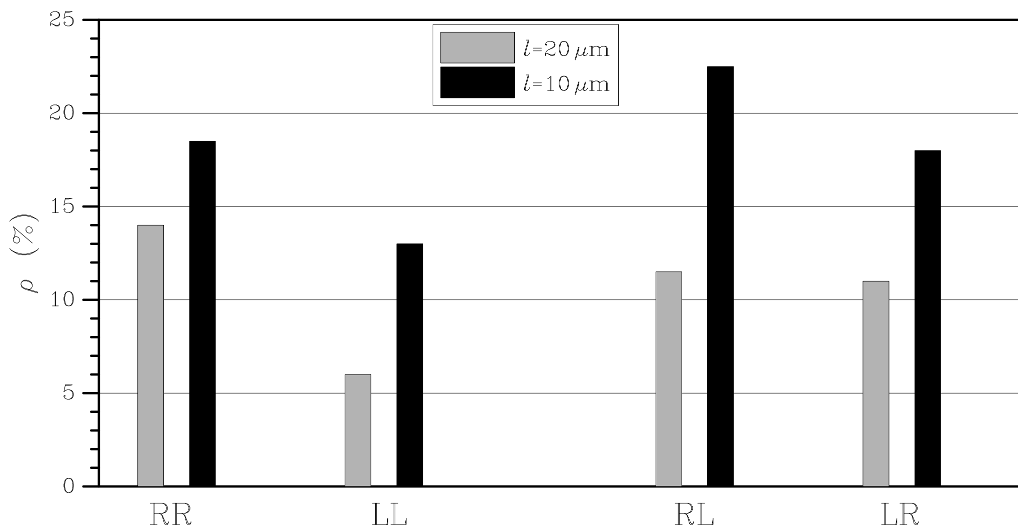

Figure 5.17: Ratio between standard deviations of MC FE model and that of the measured data for the different experimental configurations.

clear pattern when the voltage increases.

In Figure 5.17, the ratio ρ between the standard deviation of MC FE results and that of the measured data at the maximum reference voltage V_{ref} for each configuration, is represented. Since the latter standard deviation is larger, the ratio is always lower than one and ρ is represented as a percentage. It is very clear that the spread within the MC FE model results and the experimental data increases as the length decreases in the considered range. But this increase is greater for MC FE results with respect to the experimental ones.

One of the most reasonable possibilities to explain this difference in the results spreading consists into admitting a different beam geometry for the actual devices (obtained from the same silicon wafer) with respect to the nominal (designed) geometry. In particular, even small changes in the beam width (nominally set equal to h=2 μm) largely influence the second moment of area $I = wh^3/12$ in Eq. (4.11), and they also modify the transversal cross section A_s. For instance, it is well known that the production process partially remove the original polysilicon pattern during the deep reactive-ion etching, and the variability in this so-called over-etch can be on the order of 0.1÷0.2 μm per side (typically the *total* over-

etch range is set between 0.2÷0.4 μm) [Gad-el Hak, 2001, Hong et al., 2000, Alper et al., 2008]. The over-etch value is generally assumed to be constant for the single MEMS and often also for devices placed on the same silicon wafer; however, the measurements for this MEMS could be even influenced by a variation in the order of 50 nm in the over-etch (which implies 15% change in the second moment of area of the beam with width nominally equal 2 μm), impacting not only on the beam stiffness but also on the initial gap (hence modifying the electromechanical force). Other geometric effects could influence the results, such as initial position offset of the beam or imperfections at the anchor (see Section 3.5) or the lack of symmetry at the rounded corners[1] that modify the hypotheses assumed so far for the boundary conditions.

5.5 Concluding remarks

In this chapter, the effects of variation of the specimen mechanical properties on the electromechanical response of the test device have been studied. First, by defining an isotropic case for polysilicon elastic properties, a nominal response has been derived. Then, bounds on the $C - V$ curves have been established by adopting the admissible elastic properties of silicon. It has been observed that most of measured data are located within the bounds. In the next step, two sets of Monte Carlo simulations have investigated the scattering of $C-V$ curves due to the variations of polysilicon morphology at the specimen. Comparing the results of Monte Carlo simulations and experimental measurements, it has been shown that i) the uncertainties due to the mechanical properties variations intensify for shorter beams and, ii) the uncertainty sources related to fabrication inaccuracies must be present in the experiments.

In the next chapter, we take into account two sources of uncertainty in the analytical model and quantify them based on the recorded data for each single specimen.

[1] The corners at which the beam is connected to either rotor or the anchor, feature a rounded (or fillet) shape due to imperfect fabrication, see Figure 3.2.

6

On-line parameter estimation: particle filter

6.1 Introduction

In the previous chapter, we have observed that the experimental scatterings can not be solely related to the mechanical properties variations and the geometric inaccuracies must be also allowed for. The analytical model provided in Chapter 4 is purely deterministic. To infer the possible variability of the model parameters based on the experimental data, particle filtering [Djuric et al., 2003, Doucet et al., 2000] is here adopted.

The effect of variability of the overall Young's modulus of the polysilicon film on the $C-V$ plot is ultimately linked to the flexural rigidity of the tested beam. In addition to that, we have shown in the previous chapter that we need to allow for other sources uncertainties. Based on the discussion in Section 3.5, the next parameter to be considered aside the Young's modulus can be the over-etch. Unlike the Young's modulus, a variation of the over-etch has several consequences. Firstly, it affects the stiffness of the beam due to the changes of the beam thickness and therefore the second moment of area. Secondly, it varies the actuation terms F and M and also the measured capacitances. These terms are linked to the electrical field formed within the conductors; therefore, changing initial gap g_0 between conductors has a direct effect on their values.

Discriminating the two different sources is not easy, due to the coupled elec-

tromechanical response of the system. By monitoring the input-output relation at increasing applied voltage, and by simultaneously handling both the sensing strategies reported before in an on-line fashion, an estimation of the two stochastic terms is here looked for. The on-line parameter estimation algorithms update the estimates of the parameters of a model every time new data is available during the parameter estimation operation. On the contrary, in off-line estimation, all the input/output data via experiments are first collected and the model parameters are then estimated. Parameter values estimated using on-line estimation can vary with time, but parameters estimated using off-line estimation do not.

In this chapter, we adopt a particle filter which belongs to the family of recursive Bayesian inference[1] methods, and estimate the two uncertain parameters for each specimen. It will be seen that the method is stable at parameter inference process. However, the assumed sources of uncertainties are still not enough to describe the experimental measurements. In Section 6.2, we review the basics of recursive Bayesian inference approach which particle filtering belongs to. Section 6.3 highlights the key features of the adopted particle filter. A thorough discussion on the relevant results remarking the important findings is finally deployed in Section 6.4.

6.2 Recursive Bayesian inference

When measurements may be affected by noise and disturbances, the unknown parameters of the model can be obtained more appropriately in a statistical approach: each parameter is treated as a random variable extracted from a statistical probability distribution rather than a single value (also known as crisp parameter). The process of deducing the properties of these distributions is generally referred to statistical inference. The methods for the interpretation of the probabilities are broadly divided in two groups: frequentist inference and Bayesian inference [Congdon, 2014]. The former defines the probability as the limit of frequency of the event's occurrence in a large number of well defined and random experiments. This definition of probability narrows down its applicability since

[1] Bayesian inference is a statistical method in which the Bayes' rule is used to update the probability estimate for a hypothesis as additional information is available.

probability can only be assigned to an event whose random experiment is available [Yuen, 2010]. Bayesian inference instead states the probability as a representation of an individual's degree of belief in a statement. Bayesian inference is advantageous over frequentist inference in the handling of the present problem because it allows *a priori* information or results of the previous inference to enrich the current estimate. Since the Bayesian inference includes different approaches and interpretations, only a practical summary of Bayesian inference is here perused. A more detailed and classical introduction can be found in [Robert, 2007].

A recursive inference of the hidden system quantities in the Bayesian framework is generally possible when i) *a priori* information about the observable quantities probability is available, and ii) a correlation exists between observable and hidden quantities. The Bayes' rule is then exploited to deduce the probability distribution of the hidden state variables [Eftekhar Azam and Mariani, 2012].

Returning to the test devices, the analytical model is preferred over the numerical model; this choice is backed by the large number of simulations needed in recursive Bayesian inference methods (e.g. particle filter) and relatively large computational demand of the numerical model. The relation between the sought parameters (i.e. over-etch and Young's modulus) and the measurement is mathematically expressed via a state-space model. As for the parameters, since they are structure-dependent, they should not vary during the measurement of capacitance change at varying loading; anyhow, to allow for model errors induced by the simplified analytical model of Chapter 4 and to update the estimates from presumably wrong initial guesses, a fictitious random walk model[1] is assumed to govern their evolution. If parameters are then collected in a state vector $\mathbf{x}$, its evolution within the interval $[t_{k-1}\ t_k]$ representing the (time) window between two successive measurements at increasing actuation voltage (i.e. two successive actuations), reads:

$$\mathbf{x}_k = \mathbf{x}_{k-1} + \mathbf{v}^{\mathbf{x}_k} \tag{6.1}$$

where $\mathbf{v}_k^{\mathbf{x}} \sim \mathbb{N}(\mathbf{0}, \mathbf{Q}^{v^x})$ denotes a zero mean, white Gaussian noise whose covari-

[1] Random walk is a stochastic process which describes a path of successive random steps on a mathematical space and its step size can vary according to specific distribution, e.g. normal distribution.

ance must be appropriately adjusted to be in the feasible range of the parameters and so to attain accurate estimates [Eftekhar Azam et al., 2012]. This term shows the degree of the accuracy of the model for representing the real observed problem. In case of dealing with a pseudo-experimental problem, this adjustment would not be necessary and very small entries of covariance is suitable to allow for deterministic-like nature of the system evolution equations [Eftekhar Azam, 2014]. The observation equation is derived from the physical model of Chapter 4, and it is formally written as:

$$\mathbf{y}_k = \mathbf{h}_k(\mathbf{x}_k) + \mathbf{w}_k \tag{6.2}$$

where: $\mathbf{y}_k$ denotes the capacitance measurements at time t_k; $\mathbf{h}_k(.)$ stands for the nonlinear relationship between the parameters in $\mathbf{x}_k$ and the measurements $\mathbf{y}_k$; $\mathbf{w}_k \sim \mathbb{N}(\mathbf{0}, \mathbf{Q}^{\mathbf{w}})$ is the measurement noise, again Gaussian with zero mean and covariance $\mathbf{Q}^{\mathbf{w}}$. Generally, the noise can nonlinearly affect the system observation. But in the present problem, it is linked to the errors stemming from measurement equipments and not related to level of actuation; therefore, it can be simply added to the observation equation.

The inference problem can be regarded as the recursive estimation of the expected value $\mathbb{E}[\mathbf{x}_k|\mathbf{y}_{1:k}]$ and/or other statistics of the state vector, conditioned on the observation of the system. In other words, $\mathbb{E}[\mathbf{x}_k|\mathbf{y}_{1:k}]$ in the recursive framework is the expected values for the unknown parameters of the model (e.g. Over-etch and Young's modulus) after observing the system's response (which is experimentally measured) up to an actuation voltage corresponding to time t_k. Provided that the initial probability density function (PDF) of the process $p(\mathbf{x}_0|\mathbf{y}_0) = p(\mathbf{x}_0)$ is known, the goal is to estimate $p(\mathbf{x}_k|\mathbf{y}_{1:k})$ upon availability of the conditional PDF $p(\mathbf{x}_{k-1}|\mathbf{y}_{1:k-1})$. The problem is often formulated in two distinct stages of prediction and update: in the prediction stage, the Chapman-Kolmogorov integral yields *a prior* of the state PDF at t_k [Arulampalam et al., 2002]:

$$p(\mathbf{x}_k|\mathbf{y}_{1:k-1}) = \int p(\mathbf{x}_k|\mathbf{x}_{k-1}) p(\mathbf{x}_{k-1}|\mathbf{y}_{1:k-1}) d\mathbf{x}_{k-1} \tag{6.3}$$

while in the update stage, as soon as the latest observation $\mathbf{y}_k$ becomes available,

Bayes' rule allows to correct the PDF through:

$$p(\mathbf{x}_k|\mathbf{y}_{1:k}) = \varsigma p(\mathbf{y}_k|\mathbf{x}_k)p(\mathbf{x}_k|\mathbf{y}_{1:k-1}) \tag{6.4}$$

where ς is a normalizing constant, which depends on the likelihood function of the observation process.

The recurrence of Eq. (6.3) and Eq. (6.4) together forms the exact basis for recursive Bayesian inference; the *a prior* PDF of the unknown parameters (i.e. the initial guess on PDF or the result of Eq. (6.3)) can be updated by observing the system response. With exception of few cases, like linear Gaussian state space models (Kalman filter) and hidden finite-state space Markov chains (Wohnam filter), it is not possible to furnish analytical solution of the integral in Eq. (6.3), since they require the evaluation of complex integrals [Cadini et al., 2009]. In the next section, an approximation method for this problem is given.

6.3 Particle filtering

To deal with general nonlinear/non-Gaussian problems, sequential Monte Carlo methods [Doucet and Johansen, 2009] can be resorted for evaluating the Chapman-Kolmogorov integral. Sequential Monte Carlo methods do not impose any restriction on the posterior density $p(\mathbf{x}_k|\mathbf{y}_k)$, and approximate the integrals in Eq. (6.3) through finite sums, adopting a sequential importance sampling. To this end, the posterior PDF is represented via Dirac delta functions at a set of discrete sample points which can be called also particles. Without loss of generality, the posterior probability of the parameters collected in $\mathbf{x}_k$ given the measurement vector $\mathbf{y}_k$ can then be written as [Capellari et al., 2015, Cadini et al., 2009]:

$$p(\mathbf{x}_k|\mathbf{y}_k) = \int p(\boldsymbol{\varepsilon}_k|\mathbf{y}_k)\delta(\boldsymbol{\varepsilon}_k - \mathbf{x}_k)d\boldsymbol{\varepsilon}_k \tag{6.5}$$

where $\delta(.)$ denotes the Dirac delta function. Assuming that the true posterior $p(\mathbf{x}_k|\mathbf{y}_k)$ is known and can be sampled, an approximate estimate for the posterior distribution of the parameters can be given by:

$$p(\mathbf{x}_k|\mathbf{y}_k) \approx \frac{1}{N_s}\sum_{i=1}^{N_s}\delta(\mathbf{x}_k - \mathbf{x}_k^i) \tag{6.6}$$

where $\mathbf{x}_k^i$ is a set of N_s random samples drawn from the true posterior PDF $p(\mathbf{x}_k|\mathbf{y}_k)$. However, it is impossible to efficiently extract these samples, as the goal of the procedure is the definition of the true posterior PDF. Importance sampling has been introduced as a remedy to this deadlock: an arbitrarily chosen distribution $\pi(\mathbf{x}_k|\mathbf{y}_k)$, called importance function, is sampled in the absence of the true *a posteriori* PDF. An unbiased estimate of $p(\mathbf{x}_k|\mathbf{y}_k)$ can then be obtained as:

$$p(\mathbf{x}_k|\mathbf{y}_k) \approx \sum_{i=1}^{N_s}\tilde{\omega}_k^i\delta(\mathbf{x}_k - \mathbf{x}_k^i) \tag{6.7}$$

where $\tilde{\omega}_k^i = \omega_k^i/\sum_{j=1}^{N_s}\omega_k^j$ and the so-called importance weights ω_k^i are approximated through:

$$\omega_k^i = \frac{p(\mathbf{y}_k|\mathbf{x}_k^i)p(\mathbf{x}_k^i)}{\pi(\mathbf{x}_k^i|\mathbf{y}_k)} \tag{6.8}$$

where $p(\mathbf{y}_k|\mathbf{x}_k^i)$ is the *likelihood* of the observation. The importance weights can be updated through:

$$\omega_k^i = \omega_{k-1}^i\frac{p(\mathbf{y}_k|\mathbf{x}_k^i)p(\mathbf{x}_k^i|\mathbf{x}_{k-1}^i)}{\pi(\mathbf{x}_k^i|\mathbf{x}_{k-1}^i, \mathbf{y}_{1:k})} \tag{6.9}$$

This recursive formula provides a way to sequentially update the importance weights, given an appropriate choice of the proposal distribution $\pi(\mathbf{x}_k^i|\mathbf{x}_{k-1}^i, \mathbf{y}_{1:k})$. Consequently, any expectations of the form $\mathbb{E}[g(\mathbf{x}_k)] = \int g(\mathbf{x}_k)p(\mathbf{x}_k|\mathbf{y}_k)\,\mathrm{d}\mathbf{x}_k$ while $g(.)$ is any given function, can be approximated by $\mathbb{E}[g(\mathbf{x}_k)] \approx \sum_{j=1}^{N_s}\omega_k^j g(\mathbf{x}_k^j)$. In [Doucet, 1997], it was shown that the transition prior distribution $p(\mathbf{x}_j|\mathbf{x}_{j-1})$ is the most popular choice for the proposal distribution instead of $\pi(\mathbf{x}_k^i|\mathbf{x}_{k-1}^i, \mathbf{y}_{1:k})$. Having that, the importance weights are easily updated by simply evaluating the observation likelihood density $\pi(\mathbf{x}_k|\mathbf{x}_{k-1})$ for the sampled particle set, through [Cadini et al., 2009]:

$$\omega_k^i = \omega_{k-1}^i p(\mathbf{y}_k|\mathbf{x}_k^i) \tag{6.10}$$

Algorithmic issues may arise as the covariance of the weights always increases

over time [Doucet et al., 2000]. In practice, after a few iterations all the particles but one display negligible weights; this issue is referred to as sample degeneracy [Doucet and Johansen, 2009]. To alleviate sample degeneracy, particle filters are typically complemented with a sequential importance sampling and resampling stage, see e.g. [Liu et al., 2001]. During the resampling stage, particles with relatively low probability are deleted and the ones with higher likelihood are duplicated. An intuitive explanation of this stage is that each $\mathbf{x}_k^i$ might be a solution for the parameter estimation problem while its associated weight ω_k^i expresses the probability of this solution to be the correct one. The resampling tends to duplicate the particles with higher probability (weight) and discard the ones with lower probability (weight); therefore, the resampling stage guides the particles around the high probability peak/s. Several procedures have been proposed in the literature for resampling, such as: multinomial resampling; stratified resampling; residual resampling; and systematic resampling. For implementation and algorithmic details, readers are referred to [Douc et al., 2005].

Using extensive Monte Carlo simulations, it was shown in [Hol et al., 2006] that, in terms of resampling quality and computational complexity, systematic resampling is favorable; therefore, in this study the latter resampling scheme is adopted. Resampling may however cause another issue called sample impoverishment, when few particles with a notable weight are kept while all others with a negligible weight are abandoned [Li et al., 2012]. In general terms, it can be said that sample degeneracy is a result of samples being too much distributed (also in zones with very low probability), instead sample impoverishment is (as a possible direct negative consequence of resampling) the problem of having the particles too focused. Sample degeneracy and sample impoverishment are arguably two main drastic flaws associated with particle filters and importance sampling, which together provide unsatisfactory particle distributions [Li et al., 2014]. One of the first remedies for mitigating the impoverishment issue was roughening (also called jittering [Flury and Shephard, 2009], diffusing [Pantrigo et al.,] or diversifying [Vadakkepat and Jing, 2006]), which basically adds an independent Gaussian jittering noise with zero mean and constant covariance to the resampled particles. All these issues motivated the research on the so-called particle distribution optimization schemes, such as applications of artificial intelligence methods (e.g.

particle swarm optimization and genetic algorithms) and machine learning approaches (e.g. clustering and merging); for a recent review of the state-of-the-art for the subject, see [Li et al., 2014]. For the current application, it will be seen in the following that, due to the relatively low number of iterations (i.e. recorded voltage actuations, every 0.5 V), sample impoverishment does not prevail and only a resampling stage has been implemented.

The particle filter samples the actual PDF of the unknown parameters by drawing samples in prediction stage so it can appropriately account for non-Gaussian densities. It is an on-line strategy as it does not handle all the experimental information already available and but instead deploy them step by step starting from zero actuation voltage up to the highest available.

6.4 Parameter estimation: Results

In this section, we first explore the sensitivity of the device response to the two parameters to be identified, namely the over-etch O and the Young's modulus E of the film. Next, the particle filter described earlier is adopted to estimate the parameter values for each of ten samples. As for the target values $\bar{O}$ and $\bar{E}$ of parameters, we have assumed: $\bar{O} = 0$, which means that the real geometry of the device matches the design one; $\bar{E} = 149.3$ GPa, which is the average between the two (upper and lower) bounding estimates of the homogenized polysilicon Young's modulus, see [Mariani et al., 2011].

Both O and E affect the stiffness terms in Eq. (4.6) or Eq. (4.14). Specifically, the over-etch comes into play by changing the width of the beam according to $h^* = \bar{h} - 2O$; further to that, the over-etch also has a role in actuation and sensing, since the gap is affected according to $g_0^* = \bar{g}_0 + 2O$. In these equations, the starred values represent the actual geometric features of each sample, while the over-barred ones are the target values (reported in Table 3.1).

For some test structures, see e.g. [Rocha et al., 2008, Mol et al., 2008, Rocha et al., 2011], the pull-in voltage V^{pull} has been suggested as a possible feature of the overall structural response providing insights into micromechanical details of the device, on top of all the over-etch. Figure 6.1 gathers the values of the voltage corresponding to the pull-in instability in case of either lateral or rotational

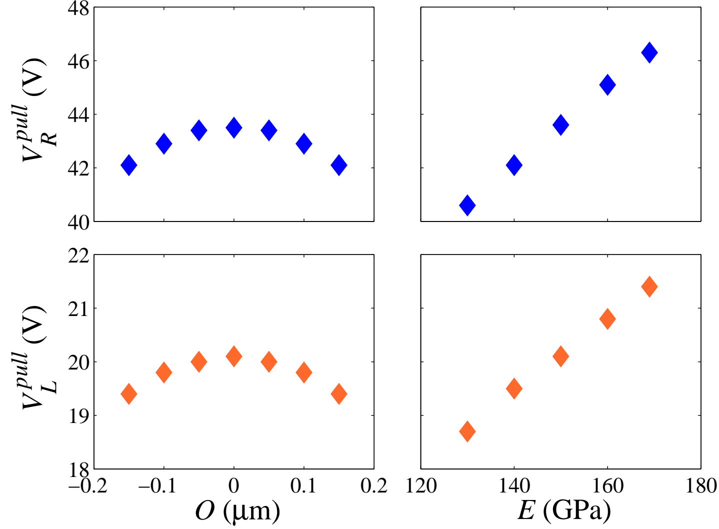

Figure 6.1: Sensitivity of the pull-in voltages V_R^{pull} and V_L^{pull} to a variation of (left) over-etch O, or (right) polysilicon Young's modulus E.

actuation. The sensitivity to O and R is numerically assessed by fixing one of the two parameters at the relevant target value (either $\bar{O}$ or $\bar{E}$), and changing the other within the domain $O \in [O_{min}$=-0.15 μm, O_{max}=0.15 μm] based on the specifications of the fabrication process or $E \in [E_{min}$=130 GPa, E_{max}=169 GPa] based on the admissible values of Young's modulus for silicon plane (100). It can be noted once again that the lateral actuation is associated to lower pull-in voltages; such effect has been also observed in the experimentally measured values, see Figures 3.7 and 3.8. A variation of the Young's modulus is shown to affect the pull-in voltage almost linearly, while the over-etch has a nonlinear impact. This observation is essential if one aims to characterize the device by using the pull-in voltage only, since that would require a one-to-one relation between the varying parameter and V^{pull} [Mol et al., 2008]. This issue is further illustrated in Figure 6.2: the overall response of the system for two different values of O leads to very similar values of the pull-in voltage. As it can be seen, although the same asymptotic response occurs at pull-in instability, the devices feature a much different capacitance variation in the stable regime. Therefore, the whole response of the system has to be accounted for to correctly characterize the uncertainties.

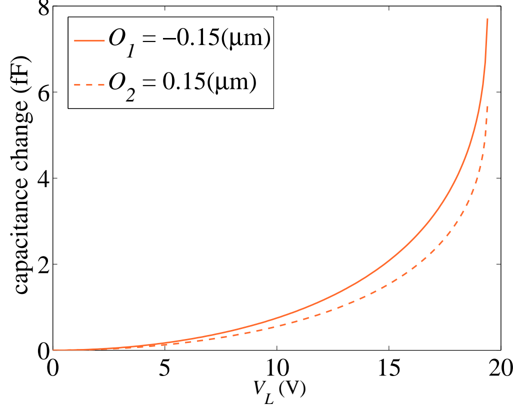

Figure 6.2: Comparison between the electromechanical responses of two devices respectively featuring $O_1 = -0.15$ μm (solid line) and $O_2 = 0.15$ μm (dashed line), with $E_1 = E_2 = \bar{E}$.

In the filtering procedure, the Young's modulus and the over-etch are allowed to vary in the domains mentioned earlier. The extreme values for the Young's modulus have been selected according to the range of variation of E for single-crystalline silicon, see [Hopcroft et al., 2010]; the values for the over-etch have been instead assumed on the basis of fabrication process specifications.

Since the adopted Bayesian filtering procedure needs to be initialized with a guess for the handled parameters, coefficients ξ_O and ξ_E are introduced to allow such initialization values O_i and E_i to vary around the target ones $\bar{O}$ and $\bar{E}$ according to:

$$O_i = O_{min} + \xi_O(O_{max} - O_{min}), \quad E_i = E_{min} + \xi_E(E_{max} - E_{min}) \tag{6.11}$$

where ξ_O and ξ_E then belong to the range $[0, 1]$.

Figure 6.3 shows the evolution of the estimations starting from different initial guess values O_i and E_i, for two different dice. As far as filtering is concerned, in the analyses 1000 particles have been adopted and the experimental data have been fed to the filter every 0.5 V (based on the available measurements). Large number of particles allow for better degree of precision at solving the involved

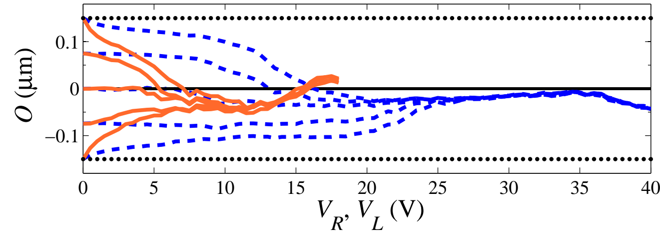

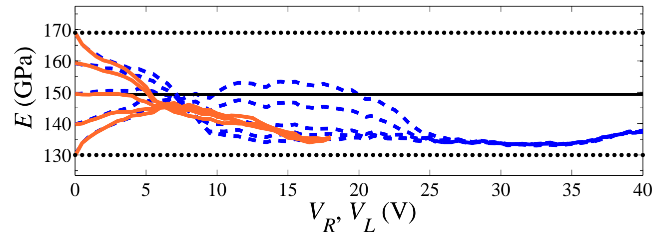

(a)

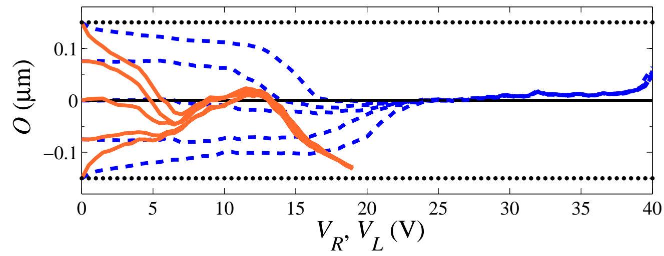

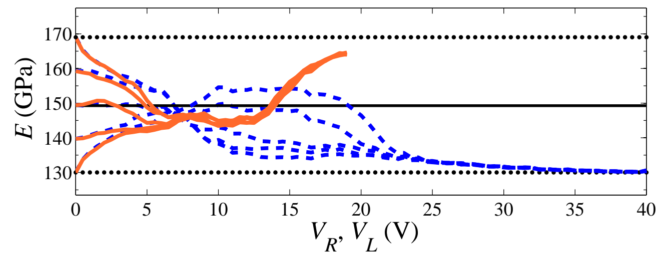

(b)

Figure 6.3: Evolution of the estimates of (top) O and (bottom) E, at varying filter initialization. Blue dashed lines: rotational actuation through V_R; orange solid lines: lateral actuation through V_L. (**a**) Specimen #2, leading to consistent final estimates, and (**b**) specimen #5, leading instead to non-consistent results.

integrals [Cadini et al., 2009]. The process noise covariance matrix $\mathbf{Q}^{v^x}$, linked to the noise term $\mathbf{v}_k^{\mathbf{x}}$ in Eq. (6.1), has been set as $\mathbf{Q}^{v^x} = \mathrm{diag}[\sigma_{v_O}^2 \quad \sigma_{v_E}^2]$ so to handle uncorrelated uncertainties related to the geometry and the film morphology, and to allow both the parameters to evolve within the *a priori* defined domain of variation. The measurement covariance matrix $\mathbf{Q}^w$, linked instead to the term $\mathbf{w}_k$ in Eq. (6.2), has been set as $\mathbf{Q}^w = \mathrm{diag}[\sigma_{w_R}^2 \quad \sigma_{w_L}^2]$ to account for the uncertainties associated to experimental measurements. As far as the results here reported are concerned, the following values for the process and measurement noise covariances have been adopted: $\sigma_{v_O}^2 = 10^{-4}\,\mu\mathrm{m}^2$, $\sigma_{v_E}^2 = 10^{-3} \times \bar{E}^2$, $\sigma_{w_R}^2 = \sigma_{w_L}^2 = 10^{-3}$ fF^2. These values are adopted to allow for i) the error occurring at analytical modelling stage, and ii) and small errors stemming from the specific measurement equipments used in Chapter 3. Graphs in Figure 6.3 show results obtained with the lateral actuation (orange lines) superposed to those obtained with the rotational actuation (blue lines), although relevant to two different series of filter runs. It can be seen that, independently of test case and sample considered, the final estimates of O and E are only marginally affected by the initialization values; accordingly, the filter is proved to properly handle the information brought by measurements, without any kind of instability. As the actuation voltage is increased, the ratio between the response of the device (in terms of capacitance change) and the measurement errors is also increased (see Figures 3.7 and 3.8); a more accurate parameter estimation is thus expected. This is somehow reported in Figure 6.3, since the estimates, starting from different initialization points, first follow different paths and then all merge to provide the mentioned initialization-independent solutions. Since the effects of actuation are larger in the lateral case, the merging of all the curves is shown to happen in this case for smaller values of the applied voltage.

Parameter estimation has been carried out for all the ten samples of length 20 μm mentioned in Chapter 3, whose $C-V$ plots are reported in Figures 3.7 and 3.8, and the relevant final values of the estimates of O and E are reported in Table 6.1. Results can be classified into two sets: those featuring final estimations for the two kinds of actuation matching well each other in the proposed statistical setting; and those providing rather different estimations with the two types of actuation, in terms of the two parameters. Graphs in Figure 6.3(a), referring to

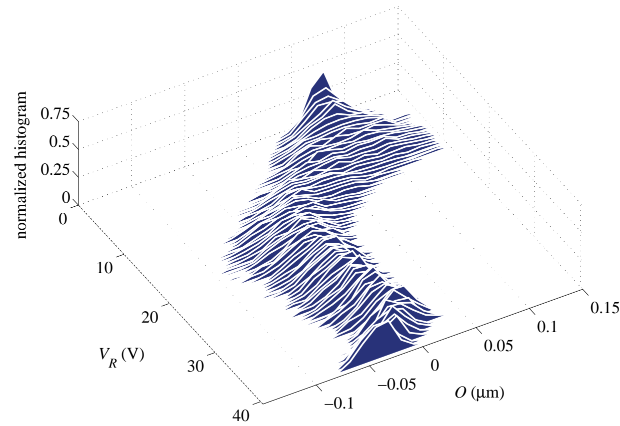

(a)

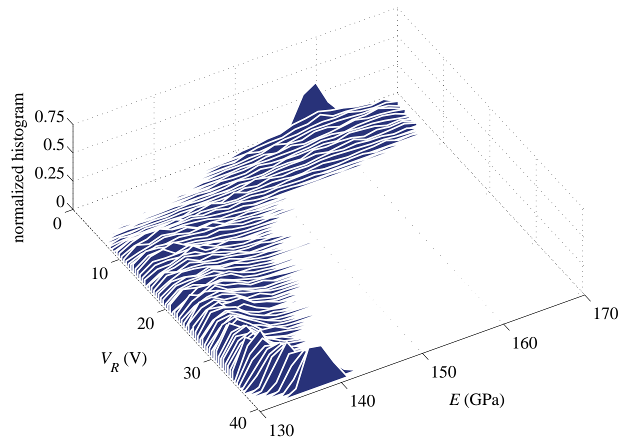

(b)

Figure 6.4: Specimen #2, rotational actuation case, $\xi_O = \xi_E = 0.75$: evolution of the PDFs of (**a**) O and (**b**) E corresponding to the evolution of estimates represented by blue curves in Figure 6.3(a).

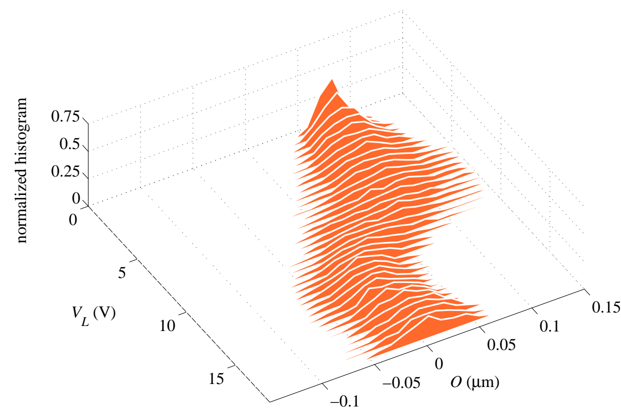

(a)

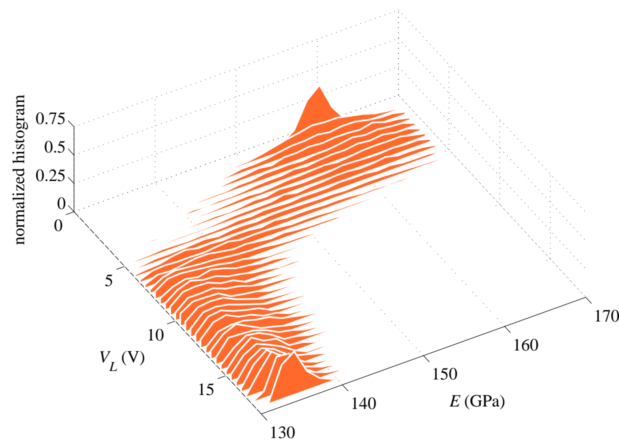

(b)

Figure 6.5: Specimen #2, lateral actuation case, $\xi_O = \xi_E = 0.75$: evolution of the PDFs of (**a**) O and (**b**) E corresponding to the evolution of estimates represented by orange curves in Figure 6.3(a).

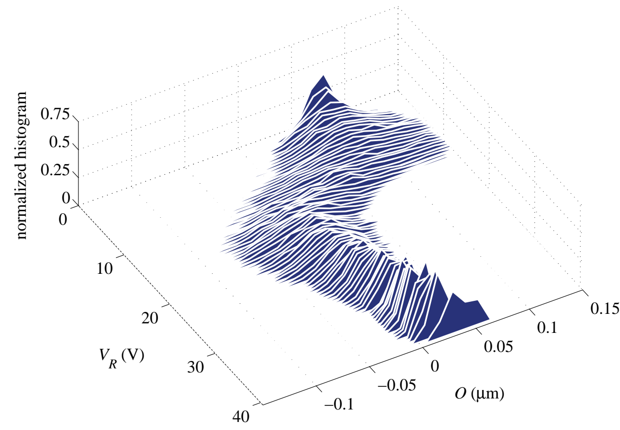

(a)

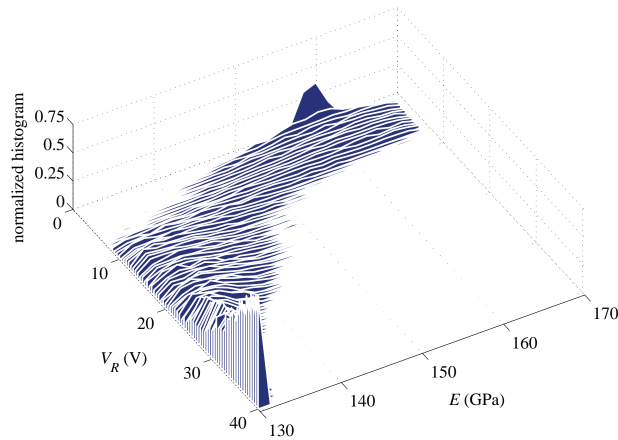

(b)

Figure 6.6: Specimen #5, rotational actuation case, $\xi_O = \xi_E = 0.75$: evolution of the PDFs of (**a**) O and (**b**) E corresponding to the evolution of estimates represented by blue curves in Figure 6.3(b).

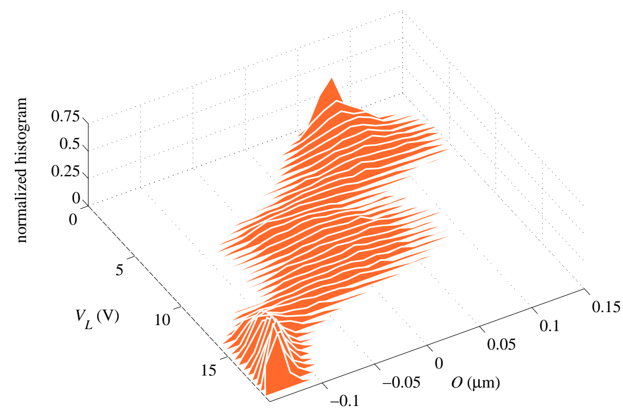

(a)

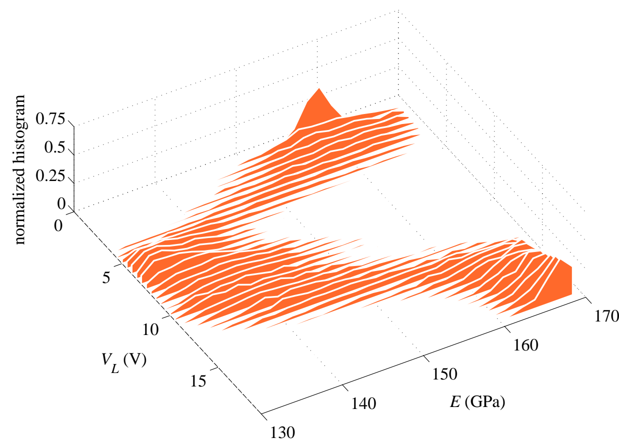

(b)

Figure 6.7: Specimen #5, lateral actuation case, $\xi_O = \xi_E = 0.75$: evolution of the PDFs of (**a**) O and (**b**) E corresponding to the evolution of estimates represented by orange curves in Figure 6.3(b).

Table 6.1: Estimated parameter values through particle filtering.

	O (μm)		E (GPa)	
Specimen #	through V_R	through V_L	through V_R	through V_L
1	-0.13	-0.13	138.4	131.8
2	-0.04	0.02	137.4	135.3
3	0.03	-0.09	134.3	151.9
4	-0.12	-0.07	145.7	132.1
5	0.06	-0.13	130.5	164.2
6	0.01	0.00	144.5	166.3
7	-0.14	-0.15	136.5	130.4
8	-0.14	-0.15	140.1	130.1
9	-0.15	-0.15	159.1	130.1
10	-0.15	-0.15	152.8	130.2

specimen #2, are exemplary of an actuation-independent solution, although the estimations of O are somehow diverging close to pull-in. Graphs in Figure 6.3(b), referring to specimen #5, show instead the pathological divergence of the two solutions, in terms of both O and E, once again maximized close to pull-in.

In addition to the average or expected values reported above, further insights are provided next in terms of evolution of the PDFs of the parameters during the whole filtering procedure. Figures 6.4 and 6.5 gather the evolution of PDFs of the parameters for specimen #2 (consistent estimation), with an initialization at $\xi_O = \xi_E = 0.75$, for the rotational and lateral actuation respectively; these results correspond to the evolution of averages shown in Figure 6.3(a). As it can be seen, the parameters show a similar evolution of the PDFs as the actuation voltage increases up to pull-in, independently of the actuation type. The relatively large superposition of the PDFs of the estimated parameters at the final stages of the procedure, as provided by the rotational and lateral actuations, is basically pointing towards a common statistical solution for the parameters. On the other hand, the PDFs of O and E in Figures 6.6 and 6.7, which correspond to specimen #5 (not consistent estimation) and to the same initialization at $\xi_O = \xi_E = 0.75$, show no superposition with the two types of actuation. Hence, though the procedure is algorithmically stable for each actuation type, estimates do not conform in a

statistical sense and so do not offer a unique solution.

Although the filtering procedure has been shown to be robust, some samples led to different estimates of O and/or E depending on the actuation, or estimates located at the bounds of the initial variation range. Hence, the adopted model might not be accurate enough for all the possible situations encountered: while an effective homogeneous Young's modulus for the polysilicon beam can be appropriate to describe the overall stiffness of each beam (see [Cho and Chasiotis, 2007, Mariani et al., 2011, Mirzazadeh et al., 2015]). Furthermore, small imperfections like e.g. non-zero values of u and θ at no actuation (i.e. for $V_L = V_R = 0$), could lead to a drift or bias in the solution obtained with the particle filter. It has been also assumed that the beam anchors behave ideally, even if several studies have shown that deformation at the anchors [Zhong et al., 2013, Frangi et al., 2013] can induce an additional compliance, and cause discrepancies between the model and measured responses. Moreover, the assumption of a uniform over-etch all around the plate and the beam may fail for different dice in a single wafer.

The particle filter is a more useful tool for systems where on-line parameter estimation methods are needed. However, the measurements have been previously carried out and the data are available. In the next chapter, we enhance the model used in this chapter by introducing another source of uncertainty and adopt off-line parameter estimation methods which handle all available data at once.

7 Off-line parameter estimation: Levenberg-Marquardt and genetic algorithm

7.1 Introduction

As observed in the previous chapters, the scattering of the electromechanical response must be originated from variations both in the mechanical properties and the geometry. A model parameter estimation has been carried out for the overetch and Young's modulus through particle filtering and it was shown that the other sources of uncertainty should be taken into account for more appropriate estimations. In this chapter, we enrich the analytical model by inserting another geometric uncertainty: initial offset displacement of the rotor. Regarding the parameter estimation method, unlike the previous chapter where we used a recursive method, we handle all the experimental data on the system response concurrently, i.e. off-line parameter estimation. In other words, we first collect all the available measurements (whole range of the actuation) and estimate the unknown parameters of the model according to this batch of data. In order to seek for the correct model parameters for each specimen, we investigate the application of two standard optimization techniques to minimize the discrepancy between the model prediction and experimental measurements in terms of the $C-V$ curves. We choose Levenberg-Marquardt (LM) and genetic algorithm (GA) belonging re-

spectively to the deterministic or stochastic type of optimization algorithms. The former type is characterized by the use of deterministic search operators. These algorithms start from a guess on the solution (i.e. unknown parameters) and iteratively determine a direction in the search space (i.e. parameter space) which minimize the error with respect to the previous solution (i.e. objective function). The stochastic algorithms, on the other hand, are characterized by dealing with several points in the parameter space and iteratively examining new points in the parameter space by random operations on the current points.

Section 7.2 and 7.3 describe the LM and GA algorithms in details, respectively. In Section 7.4, the third unknown parameter is introduced into the analytical model. It is shown that the LM algorithm fails at finding the global minimum of the objective function while the adopted genetic algorithm successfully estimates the unknown parameters based on the measurements.

7.2 Levenberg-Marquardt algorithm

The LM algorithm is one of the most efficient and popular deterministic algorithms for determining the unknown parameters of multivariate nonlinear functions in least squares problems, particularly when the number of parameters to be identified is low (typically less than 5) [Rouquette et al., 2007]. In comparison to the similar methods such as, conjugate gradient and resilient back-propagation, the LM algorithm shows better convergence[1] [Sipos et al., 2012, Kişi and Uncuoglu, 2005]. The LM algorithm combines effectively two other deterministic search methods: the gradient descent (GD) and the Gauss-Newton (GN) method. When the current solution (typically at the initiation state) is far from the correct one, the algorithm behaves like the GD method which is slow but highly convergent. As the estimated parameters marches closer to the correct values, the algorithm turns to be similar to the GN method which is rapid in convergence but strongly dependent on the initial conditions.

[1] Trust Region method is also available to this aim which is developed based on the LM algorithm [Yuan, 2000] and can exhibit better convergence performance. However, the algorithmic complexity of this method is much higher than the LM algorithm which explains why the LM method is more popular [Berghen, 2004].

The solution of the parameter identification problem is obtained as the difference between the estimated and the measured response is minimized in a least squares format. Thus, a functional $S(\mathbf{x})$ is defined

$$S(\mathbf{x}) = \|\mathbf{h}(\mathbf{x}) - \mathbf{y}\| \tag{7.1}$$

where $\mathbf{y}$ is the vector collecting the measured response of the system in terms of the capacitance change corresponding to the increasing actuation voltage, $\mathbf{h}$ is the system response for the parameter vector $\mathbf{x}$ and $\|.\|$ denotes the Euclidean norm. In practice, $\mathbf{h}(\mathbf{x}) - \mathbf{y}$ in Eq. (7.1) is a vector collecting the difference between the measured and predicted capacitance change at different values of actuation voltage whose length is the number of voltage steps used at experimental measurements.

The LM algorithm offers the following iterative formula to reduce $S(\mathbf{x})$ with respect to the parameters vector $\mathbf{x}$ [Ozisik, 2000]:

$$\mathbf{x}_{k+1} = \mathbf{x}_k + \left[\mathbf{J}^{\mathrm{T}}\mathbf{J} + \lambda_k \mathrm{diag}(\mathbf{J}^{\mathrm{T}}\mathbf{J})\right]^{-1} \left[\mathbf{J}^{\mathrm{T}}(\mathbf{h}(\mathbf{x}) - \mathbf{y})\right] \tag{7.2}$$

where k is the iteration step. The $n \times m$ sensitivity matrix $\mathbf{J}(\mathbf{x})$ is defined as the Jacobian of $\mathbf{h}$ with respect to the unknown parameters $\mathbf{x}$:

$$\mathbf{J}(\mathbf{x}) = \begin{bmatrix} \frac{\partial h_1}{\partial x_1} & \frac{\partial h_1}{\partial x_2} & \cdots & \frac{\partial h_1}{\partial x_m} \\ \frac{\partial h_2}{\partial x_1} & \frac{\partial h_2}{\partial x_2} & \cdots & \frac{\partial h_2}{\partial x_m} \\ \vdots & \vdots & \ddots & \vdots \\ \frac{\partial h_n}{\partial x_1} & \frac{\partial h_n}{\partial x_2} & \cdots & \frac{\partial h_n}{\partial x_m} \end{bmatrix} \tag{7.3}$$

where n and m are the number of response measurements (i.e. number of voltage steps) and the number of model parameters to be estimated, respectively. This matrix can be either calculated analytically when possible, or approximated through finite-difference method. The term $\lambda_k \mathrm{diag}(\mathbf{J}^{\mathrm{T}}\mathbf{J})$ can be interpreted as a damping term for fluctuation of the estimations which can be modulated by the positive scalar λ_k. This term controls the transition between the GD method ($\lambda_k \to \infty$) and the GN method ($\lambda_k = 0$). The LM algorithm is adaptive because it controls the value of λ_k during the iterations. This parameter is large at the beginning of the iterative procedure, resembling the GD method. This is because

the GD method is advantageous when the current stage is far from the corrected one (which is often the case at the initialization stage). If the updated parameters vector $\mathbf{x}$ computed from Eq. (7.2) leads a reduction in the value of $S(\mathbf{x})$, the update is accepted and λ_k can be reduced (typically by a factor of 10) for the next iteration. Otherwise, Eq. (7.2) will be solved with an increased damping term. This step will be repeated for increasing values of λ_k until an acceptable update for the parameters vector is found.

7.3 Genetic algorithms

Genetic algorithms (GAs) are a stochastic search method widely used for optimization, based mainly on evolutionary ideas of genetics and natural selection. The general idea of genetic algorithms as simulations of evolution first appeared in 1967 in Bagley's Thesis titled "The behavior of adaptive systems which employ genetic and correlative algorithms" [Bagley, 1967]. These algorithms were first suggested in the 1970s by John Holland in the United States [Holland, 1975], and by Ingo Rechenberg in Germany [Rechenberg, 1973]. Based on simplification of evolutionary theory, GAs work on a populations of candidate solutions, and employ heuristics such as selection, crossover, and mutation to evolve the population's members over sequential generations. The basic steps behind GAs can be summarized as following.

1. Generate a random initial population composed of n_P candidate solutions.
2. Evaluate the fitness value for each member of the current population using the objective function.
3. Select the so-called parents i.e. members, based on their fitness value for reproduction purpose.
4. Pass a number of best parents so-called elite to the next generation population.
5. Generate offspring by combining the characteristics of two parents, *crossover*, and by applying variations (based on any specific probability distribution) to a parent or to the newly generated offspring, *mutation*.

6. Replace the current population with the newly generated offspring.

7. Perform the steps 2 to 6 until a termination condition is met, such as maximum number of generations or minimum change in the value of the best fitness between two generations.

The initial population should be selected according to the existing prior knowledge of the zones in parameter space with higher probability of solution. In absence of such information, a general and safe practice is to use a random distribution of population over the search area to increase the chance of locating the zone of the solution. Regarding the offspring generation, beside the passing so-called elite members which hold the best current solution, use of both *crossover* and *mutation* is necessary. The former enables the algorithm to combine the elements of the best solutions (parents) to generate possibly superior offspring (children) which is the basic idea behind evolution. The latter instead prevents the loss of diversity [Holland, 1975] which helps the chance of generating individuals with better fitness value and locating the correct solution.

In the next section, we adopt these two methods, the LM and the GA, for estimation of the unknown parameters of the test devices.

7.4 Discussion on the results

The aforementioned optimization methods have been used in a parameter estimation framework. As for the objective function to be minimized, the normalized discrepancy between the measured capacitance and the model predictions has been chosen. In this regard, the same idea of cross validation of Chapter 6 has been employed; the identification process is repeated once for each actuation type, using both sensing types.

As concluded in the Chapter 6, the model needs to be further enhanced by considering other sources of uncertainties to better match the experimental data. In this regard, the next likely parameter to be considered is an initial offset displacement of the central rotor which can heavily affect the system response and is prone to changes due to the fabrication process. This rotor displacement can

be parametrized by an initial beam-end deflection u_0, and an initial beam-end rotation, θ_0, depicted in Figure 7.1. Between the two, the beam-end rotation is the prominent parameter. The effects of initial beam-end deflection for the rotational capacitors, both at actuation and sensing, is negligible since u_0 can be assumed to occur in the direction almost parallel to the capacitors and does not change the gap g_R. Since the expected values for u_0 are in order of tens of nm and are relatively small to the gap distance g_0=2 μm (see Figure 3.2), such changes do not also alter the system behaviour at the lateral capacitor accordingly. Therefore, in the following we take into account the rotation offset value θ_0 only. Insertion of this parameter into the analytical model provided in Chapter 4 is carried out by a simple modification as $\theta \rightarrow \theta + \theta_0$.

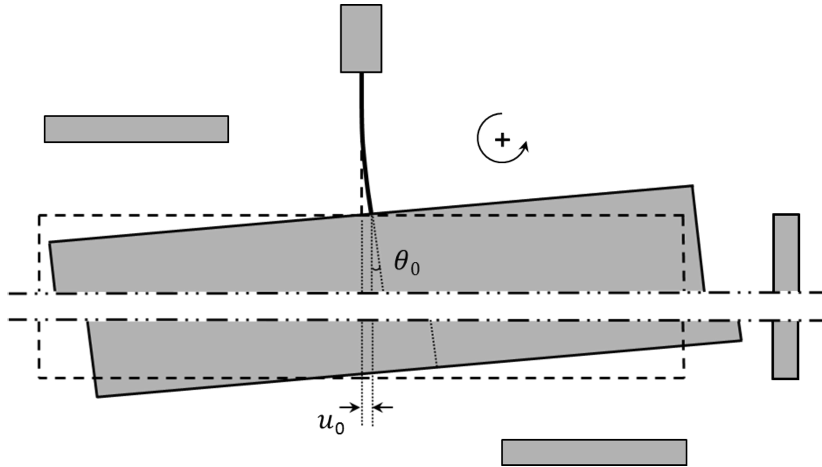

Figure 7.1: Initial offset displacement parametrized by u_0 and θ_0. Displacements not to scale.

Using the three unknown parameters namely, O, E and θ_0, the sensitivity of the response to these parameters is investigated first; for such purpose, one may observe the capacitance change corresponding to an arbitrary actuation voltage. The variation range of over-etch and Young's modulus can be chosen within the domain $O \in [O_{min}$=-0.15 μm, O_{max}=0.15 μm] based on the specifications of the fabrication process or $E \in [E_{min}$=130 GPa, E_{max}=169 GPa] based on the admissible values of Young's modulus for silicon plane (100), similar to the analyses in

Chapter 6. In order to have a physical understanding of the variation range of rotation offset, we have resorted to the pull-in instability configuration. In a separate analysis, the rotation angle corresponding to pull-in instability for rotational and lateral actuation have been obtained as -0.0088 and 0.0042 rad, respectively (counterclockwise rotation is positive, see Figure 7.1). These values are calculated using reference values for over-etch and Young's modulus, i.e. O=0 μm and E=149.3 GPa. Taking those calculations into account, the variation range for the offset has been set as $\theta_0 \in [\theta_{0min}$=-0.004 rad, θ_{0max}=0.004 rad].

First, we investigate the effects of the variation of these three parameters on the response of the system. Figure 7.2 reports the developed capacitance change at the rotational capacitors when a voltage difference V_R = 37 V is applied at the same capacitors (20μm RR case according to Figure 3.7(a)). As it can be observed, all the three parameters effectively change the device response. In the case of over-etch, the capacitance change varies in a strong nonlinear fashion, while Young's modulus and the rotation offset have a quasi linear effect. Looking at the variation of capacitance change, it is also clear that the over-etch and Young's modulus exhibit stronger influence. Similar behaviour can be seen in the response of LL case when a voltage difference V_L = 15 V is applied to the lateral capacitor. The only difference is linked to the direction of the rotation offset; in the present convention, positive rotation offset decreases the gap between the rotational capacitors and increases the one between the lateral capacitor, see Figures 7.2 (c) and 7.3 (c).

Comparing LM and GA method, LM is the first choice, since its computational burden is typically lower than GA method. The difference is simply due to the fact that LM is a gradient based method which tries to find the solution (minima/maxima) by determining the appropriate search direction; therefore, a lower number of simulations is required. However, this method requires a guess for the initialization of the algorithm. On the other hand, GA starts with a random initial population in the absence of *a priori* statistical knowledge of the solution.

As mentioned above, as the first attempt, the LM method has been adopted due its lower computational burden. However, such optimization method must be carried out for different initialization values first to ensure its robustness. We use the measured capacitance change at both capacitors when actuation voltage

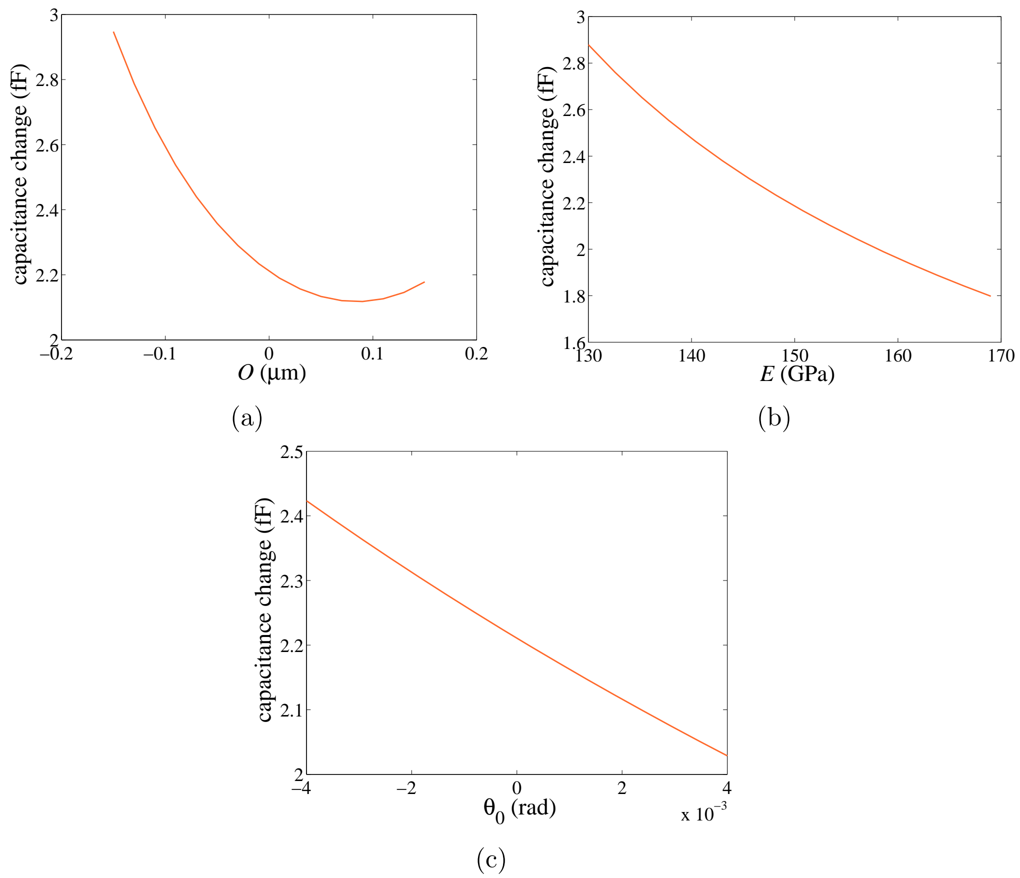

Figure 7.2: RR case, V_R =37 V, variation of the device response at varying (**a**) overetch O, (**b**) Young's modulus E and (**c**) rotation offset θ_0.

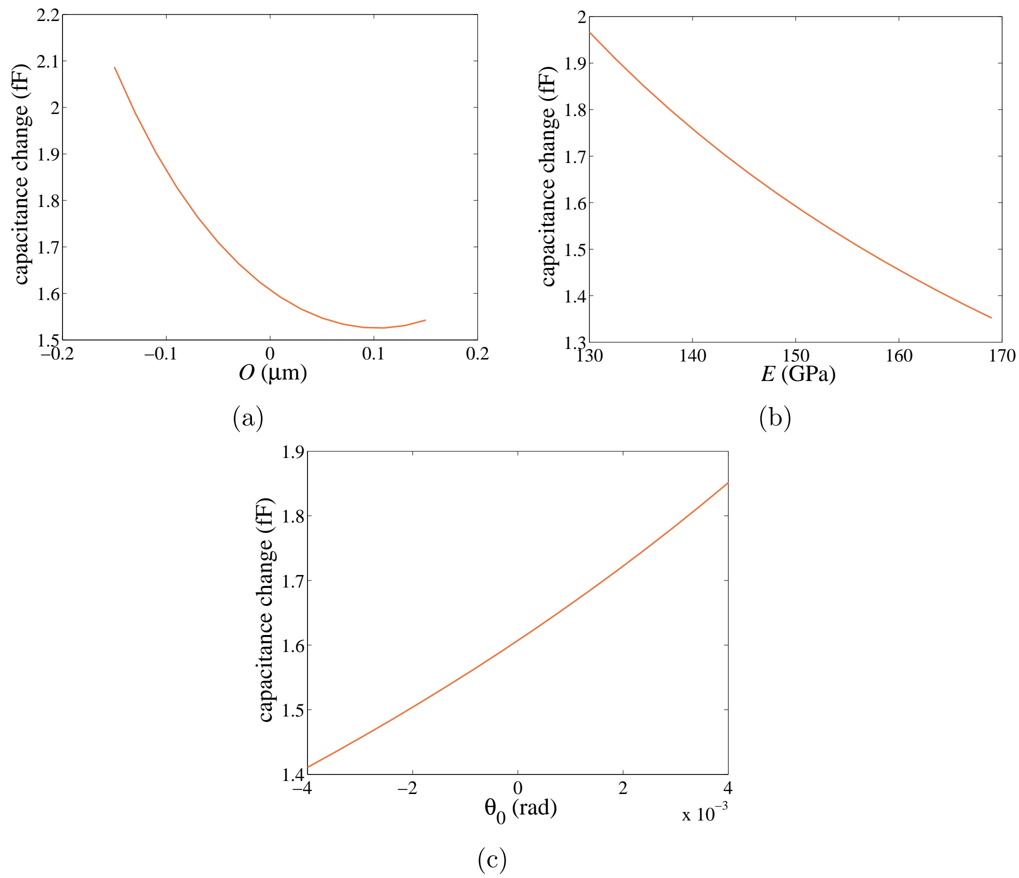

Figure 7.3: LL case, V_L =15 V, variation of the device response at varying (**a**) overetch O, (**b**) Young's modulus E and (**c**) rotation offset θ_0.

is applied to the rotational capacitors (RR and RL cases) for specimen #2 of 20 μm micro beam family. The identified results are shown in the maps of Figure 7.4, where the values of identified parameters O, E and θ_0 at the end of the iterative method are represented as functions of the initialization values O_i and E_i while keeping the initial guess of rotation offset θ_{0i} to be zero (nominal design values). Each map derives from a grid of 5×5 initialization points inside the admissible domain. Similar maps can be derived for pairs of θ_0 with either E_i or O_i. It can be observed from Figure 7.4 that the identification process is heavily dependent on the initialization values which invalidates the robustness of the method. In other words, the LM method was not capable of finding the global solution to a unique optimization problem.

As means to escape from the local minima/maxima, one can impose further regularity conditions on the functional $S(\mathbf{x})$ i.e.

$$S(\mathbf{x}) = \|\mathbf{h}(\mathbf{x}) - \mathbf{y}\| + \boldsymbol{\gamma}\|\mathbf{x} - \mathbf{x}_0\| \tag{7.4}$$

where the vector of the regularization parameters $\boldsymbol{\gamma} > \mathbf{0}$ and the vector of *a priori* guess on the parameters $\mathbf{x}_0 \in [\mathbf{x}_{min} \quad \mathbf{x}_{max}]$ should be given to the problem. This type of regularization is known as nonlinear Tikhonov regularization in the literature [Bissantz et al., 2004]. The regularization parameter defines the rate of convergence of the iterative procedure toward the *a priori* guess. This parameter demonstrates the degree of confidence in the guess. The choice of the *a priori* guess is crucial to this method and can be derived from a set of individual experiments or the expert guess on the unknown parameter. In the present investigation, we lack such insight into the value of the unknown parameters of the devices. Thus using such regularization method would be unjustified and is not pursued in this work.

Thereby, we resort to GAs as a global optimization strategy [Patelli et al., 2014]. The same scheme of cross-validation has been also adopted in this set of analyses. Since the sought parameters are independent of the type of actuation, the parameter estimation procedure can be carried out for the two actuation types separately, to cross-validate the estimations. The population size to explore the parameter space (also known as design or search space) is an important factor

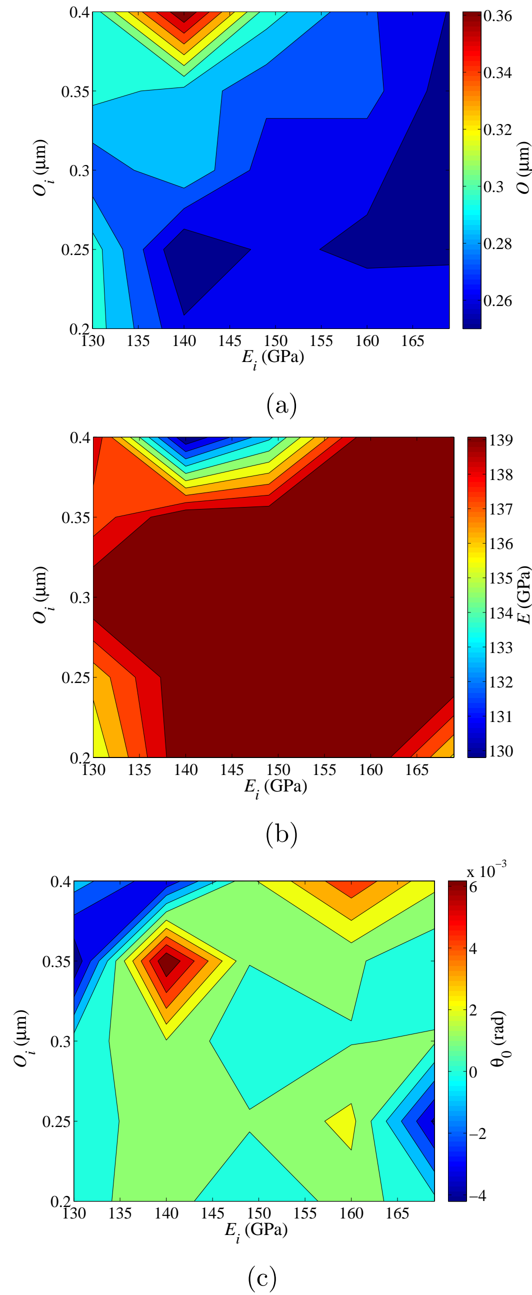

Figure 7.4: Effect of initialization on the estimated parameters: (**a**) Overetch O, (**b**) Young's modulus E and (**c**) rotation offset θ_0.

which determines the efficiency of the procedure [Chen et al., 2015, Chen et al., 2012]. Large population will clearly require numerous evaluations and thus, more computational effort is needed. On the other hand, assigning a large population generally is advantageous as it allows a thorough space search and accordingly a higher chance for finding the true global minima/maxima.

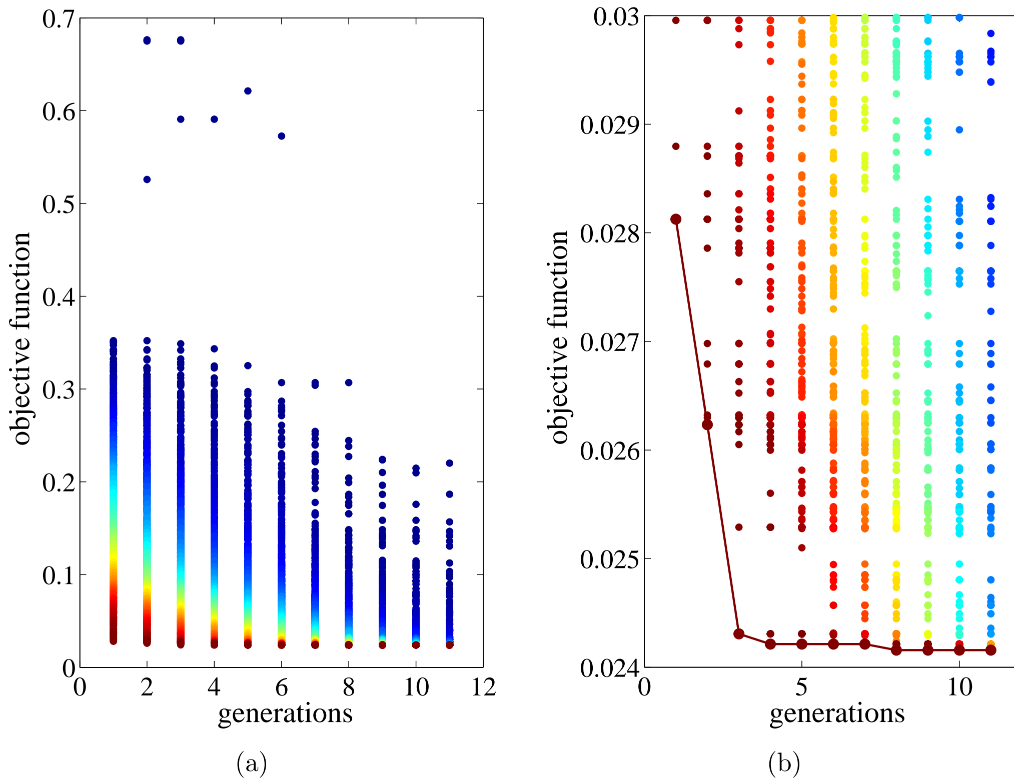

Figure 7.5: (**a**) Convergence of the objective discrepancy function at increasing generations, and (**b**) close-up of the plot and best score trend.

To estimate the value of the unknown parameters parameters O, E and θ_0, a genetic algorithm with a population of 5000 individuals has been adopted which converges before 11 generations. The individuals population has been assessed based on several trials with different populations to ensure the robustness of the algorithm. Figure 7.5(a) shows the convergence of the genetic algorithm in terms of the objective function value for the exemplary case of specimen # 2; Figure

7.5(b) illustrates the close-up view of the bottom part of the Figure 7.5(a) along with the trend of the best individual score. Each dot in the figures stands for the objective function value for one individual. The color is assigned so that dark blue stands for the individual which shows the largest objective function value, and dark red stands for the best individual at each generation (corresponding to the smaller objective function value). At the evaluation of first generation (random spread of individuals within the parameters space), the individuals show a wide range of values of the objective functions; as the generations advance, the individuals move to the bottom of the graph concentrating around the best possible solution. It can be observed that the rate of convergence is relatively high, since the number of individuals is large; although the convergence of the algorithm occurs at the 8th generation, the fluctuation in the objective function after the 4th is quite negligible as for the best solution. However, it is worth noting that the computation cost for this parameter estimation for each specimen is less than 30 min on a personal computer with an Intel®Core™i7 3.00 GHz processor thanks to adopting the analytical model.

Table 7.1: Estimated parameters values through GA.

	E (GPa)		O (μm)		θ_0 (milliradian)	
Specimen #	through V_R	through V_L	through V_R	through V_L	through V_R	through V_L
1	134.6	131.6	-0.10	-0.05	0.08	0.34
2	147.6	137.7	-0.09	-0.02	-0.15	0.07
3	150.8	153.2	-0.09	-0.13	-0.31	-0.30
4	149.5	130.7	-0.12	-0.07	-0.01	-0.05
5	149.5	141.8	-0.09	-0.10	-0.55	-0.56
6	161.5	144.2	-0.07	-0.07	-0.42	-0.85
7	130.3	134.3	-0.10	-0.10	0.07	0.41
8	134.0	130.2	-0.12	-0.06	0.12	0.46
9	131.1	135.5	-0.04	-0.05	0.91	1.00
10	132.2	142.6	-0.06	-0.12	0.52	0.53
mean	142.1	138.2	-0.09	-0.08	0.03	0.10
standard deviation	10.9	7.3	0.03	0.03	0.44	0.56

The parameter estimation procedure based on the GA has been carried out on each specimen; the relevant estimated parameters are reported in Table 7.1. The values are categorized under the two actuation types, V_R and V_L. These values can be compared one to another to cross-validate the procedure for each specimen. By inspecting the outcomes, it clearly emerges that the current identification

attempt has provided better results than those reported in Chapter 6, featuring more consistency between the two sets of estimated values. The reason behind this improvement is linked to the third handled unknown parameter, the rotation offset θ_0, which allows to model the scatterings in the initial configuration due to possible residual stress and/or stress gradient effects. Despite the improvement, there are still some specimen for which the method was not able to generate consistent results (e.g. specimens #4 and #6).

More insights into the uncertainties can be obtained through further enhancements, using numerical models instead of the analytical ones. Numerical models, such as finite element ones, are supposed to provide better results as they can allow for additional unknown parameters. On the other hand, the use of Bayesian tools is generally favorable compared to the approaches providing deterministic estimates (such as the one adopted in this chapter) when the measurement errors have to be properly dealt with. These enhancements, within the frame of a complete uncertainty quantification scheme, are provided in the next chapter.

8

Reduced order modelling and off-line Bayesian parameter estimation

Although the fastest computers can execute millions of operations in one second they are always too slow. This may seem a paradox, but the heart of the matter is: the bigger and better computers become, the larger are the problems scientists and engineers want to solve.

- Arhur Jaffe, *Ordering the universe: the role of mathematics, 1984.*

8.1 Introduction

Given a complete description of the system, the descriptive models can predict the behaviour of the system which is generally known as direct or forward problem. It happens that some parameters (or characteristics) of the physical system are unknown, but it is sometimes possible to *infer* them from some observations on the system's response; this is instead known as inverse problem which is often associated with large-scale simulations at varying unknown parameter. When dealing with complicated physical systems, analytical models might not be available, the numerical methods such as FE models can instead offer effective and versatile simulation tools. However, their computational burden is usually much larger than that of the analytical models. Therefore, employing them in an inverse

analysis framework can be prohibitive.

Even though, the computation capabilities of computers are increasing and the computational burden can be divided by exploiting parallel computing architectures, it is usually not sufficient and a more effective solution must be devised. As for the particular system in this work, the analytical model developed in Chapter 4 shows some limitations when anchor compliance become more significant (which occurs at shorter beams) or several sources of uncertainties have to be taken into account, and therefore, FE modeling can be adopted in the parameter estimation process (which is an inverse problem, in nature). The numerical model provided in Chapter 4 is a nonlinear coupled-physics model and naturally time consuming (as confirmed in Chapter 4).

The problem can be treated by reducing drastically the computational effort needed in FE models by a non-intrusive method based on the proper orthogonal decomposition (POD) and kriging metamodelling (also known as kriging surrogate modelling[1]). Unlike the intrusive methods which require access to the FE source code in order to modify it, the non-intrusive methods are simpler and only need a set of input/output (snapshots) of the FE model regardless of the source code. This is the main advantage of the non-intrusive approaches that makes them interesting for dealing with complex multi-physics problems [Fossati and Habashi, 2013]. In the method adopted here, the time-consuming FE simulations are carried out once for all, and in the parameter estimation procedure are replaced by a new computationally fast model. As for the parameter estimation method, transitional Markov chain Monte Carlo (TMCMC) has been adopted to i) deal with the unknown parameters as stochastic variables (in contrast to genetic algorithms) and also ii) handle all measured data at once in an off-line format (in contrast to particle filtering). The main goal of this chapter, is rather than focusing on the test device explored in the previous chapters, to propose a full practical methodology for uncertain parameter identification in a general multi-physics nonlinear problem.

This chapter starts with a review of the available computational reduction methods in the literature in Section 8.2. Two of these methods (i.e. POD based

[1] Surrogate models provide an approximation of the input/output map by fitting a set of data/solutions obtained by numerical simulation [Manzoni et al., 2012].

model order reduction and surrogate modelling) are next detailed in the rest of the section to address the computational reduction of nonlinear multi-physics systems. Section 8.3 describes the basic ideas behind the POD and how it can be used for model order reduction. Section 8.4 instead gives a review of the available surrogate models and in specific focuses on kriging method. Section 8.5 provides the link between these two methods and explains how they can be adopted for computational reduction. The requirements (i.e. sampling) for constructing this computationally fast model is also discussed in this section. The TMCMC method for Baysian parameter estimation (or inverse modelling) developed in [Ching and Chen, 2007] is introduced in Section 8.6. Utilization of the complete framework (i.e. POD-kriging TMCMC) is finally exemplified in Section 8.7 by using the FE model provided in Chapter 4, and based on the experimental data of Chapter 3.

8.2 Methods for computational reduction

The demand for computational engineering and numerical simulations has been constantly rising during the last decades. Such methods provide the researchers with virtual testing experiments for response prediction or optimization purposes at lower cost/time with respect to experimentation. Constant development of algorithms and computers have always led the application of these methods toward ever larger and more complicated problems. Currently, the engineering problems can easily be nonlinear or related to multi-scale and multi-physics phenomena and involve up to millions of degrees of freedom due to complicated geometries. On the other hand, novel parallel architecture and the hardware improvements, both at process and storage capacity, always lag behind the computational demand of such problems. Computational burden reduction methods offer solutions to these complicated problems without loosing much accuracy.

A wide range of methods for computational burden reduction have been proposed and, depending on the main idea behind each method and its application, a different classification can be made. For instance, when the dimensions of the problem and the material length scale or the load wavelength are far from one another, a popular approach is the hierarchical multi-scale simulations which are adopted in different applications such as classical or gradient based homogeniza-

tion [Geers et al., 2010, Kouznetsova et al., 2002], modeling the response of composites [Stefanou et al., 2015], crack propagation simulation [Oliver et al., 2015] or wave propagation [Mariani et al., 2009].

Another category is the domain decomposition [Gosselet and Rey, 2006, Fragakis and Papadrakakis, 2003] where the physical domain is divided into sub-domains, wherein the governing equations are first solved disjointedly and then coupled together, by enforcing continuity of some kinematic fields or forces, at all the interfaces between adjacent sub-domains. This technique is naturally advantageous when applied to the solution of problems of large size or characterized by different physical domains co-existing. Their goal is indeed to significantly increase the computational efficiency of the numerical simulations as they allow for i) a sensible reduction of the number of degrees of freedom or ii) relaxing the time-step constraints encountered with the standard description in an explicit dynamic scheme (i.e. Courant condition), for each sub-domain with respect to those of the whole domain [Confalonieri, 2013]. Such methodology has been adopted for multi-physics problems [Corigliano et al., 2013], fracture simulations [Confalonieri et al., 2014], elastic-plastic structural analysis [Corigliano et al., 2015] and fluid-solid interaction [Deparis et al., 2004].

Furthermore, there are the model order reduction (MOR) techniques. The key concept behind these techniques, is to reduce the dimension of the original algebraic system arising from the discretization of a partial differential equation problem. Unlike domain decomposition approach where the problem is divided in several sub-domains, MOR techniques replace large-scale computational models by simpler ones, still capable of reproducing their essential features, obtained by projecting the full-order model onto a much smaller subspace spanned by a reduced set of bases. As for such basis, the proper orthogonal decomposition (POD) [Kerschen et al., 2005] is able to provide "ad hoc" basis tailored on the specific simulation case, thanks to its optimality property (see Section 8.3). This property efficiently allows to obtain the most dominant components of a solution space with usually a set of few bases (also known as modes) [Berkooz et al., 1993]. Given a linear time invariant systems, projection of the full-order system using optimal basis can be effective and accurate since it is carried out only once. If model order reduction for a general nonlinear problem or for a parametric model (i.e. para-

metric model order reduction or PMOR) is instead of concern, such as the present problem, the procedure features a hidden computational difficulty [Paul-Dubois-Taine and Amsallem, 2015, Rudnyi and Korvink, 2002, Radermacher and Reese, 2015]. Having calculated the optimal basis (let's assume the calculated POD basis is perfectly representing the nonlinear nature of the system), the full-order system matrices (e.g. stiffness matrix and load vector for a static problem) are projected on a lower order space to construct the reduced systems. These reduced matrices should be computed either by use of symbolic manipulation which is not always feasible, or numerically for each iteration of a nonlinear analysis. That means that the original full-order system matrices must be accordingly computed at the end of an iteration to be then reduced by the use of the orthogonal bases for the next iteration. This step adds a considerable computational burden that overshadows the advantages of the model reduction, except perhaps for the case when size of the problem is extremely large.

Here in this work, we adopt a similar technique to that originally presented in [Ostrowski et al., 2005] for thermal problems and later used in [Buljak and Maier, 2011] for plasticity. It is a non-intrusive technique and can be easily implemented along with any solver for the full-order model (such as commercial FE codes) which makes it interesting for industrial applications. It avoids the above mentioned hurdle by using POD, not to reduce the system matrices, but to optimally find the correlation among sampled solutions of the full-order problem corresponding to a set of assumed values of the parameters (i.e. model parameters or time). The POD produces low-order approximation of the response (for instance, displacement field); therefore, the arbitrary solution of the full-order can be expressed as a linear combination of only few basis vectors. As for the MEMS test devices, the POD can be used to reduce the number of the required outputs (the measured data points in the $C-V$ curves). If used in an inverse problem algorithm (or parameter estimation), beside the significant computational gain, it can also help the stability of the algorithm [Ostrowski et al., 2005]. In the following, we investigate the proposed approach further in detail.

8.3 Model order reduction: proper orthogonal decomposition

The main goal behind MOR is to provide the approximation of a physical problem at a low computational burden without resorting to the common computationally demanding numerical techniques. Such technique is essentially based on a high-fidelity, computationally expensive discretization scheme. The choice between the accuracy of the approximation and the level of computational burden reduction is the main trade-off in such methods.

In the computational burden reduction techniques, like POD, the attempt is to project the high-dimensionality problem onto a set of suitable low dimensional subspaces. The essential components of such techniques are the following.

- High-fidelity discretization technique. As mentioned earlier, the POD technique is an *a posteriori* technique, based on some knowledge on the problem solution. A MOR technique based on POD does not replace completely a high-fidelity one like the FEM. Generally, we will rely on a numerical model (e.g. the FE approximation) as the reference discretization method.

- Reduced basis. The main ingredient of MOR is the reduced basis constructed from a finite set of high-fidelity solutions (snapshots). The objective is to find a reduced approximation of the high-fidelity model output as a linear combination of the basis functions which can be obtained via singular value decomposition (described in remainder of this section).

- Training/emulating procedure. Firstly, in a *training* stage, an extensive set of the high fidelity solutions are gathered in the snapshots database which is performed off-line once. Then, each subsequent input-output query is carried out in an *emulating* stage. Clearly, the reduced problem can be solved during the *emulating* stage for any set of parameters not selected in the *training* stage. The first stage, involves the expensive computation upon which the reduced model is supposed to be built.

A general and synthetic introduction to POD technique in view of the reduction of a dynamical system (i.e. the first and the most popular application of this strategy) can be found in [Volkwein, 2011]. We shortly review here the

main features of the POD necessary to build the model-specific optimal linear subspace according to an ensemble of model responses (by varying the model parameters, e.g. boundary conditions, geometric configuration or material properties). Given a real vector $\boldsymbol{u} \in \mathbb{R}^m$, $\mathbb{R}$ being the set of real numbers and m denoting the dimension of vector $\boldsymbol{u}$, we assume a set of arbitrary orthonormal bases vector $\boldsymbol{\phi}_i \in \mathbb{R}(i = 1, 2..., m)$ which satisfies $\boldsymbol{\phi}_i^{\mathrm{T}} \boldsymbol{\phi}_j = \delta_{ij}(i, j = 1, 2, ..., m)$, where δ_{ij} is the Kronecker's delta. The original vector $\boldsymbol{u}$ can then be written as a linear combination of the bases as

$$\boldsymbol{u} = \sum_{i=1}^{m} \boldsymbol{\phi}_i a_i = \boldsymbol{\Phi} \boldsymbol{a} \tag{8.1}$$

where a_i represent the unknown amplitudes of the expansion, also known as coefficients. These coefficients are gathered in the column vector $\boldsymbol{a}$, and $\boldsymbol{\Phi} = [\boldsymbol{\phi}_1, \boldsymbol{\phi}_2, ..., \boldsymbol{\phi}_m]$ is the bases matrix. A reduction in the computational cost can be obtained by the following representation

$$\boldsymbol{u} \approx \hat{\boldsymbol{u}} = \sum_{i=1}^{r} \boldsymbol{\phi}_i a_i = \hat{\boldsymbol{\Phi}} \hat{\boldsymbol{a}} \tag{8.2}$$

where $r < m$. The reduced bases matrix $\hat{\boldsymbol{\Phi}}$ consists of r columns of $\boldsymbol{\Phi}$, and the vector $\hat{\boldsymbol{a}}$ collects the relevant first r entries of $\boldsymbol{a}$. The computational gain is related to the degree r, smaller than m. The final objective in POD is to provide an optimal set of bases able to minimize the sum of the squared projection errors:

$$\min \|\boldsymbol{u} - \hat{\boldsymbol{u}}\| \tag{8.3}$$

which $\|.\|$ represents the L^2 norm. The so-called snapshot version of POD introduced by Sirovich [Sirovich, 1987] can address two problems: first, the choice of r which determines the computational gain and the accuracy of the approximation; second, the computation of the bases gathered in $\hat{\boldsymbol{\Phi}}$. In practice, the snapshot vector $\boldsymbol{u}$ is the measurable response of a physical system defined by a set of parameters space (the vector collecting the displacement field at a given boundary condition, for instance). Accordingly, n observations of a m-dimensional vector $\boldsymbol{u}$

can be collected in the snapshot matrix $\boldsymbol{U}_{m\times n}$ as

$$\boldsymbol{U} = [\boldsymbol{u}_1, \boldsymbol{u}_2, ..., \boldsymbol{u}_n] = \begin{bmatrix} u_{11} & u_{12} & \cdots & u_{1n} \\ u_{21} & u_{22} & \cdots & u_{2n} \\ \vdots & \vdots & \ddots & \vdots \\ u_{m1} & u_{m2} & \cdots & u_{mn} \end{bmatrix} \tag{8.4}$$

In the literature, several means of computing the POD have been proposed, e.g. eigensolutions of the sample coviariance matrix, singular value decomposition of the snapshot matrix and auto-associative neural networks. A review of these methods can be found in [Kerschen et al., 2005]. Here, we exploit the singular value decomposition method[1] to deal with the snapshot matrix.

For any real matrix, like the snapshot matrix $\boldsymbol{U}$, there exists a factorization called the singular value decomposition (SVD) that can be written as [Liang et al., 2002]:

$$\boldsymbol{U} = \boldsymbol{L}\boldsymbol{S}\boldsymbol{R}^{\mathrm{T}} \tag{8.5}$$

where $\boldsymbol{L}_{m\times m}$ is an orthonormal matrix whose columns are the left singular vectors of $\boldsymbol{U}$; $\boldsymbol{S}_{m\times n}$ is a pseudo-diagonal and semi-positive definite matrix whose diagonal entries are the singular values of $\boldsymbol{U}$; and $\boldsymbol{R}_{n\times n}$ is an orthonormal matrix whose columns are the right singular vectors of $\boldsymbol{U}$. Given

$$\boldsymbol{U}\boldsymbol{U}^{\mathrm{T}} = \boldsymbol{L}\boldsymbol{S}^2\boldsymbol{L}^{\mathrm{T}} \qquad \text{and} \qquad \boldsymbol{U}^{\mathrm{T}}\boldsymbol{U} = \boldsymbol{R}\boldsymbol{S}^2\boldsymbol{R}^{\mathrm{T}}, \tag{8.6}$$

where $\boldsymbol{S}^2$ is the pseudo-diagonal matrix having S_{ii}^2 on the main diagonal, the singular values of $\boldsymbol{U}$ are the square root of the eigenvalues of $\boldsymbol{U}\boldsymbol{U}^{\mathrm{T}}$ or $\boldsymbol{U}^{\mathrm{T}}\boldsymbol{U}$; the left and right singular vectors of $\boldsymbol{U}$ are the eigenvectors of $\boldsymbol{U}\boldsymbol{U}^{\mathrm{T}}$ and $\boldsymbol{U}^{\mathrm{T}}\boldsymbol{U}$, respectively.

The complete basis set $\boldsymbol{\Phi}$ is given by the columns of $\boldsymbol{L}$, also known as proper orthogonal modes (POMs) [Eftekhar Azam and Mariani, 2013]. If the singular

[1] It is noted that the Karhunen Loéve decomposition (KLD) and principal component analysis (PCA) are closely connected to the POD-SVD method and the reader is referred to [Wu et al., 2003, Liang et al., 2002, Feeny and Kappagantu, 1998, Mees et al., 1987] for detailed discussion on their equivalence.

values S_{ii} of $\boldsymbol{U}$ are sorted in a decreasing order, and the columns of $\boldsymbol{L}$ and $\boldsymbol{R}$ are accordingly arranged, the SVD of Eq. (8.5) is such that the first r (for given r) columns of $\boldsymbol{\Phi} = \boldsymbol{L}$ represent the optimal basis subset that fulfills the minimization problem of Eq. (8.3). The index r can be chosen such that [Braconnier et al., 2011]

$$r = \inf_k \frac{\sum_{i=1}^{k} S_{ii}}{\sum_{i=1}^{m} S_{ii}} \geq err \tag{8.7}$$

where err is an arbitrary error threshold. Therefore, we can reproduce the snapshot matrix $\boldsymbol{U}_{m\times n}$ exactly using the new orthonormal bases $\boldsymbol{\Phi}_{m\times m}$ as

$$\boldsymbol{U} = \boldsymbol{\Phi}\boldsymbol{A} \tag{8.8}$$

where $\boldsymbol{A}$ is a matrix of coefficient which gathers the vectors $\boldsymbol{a}_i, i = 1, 2, ..., n$. Eq. (8.8) yields in fact an alternative representation of snapshot matrix in a new coordinate system given by $\boldsymbol{\Phi}$. To calculate the coefficient matrix $\boldsymbol{A}$, we can use the orthogonality condition of the POMs

$$\boldsymbol{A} = \boldsymbol{\Phi}^{\mathrm{T}}\boldsymbol{U} \tag{8.9}$$

Instead, the coefficient vector $\boldsymbol{a}$ for the i-th snapshot vector $\boldsymbol{u}$ reads

$$\boldsymbol{a}_i = \boldsymbol{\Phi}^{\mathrm{T}}\boldsymbol{u}_i, \quad i = 1, 2, ..., n \tag{8.10}$$

The approximation can then be done by

$$\hat{\boldsymbol{u}}_i = \hat{\boldsymbol{\Phi}}\hat{\boldsymbol{a}}_i, \quad i = 1, 2, ..., n \tag{8.11}$$

or in a matrix format

$$\hat{\boldsymbol{U}} = \hat{\boldsymbol{\Phi}}\hat{\boldsymbol{A}} \tag{8.12}$$

$\hat{\boldsymbol{U}}$ and $\hat{\boldsymbol{u}}$ are the approximation of their original counterparts $\boldsymbol{U}$ and $\boldsymbol{u}$, respectively.

This approximation expressed by Eq. (8.12) is, strictly speaking, valid only for the snapshots that have been used to construct the POD basis. As far as a parametric model order reduction is concerned, it is necessary to ensure the capability

to approximate the system response, different from the snapshots. In other words, we have already obtained the system response collected in the snapshot matrix corresponding to a given sets of parameters defining the system (i.e. simulated responses), but we are interested to approximate the system response for any arbitrary combination of the parameters (i.e. unsimulated responses). To this aim, radial basis functions (RBF) have been adopted in [Ostrowski et al., 2005, Buljak and Maier, 2011]. In this work recourse is made to a kriging metamodel as an alternative for RBF as several studies have shown better performance of kriging metamodelling in terms of accuracy and robustness when dealing with nonlinear behaviour [Manzoni et al., 2012, Jin et al., 2003, Costa et al., 1999].

8.4 Kriging metamodel

The idea behind the MOR introduced earlier is the assumption that the behaviour of a system can be well reproduced by a small number of dominant (prevailing) POMs. To this aim, the POD finds the optimum modes keeping the projection error as low as possible (see Eq. (8.3)). However, to use such method for a parametric MOR, we need to establish the nonlinear relationship not only between the selected training parameter vectors and the corresponding snapshots, but also between the arbitrary parameters and the unsimulated responses. Kriging metamodelling offers a suitable technique for such purpose.

Kriging metamodelling belongs to the family of surrogate models [Viana et al., 2013]. These techniques provide an approximation of the input/output map only, by fitting a set of data/solutions which are usually obtained from numerical simulations. A plethora of different surrogate models is available. The most commonly used ones are based on response surface methods or polynomial regression [Box et al., 1978], radial basis function [Hardy, 1971], neural networks [Ting et al., 2010], polynomial chaos expansions [Ghanem and Spanos, 2003], or kriging [Sacks et al., 1989a]. These methods are popular in applications in which computational burden becomes prohibitively large for the engineering problems, where numerous and large-scale simulations are required, e.g. optimization algorithms or reliability estimation simulations. For more comprehensive lists of such methods and their applications the reader may refer to [Razavi et al., 2012, Wang and Shan,

2007, Simpson et al., 2001].

In the jargon of computer experimentation, we aim at substituting a computationally expensive model called *simulator* (e.g. FE modelling) by an *emulator*. The emulator shares the same input and output spaces of the simulator. Among different alternatives for surrogate modelling mentioned above, a kriging method has been chosen in this work due its accuracy, robustness with small training data and capability of uncertainty prediction [Simpson et al., 2001, Laurenceau and Sagaut, 2008].

Kriging is a particular emulator that provides a probabilistic response $\hat{Y}(\boldsymbol{x})$ whose variance or spread depends on the quantity of the available knowledge (simulator results); how many sets of input/output are provided to construct the emulator. The uncertainty prediction in this method is due to a lack of knowledge at the specific input parameter $\boldsymbol{x}$; therefore, it is purely epistemic rather than aleatory [Dubourg et al., 2011][1]. This property of kriging can be used as an error estimation tool in the prediction process.

Given the relationship $\mathscr{M}$ between the input $\boldsymbol{x}$ and the output scalar[2] y, kriging assumes that the output $y \equiv \mathscr{M}(\boldsymbol{x})$ is a sample path from a Gaussian process Y which needs to be characterized, i.e. its mean and autocovariance functions are unknown. This will be done by using the knowledge of model response (snapshots) $\{y_i = \mathscr{M}(\boldsymbol{x}_i), i = 1, ..., n\}$ evaluated at the experimental design points $\boldsymbol{x} = [\boldsymbol{x}_1, \boldsymbol{x}_2, ..., \boldsymbol{x}_n]$. The so-called *universal kriging* model assumes that the Gaussian process has an autocovariance function and is centered around a regression model (also known as trend) [Dubourg et al., 2011]

$$Y(\boldsymbol{x}) = \sum_{i=1}^{s} \beta_i f_i(\boldsymbol{x}) + Z(\boldsymbol{x}) = \boldsymbol{f}^{\mathrm{T}} \boldsymbol{\beta} + Z(\boldsymbol{x}) \tag{8.13}$$

where $\boldsymbol{f}^{\mathrm{T}} = [f_1(\boldsymbol{x}), ..., f_s(\boldsymbol{x})]$ are basis functions and $\boldsymbol{\beta} = [\beta_1, ..., \beta_s]^{\mathrm{T}}$ are regression

[1] This distinction between aleatory and epistemic is basically determined by our modelling choices and availability of uncertainty characterization. The uncertainty should be categorized as epistemic if it can be evaluated using the existing models. On the other hand, the uncertainty should be categorized aleatory if this evaluation is not available. For more detailed discussion, the reader is referred to [Der Kiureghian and Ditlevsen, 2009].

[2] Kriging handles the output vector by its entries individually, and not as whole. In other words, each entry of output vector can be seen as a degree of freedom which is linked to the input vector through a functional relationship.

coefficients, and the number of regression functions s is assumed less than or equal to the number observations n to avoid the problem being under-determined (i.e. it does not lack equations to explain the unknowns). The second term is a Gaussian process with zero mean and covariance $C_Z = \sigma_Y^2 R(|\boldsymbol{x} - \boldsymbol{x}'|, \boldsymbol{\xi})$ with a variance σ_Y^2 and a set of parameters $\boldsymbol{\xi}$, where $\boldsymbol{x}$ and $\boldsymbol{x}'$ are two points in the parameter space. The way the data are represented by kriging is critically dependent on the type of the correlation function R. The parameters $\boldsymbol{\xi}$, $\boldsymbol{\beta}$ and σ_Y^2 will be then determined upon the choice of correlation and regression functions. The correlation function can be stated as the generalized exponential model [Sacks et al., 1989b]

$$R(|\boldsymbol{x} - \boldsymbol{x}'|, \boldsymbol{\xi}) = \exp[-\sum_{k=1}^{s} \xi_k |x_k - x_k'|^\gamma] \tag{8.14}$$

with $1 \leq \gamma \leq 2$. The function is called general as it can change shape: $\gamma = 1$ and $\gamma = 2$ yield the exponential and the Gaussian functions, respectively.

The Gaussian assumption states that the vector formed by the response of the simulator (true model) $\boldsymbol{Y}$ (i.e. rows of the snapshot matrix $\boldsymbol{U}$) and the emulator prediction $Y(\boldsymbol{x})$ are normally distributed:

$$\left\{ \begin{array}{c} \boldsymbol{Y} \\ Y(\boldsymbol{x}) \end{array} \right\} \sim \mathbb{N} \left(\left\{ \begin{array}{c} \boldsymbol{F\beta} \\ \boldsymbol{f}^{\mathrm{T}}(\boldsymbol{x})\boldsymbol{\beta} \end{array} \right\}, \sigma_Y^2 \left\{ \begin{array}{cc} \boldsymbol{R} & \boldsymbol{r}(\boldsymbol{x}) \\ \boldsymbol{r}(\boldsymbol{x})^{\mathrm{T}} & 1 \end{array} \right\} \right) \tag{8.15}$$

where $\boldsymbol{F}$ with its generic terms $\{F_{ij} = f_j(\boldsymbol{x_i}), i = 1, ..., n, j = 1, ..., s\}$ and the correlation matrix $\boldsymbol{R}$ with its terms $\{R_{ij} = R(\boldsymbol{x}_i, \boldsymbol{x}_j; \boldsymbol{\xi}), i, j = 1, ..., n\}$ are defined with respect to the assumed statistics of the Gaussian process. Similarly, $\boldsymbol{r}(\boldsymbol{x})$ is the vector of cross-correlations between the observation points and the desired prediction point, $\{r_i(\boldsymbol{x}) = R(\boldsymbol{x}, \boldsymbol{x}_i; \boldsymbol{\xi}), i = 1, ..., n\}$.

Consequently, the mean and variance of the conditional distribution of $\hat{Y}(\boldsymbol{x}) = Y(\boldsymbol{x}) \mid \boldsymbol{Y}$ (also known as mean and variance of the kriging predictor), which is also Gaussian [Dubourg et al., 2011], can be calculated:

$$\mu_{\hat{Y}}(\boldsymbol{x}) = \boldsymbol{f}^{\mathrm{T}}(\boldsymbol{x})\hat{\boldsymbol{\beta}} + \boldsymbol{r}(\boldsymbol{x})^{\mathrm{T}} \boldsymbol{R}^{-1} (\boldsymbol{Y} - \boldsymbol{F}\hat{\boldsymbol{\beta}}) \tag{8.16}$$

$$\sigma^2_{\hat{Y}}(\boldsymbol{x}) = \sigma^2_Y \left(1 - \boldsymbol{r}(\boldsymbol{x})^{\mathrm{T}}\boldsymbol{R}^{-1}\boldsymbol{r}(\boldsymbol{x}) + \boldsymbol{q}(\boldsymbol{x})^{\mathrm{T}}(\boldsymbol{F}^{\mathrm{T}}\boldsymbol{R}^{-1}\boldsymbol{F})^{-1}\boldsymbol{q}(\boldsymbol{x})\right) \tag{8.17}$$

where

$$\hat{\boldsymbol{\beta}} = (\boldsymbol{F}^{\mathrm{T}}\boldsymbol{R}^{-1}\boldsymbol{F})^{-1}\boldsymbol{F}^{\mathrm{T}}\boldsymbol{R}^{-1}\boldsymbol{Y} \tag{8.18}$$

is the generalized least squares solution (with respect to $\boldsymbol{R}$) for the regression problem

$$\boldsymbol{F}\hat{\boldsymbol{\beta}} \simeq \boldsymbol{Y} \tag{8.19}$$

and we introduced

$$\boldsymbol{q}(\boldsymbol{x}) = \boldsymbol{F}^{\mathrm{T}}\boldsymbol{R}^{-1}\boldsymbol{r}(\boldsymbol{x}) - \boldsymbol{f}(\boldsymbol{x}) \tag{8.20}$$

To obtain the kriging model parameters in practice, the regression and correlation models need to be chosen and then these parameters can be determined using common available statistical inference techniques, such as the maximum likelihood estimation (MLE). Based on this technique, given the regression model $\boldsymbol{f}$ and correlation model $\boldsymbol{R}$, the likelihood of the simulated data can be calculated with respect to the unknown parameters, σ^2_Y, $\hat{\boldsymbol{\beta}}$ and $\boldsymbol{\xi}$. Eq. (8.18) holds for calculating $\hat{\boldsymbol{\beta}}$, and σ^2_Y in Eq. (8.17) can be evaluated analytically [Santner et al., 2013] as

$$\sigma^2_Y = \sigma^2_Y(\boldsymbol{\xi}) = \frac{1}{n}\left(\boldsymbol{Y} - \boldsymbol{F}\hat{\boldsymbol{\beta}}\right)^{\mathrm{T}}\boldsymbol{R}^{-1}\left(\boldsymbol{Y} - \boldsymbol{F}\hat{\boldsymbol{\beta}}\right) \tag{8.21}$$

The optimal values of $\boldsymbol{\xi}$ can be instead obtained by minimizing the negative log-likelihood function as

$$\boldsymbol{\xi} = \arg\min\left(-\log L(\boldsymbol{Y}|\hat{\boldsymbol{\beta}}, \sigma^2_Y, \boldsymbol{\xi})\right) \tag{8.22}$$

where $L(\boldsymbol{Y}|\hat{\boldsymbol{\beta}}, \sigma^2_Y, \boldsymbol{\xi})$ is the likelihood of observations gathered in $\boldsymbol{Y} = \{\mathscr{M}(\boldsymbol{x}_1), \mathscr{M}(\boldsymbol{x}_2), ..., \mathscr{M}(\boldsymbol{x}_n)\}^{\mathrm{T}}$. Since $\boldsymbol{Y}$ is assumed to be realization of a Gaussian process (recall basic kriging assumption), the minimization problem in Eq. (8.22) can be written as following

$$\boldsymbol{\xi} = \arg\min \left(\frac{1}{2} \log(\det(\boldsymbol{R})) + \frac{n}{2} \log(2\pi\sigma_{\hat{Y}}^2) + \frac{n}{2} \right) \tag{8.23}$$

Several kriging softwares are available to the research community such as 'PErK' [Santner et al., 2013], 'UQLab' [Marelli and Sudret, 2014] and 'DACE' [Lophaven et al., 2002]. In this work, we adopt the latter to derive metamodels $\mathscr{M}_K$ for the relevant coefficients of POD rather than directly for the response (i.e. $C - V$ curves in the MEMS devices problem, for instance) of a high fidelity model (simulator). Accordingly, the constructing the kriging model can be done as many times as the number of POMs kept in the POD method, only, and not as the number of the data points of the response (i.e. $C - V$ data points). In the next section, it is shown how POD and kriging can form a parametric model order reduction.

8.5 POD-kriging method for model order reduction

In Section 8.3, the POD method is introduced to construct the optimal orthogonal bases to be used for approximation of system responses stored in the snapshot matrix. This matrix can be then properly approximated through Eqs. (8.12) and (8.7). The order of reduction depends on the level of correlation between the vectors of the snapshot matrix. If a high level of correlation is present among the responses, the snapshot matrix can be approximated by a set of few POMs.

However, the final goal is to obtain a parametric MOR, i.e. a reduced model that can emulate the system response for any arbitrary set of input (belonging to the parameter domain) and not only the ones used for constructing it. If we assume that the snapshot matrix is collecting the most important ingredients of all possible responses, then we only need to establish the relationship between the reduced vector of coefficients $\hat{\boldsymbol{a}}$ and the input parameters of the system $\boldsymbol{x}$:

$$\boldsymbol{u}(\boldsymbol{x}) \approx \hat{\boldsymbol{u}}(\boldsymbol{x}) = \hat{\boldsymbol{\Phi}}\hat{\boldsymbol{a}}(\boldsymbol{x}) \tag{8.24}$$

This can be properly done using the introduced kriging surrogate. Exploiting the same simulated responses collected in the snapshot matrix $\boldsymbol{U}$, the kriging model $\mathscr{M}_K$ can be constructed to approximate the elements of the coefficient vector,

which reads

$$\hat{\boldsymbol{a}}(\boldsymbol{x}) \approx \tilde{\boldsymbol{a}}(\boldsymbol{x}) = [\mathscr{M}_{K_1}(\boldsymbol{x}), \mathscr{M}_{K_2}(\boldsymbol{x}), ..., \mathscr{M}_{K_r}(\boldsymbol{x})]^{\mathrm{T}} = \bar{\mathscr{M}}_K(\boldsymbol{x}) \tag{8.25}$$

So, at the final assembling of the two approximation stages, POD-kriging, a parametric reduced model of the system can be obtained as

$$\boldsymbol{u}(\boldsymbol{x}) \approx \hat{\boldsymbol{\Phi}} \bar{\mathscr{M}}_K(\boldsymbol{x}) \tag{8.26}$$

This training process is done once-for-all. The operations that it involves are accordingly summarized by the flow-chart presented in Figure 8.1. It is worth noting that the efficiency of this method is critically dependent on the degree of representativeness of the snapshot matrix, i.e. how much of the physical characteristics of the system are captured with the best possible accuracy. Since the training stage of POD-kriging is computationally expensive, a thoughtful choice of the training input parameters (sampling) is necessary to avoid the excessive number of simulations and to ensure the accuracy of the reduced model. In the next section, we discuss the alternative methods for the sampling stage and we adopt an efficient strategy to be coupled with POD-kriging.

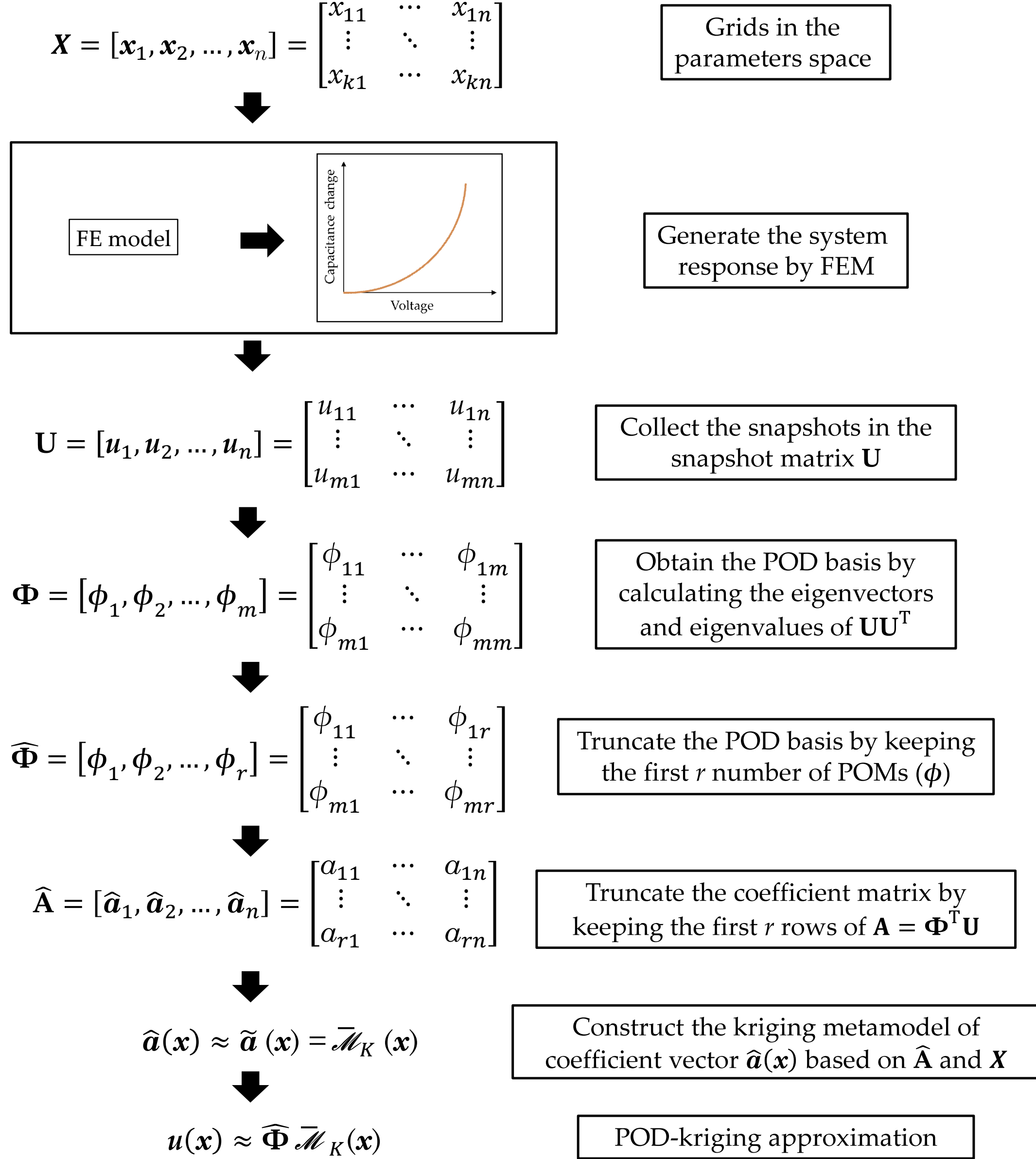

Figure 8.1: Flow chart of operations to be performed in a POD-kriging procedure with k number of unknown parameters, n number of snapshot (FE simulation based on predefined parameters) and m number of output quantities from FE model (discretized response curve).

8.5.1 Sampling strategy

The POD and the kriging methods both require a set of system responses for the training stage. In other words, they need a set of the outputs of the FE model (snapshots) which are the data points forming the $C-V$ curves in the present problem. Each of these snapshots ($C-V$ curves) is corresponding to a set of given model parameters (collected in $\boldsymbol{x}$). This brings two key points: i) the choice of the snapshots in the parameter space, and ii) the number of proper orthogonal modes to be kept. The latter was discussed earlier, but the former is a sampling issue. Generally, the sampling methods can be divided into two groups depending on the presence of prior knowledge on the behaviour of the function to be sampled. In the case that the function behaviour with respect to the parameters variations is well studied and known, a preferred distribution pattern can be chosen; based on the characteristics of the function, providing denser distribution of sampling points (snapshots) at the the zones of extreme nonlinearity and vice versa, similar to [Bolzon and Buljak, 2011]. The alternative, i.e. the absence of such knowledge, is often the case for high-dimensional problems (i.e. several co-existing uncertain parameters). This issue is addressed in the literature as a design of computer experiments problem. The first intuitive sampling method is the uniform sampling. Despite its generality and simplicity, this technique is practically inapplicable when the problem dimension is high since the dimension is the exponent of the number of points per space direction (this behaviour is often called the curse of dimensionality). The random sampling method can be an alternative, but it also faces difficulties such as low efficiency at higher dimensions or sampling points close to one another which does not add valuable information. A popular method is the Latin Hypercube sampling [McKay et al., 2000], which offers an optimum space filling quality for a predefined number of samples. This sampling strategy is an *a priori* one and the number of sampling points should be set at the beginning. That means one should know from the beginning that how many sampling points can be adequate to provide an informative snapshots for the POD-kriging. In the case that the initial sampling is poor, enriching the sample collection by adding more samples violates the optimum space filling condition of Latin Hypercube method. The enriching stage causes problems for some other

methods, like centroidal Voronoi tessellations [Du et al., 1999], where a revision of an initial distribution of points will be required. Quasi-Monte Carlo methods such Halton [Halton, 1960] or Sobol [Sobol, 1967] are other popular sampling techniques which sequentially generate new sample points. They are very efficient on low-dimensionality problems but need special treatments for dimensions higher than ten [Laurenceau and Sagaut, 2008]. There is another class of techniques which is adaptive and sequential, such as the greedy methods [Maday and Stamm, 2013, Haasdonk, 2013, Leblond and Sigrist, 2016] or the quad-tree-like resampling method introduced in [Margheri and Sagaut, 2016, Braconnier et al., 2011]. They use the information provided by the previous samples (which are selected by uniform grid or Latin Hypercube, for instance) to locate incrementally the new sample points according to a criterion which is usually related to the discrepancy between the output of the reduced and the original model at that point. Consequently, they are numerically more complicated to be implemented compared to the Latin Hypercube or the random distribution.

In this work, the sampling is done using a predefined set of points, based on the sparse grid methods of the Smolyak algorithm [Smolyak, 1963], unlike the Monte Carlo approach where the points are chosen in a statistical manner. The use of sparse grids has been precedented for kriging sampling in [Margheri and Sagaut, 2014, Axerio et al., 2010]. Since this approach involves only predefined points in the parameters space, its coupling with a high fidelity model is straight-forward and only requires simulations at those predefined parameters. The Smolyak algorithm is the extension of the univariate interpolation formula to higher dimensions using the minimal number of support points. The sparse grid methods are in fact a special discretization technique, which allows to cope with the curse of dimensionality, so that, by increasing the dimension of the problem, the number of sampling points does not increase according to a power law. Another important feature of this technique is rooted in its hierarchical structure [Bank et al., 1988]: the new sample points are inserted to the initial sample distribution without rearrangement of existing points. Therefore, the existing FE solutions can be added if new points are needed to improve the sampling process. This enriching step is often necessary because the initial set of sampling points may not be adequate and more sampling points should be added to the previous collection.

We use the sequences of two types of sparse grids, Clenshaw-Curtis and Chebyshev [Barthelmann et al., 2000], from the toolbox provided by [Klimke, 2007] for sampling the functions and training the POD-kriging. Depending on the error between the generated model and the FE model, different levels of the sparse grids can be sequentially adopted. Examples of this type of grids in the parameter space for two and three dimensional problems are plotted in Fig. 8.2 and Fig. 8.3 up to sequence level 5. Table 8.1 gathers the growing number of sampling points of this strategy as the dimension of the problem expands. It is important to note that the increase rate of points is not exponential as it is the case for uniform sampling. This sequential method is effective for smooth functions with moderate local gradients. If the considered problem features sharp gradients or strong discontinuities, an adaptive method can be employed to search samples more thoroughly from those regions.

Table 8.1: Number of sampling points by Smolyak algorithm at different dimensions.

	design space dimension							
sampling order	1	2	3	4	5	6	7	8
1	3	5	7	9	11	13	15	17
2	5	13	25	41	61	61	113	145
3	9	29	69	137	241	389	589	849
4	17	65	177	401	801	1457	2465	3937
5	33	145	441	1105	2433	4865	9017	15713

8.6 Transitional Markov chain Monte Carlo simulation

In the previous chapter, we adopted a genetic algorithm to identify the unknown parameters of the model which belongs to the family of deterministic approaches. These approaches usually result in a set of crisp parameter estimates (i.e. dealing with the unknown parameters as deterministic variables); in some cases a covariance matrix is also extracted only to state a confidence interval or error

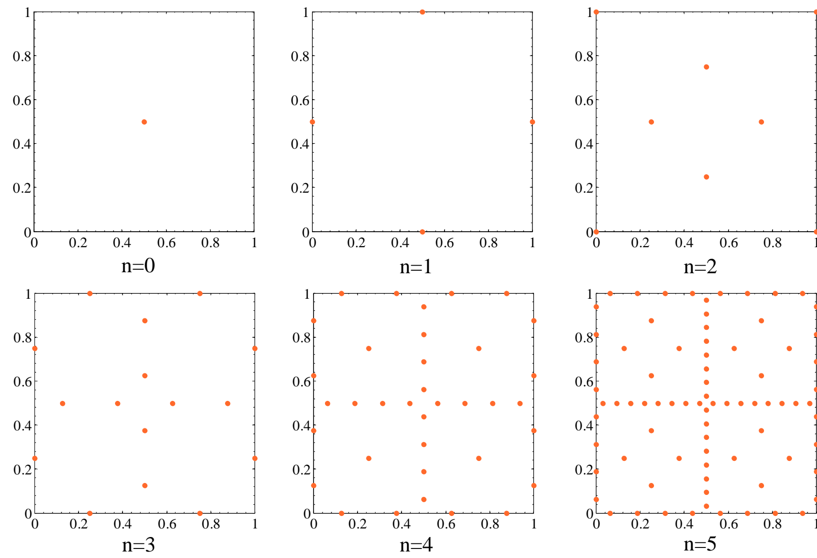

(a)

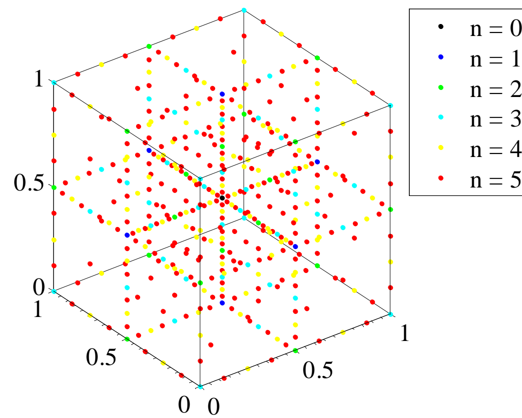

(b)

Figure 8.2: Ilustration of Clenshaw-Crutis sample points distribution in the case (**a**) of two dimensional, and (**b**) of three dimensional problem.

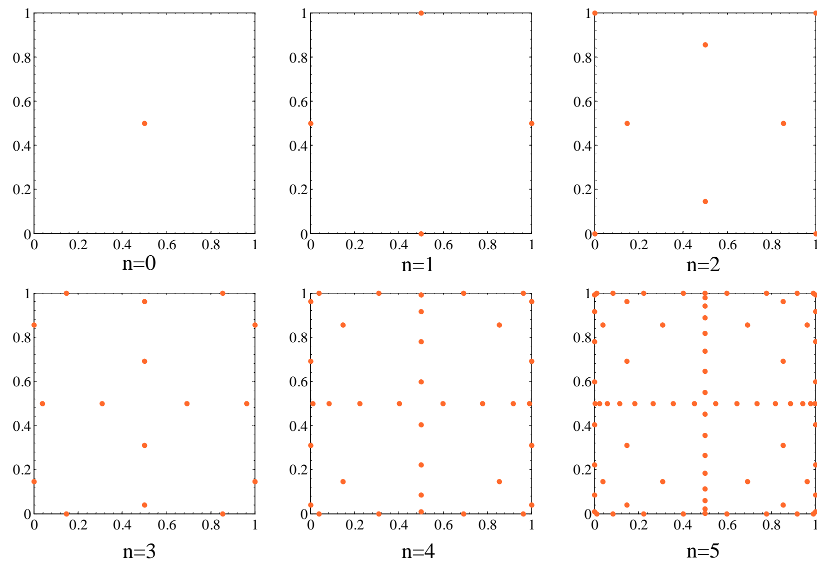

(a)

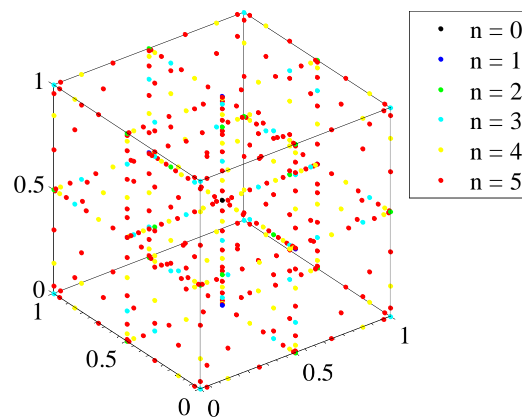

(b)

Figure 8.3: Ilustration of Chebyshev sample points distribution in the case (**a**) of two dimensional, and (**b**) of three dimensional problem.

bars on the estimated values. Nonetheless, in the case that predictions of the model are required for unseen inputs, the predicted outputs are computed using the parameters only. Such approaches do not consider that the available data are usually contaminated by the measurement noise and just one prescribed model cannot accommodate all the measurements, but different model classes need to be associated. It must be noted that, the particle filter introduced in Chapter 6 is able to address these issues as an on-line method. But when the experimental observations (measurements) are available prior to the parameter estimation process, an off-line method is more advantageous (see Chapter 6). So in what follows, another approach from the family of Bayesian methods is adopted.

In a Bayesian framework, the parameters are viewed as random variables rather than deterministic values and can be described by probability distributions. These distributions can then be regarded as one's degree of belief about the value of a certain parameter. The system identification in the Bayesian (like any other) approach deals with a potentially ill-posed problem, and finding the global optimal solutions for the model parameters can be challenging. In [Beck and Katafygiotis, 1998], a study of an unidentifiable case of model updating problem was carried out and an asymptotic approximation method was successfully suggested to derive the continuum of the optimal model parameters (parameter manifolds that are unidentifiable). This approach is not robust when the model parameters are not very peaked. Besides, stochastic simulation methods can handle more general cases than the asymptotic approximation method. However, application of many of these methods to the practical Bayesian inverse problems is often inefficient, for instance, importance sampling is not efficient for high-dimensional problems [Au and Beck, 2003]. To this aim, another available stochastic method is the Metropolis-Hastings (MH) algorithm [Metropolis et al., 1953, Hastings, 1970]. This algorithm is a method to obtain sequences of random samples (Markov chain samples) from a target PDF. In the MH method, the PDF of a Markov chain sample simulated at th i-th Markov step tends to the target PDF as $i \to \inf$. However, application of MH algorithm is limited if the target PDF is multimodal or the problem is high dimensional [Ching and Chen, 2007].

Beck and Au [Beck and Au, 2002] proposed an alternative method to solve the Bayesian problem, regardless of whether the class of selected models is identifiable

or not. They introduced a Markov chain Monte Carlo (MCMC) method, avoiding direct application of the MH algorithm. Their method mixes the MH algorithm with a concept similar to that used in simulated annealing[1] (which is originally proposed as a probabilistic optimization method [Kirkpatrick, 1984], but can be used to sample from multimodal PDFs as well). The main idea is to sample not directly from the target PDF but successively from a series of simpler intermediate PDFs, in order to adapt to the region of probability concentration of the target PDF. Using this method, it is shown that Markov chain samples populate the regions of concentrations in a probabilistically correct manner [Beck and Au, 2002]; nevertheless, it becomes inefficient for high-dimensional problems.

This method was further enhanced in Transitional MCMC or TMCMC [Ching and Chen, 2007]. TMCMC is applicable for sampling complex posterior distributions, i.e. very peaked, flat, multi-modal and high-dimensionality PDFs. This method is also capable of evaluating the evidence for the assumed model class, which is the key point for the Bayesian model selection [Green and Worden, 2015]. Therefore, TMCMC belongs to the family of algorithms that can be used to address two levels of inference at the same time: parameter estimation and model class selection. Other examples of algorithms for two levels inference are: Nested Sampling [Skilling, 2004], Reversible jump Markov chain Monte Carlo [Green, 1995] and Variational Bayesian inference [Ghahramani et al., 1999]. Another advantage of The TMCMC algorithm is that it can be properly handled by parallel processors [Angelikopoulos et al., 2012]. Given these features, TMCMC has received a huge attention by the engineering community in different applications [Goller et al., 2011, Green et al., 2015, Lam et al., 2015, Ortiz et al., 2015, Ching and Wang, 2016]. In this work, we couple the TMCMC with the POD-kriging reduced model for parameter estimation purposes.

Though the Bayesian framework is introduced in Chapter 6, it is appropriate to define the problem once more. Let $\boldsymbol{x} \in \mathbb{R}^{n_x}$ denote the unknown parameters of a model class M of an engineering system, and D be the measured data or the set of observations of that system. The main idea of a Bayesian approach is that,

[1] In the jargon of sampling the posterior parameter distribution, simulated annealing has influenced a number of algorithms: Simulated Tempering [Celeux et al., 2000, Marinari and Parisi, 1992], Exchanged Monte Carlo [Hukushima and Nemoto, 1996], TMCMC [Ching and Chen, 2007] and (smooth) Data Annealing [Green, 2015b, Green, 2015a].

by sequential application of Bayes' rule, one can firstly sample properly from the posterior distribution of $\boldsymbol{x}$ conditioned on D and, secondly, assess the probability of the model structure M conditioned similarly, using

$$p(\boldsymbol{x}|D, M) = \frac{p(D|\boldsymbol{x}, M)p(\boldsymbol{x}|M)}{p(D|M)} \tag{8.27}$$

and

$$p(M|D) = \frac{p(D|M)p(M)}{p(D)} \tag{8.28}$$

where

$$p(D|M) = \int p(D|M)p(M)\, d\boldsymbol{x} \tag{8.29}$$

is the same normalizing constant $1/\varsigma$ in Eq. (6.4), which ensures that integral of Eq. (8.27) is unitary. This is called evidence of M also known as marginal likelihood and can be used for selecting a model among some proposals. $p(\boldsymbol{x}|M)$ represents the *a priori* PDF of $\boldsymbol{x}$ and $p(D|\boldsymbol{x}, M)$ is the likelihood, which describes the probability of witnessing the data D given the model class M with parameters $\boldsymbol{x}$. The *a priori* PDF of $\boldsymbol{x}$ represents one's knowledge of the parameters before an observation is carried out. Basically, Eq. (8.27) converts this *a priori* knowledge into a posterior density having observed the data D.

The reconstruction of the posterior parameter distribution is usually done by a sampling performed by MCMC algorithms. The MCMC involves a random walk (i.e. succession of random steps) through the probability distribution, favoring values with higher probability. Repeating this sampling strategy, every point in the parameter space is hit with a frequency proportional to its probability, i.e. the stationary distribution of Markov chain is equal to (or at least proportional to) the target distribution [Green and Worden, 2015]. As mentioned earlier, the MH algorithm is not efficient at drawing samples from high-dimensionality parameter space when all the regions of high probability content have to be covered. The algorithm by Beck and Au [Beck and Au, 2002] proposes a gradual updating of the model by using the MH algorithm to sample from a sequence of target PDFs. Each target PDF is a posterior PDF obtained by an increasing fraction of available data to the inference. This annealing feature helps the target PDF to gradually

converge from the broad *a priori* PDF to the final concentrated posterior PDF [Muto and Beck, 2008]. Rather than using only a part of the data, the TMCMC takes advantage of a sequence of intermediate PDFs using the entire data set.

The TMCMC algorithm, by circumventing the need to evaluate the marginal likelihood stated in Eq. (8.29) (like any MCMC method), relies on sampling from a sequence of N non-normalized intermediate PDFs

$$p_n(\boldsymbol{x}) = p(D|\boldsymbol{x}, M)^{\beta_n} p(\boldsymbol{x}|M), \quad n = 0, ..., N,\ 0 = \beta_0 < \beta_1 < ... < \beta_N = 1 \quad (8.30)$$

where the tempering parameter[1] β_n monotonically increases with n. Consider N_s samples taken from each intermediate PDF $p_n(\boldsymbol{x})$ (or at initiation stage, taken from the $p(\boldsymbol{x}|M)$), which are denoted as $\boldsymbol{x}_k^{(n)}, k = 1, ..., N_s$. A technique similar to importance sampling to generate the next distribution $p_{n+1}(\boldsymbol{x})$ is then used, by calculating the importance (or plausibility) weights and normalized importance weights of each sample with

$$w(\boldsymbol{x}_k^{(n)}) = \frac{p_{n+1}(\boldsymbol{x}_k^{(n)})}{p_n(\boldsymbol{x}_k^{(n)})} = p(D|\boldsymbol{x}_k^{(n)}, M)^{\beta_{n+1}-\beta_n} \quad (8.31)$$

and

$$\hat{w}(\boldsymbol{x}_k^{(n)}) = \frac{w(\boldsymbol{x}_k^{(m)})}{\sum_{k}^{N_s} w(\boldsymbol{x}_k^{(n)})} \quad (8.32)$$

respectively. To avoid the degeneracy problem (see Section 6.3), the TMCMC considers each re-sampled value $\boldsymbol{x}_k^{(n)}$ as the starting point of a Markov chain evolving with accordance to the MH algorithm. The normalized importance weight calculated in Eq. (8.32) determines the Markov chain growth. Once the Markov chains have generated a sufficient number of samples from the intermediate target $p_n(\boldsymbol{x})$, the process is repeated until the samples from $p(\boldsymbol{x}|D, M)$ are produced.

In this work, the focus is on the first level of inference, i.e. sampling the model parameter distribution. We use the TMCMC algorithm developed in [Ching and Chen, 2007] whose algorithmic steps are the following.

[1] β_n is called tempering parameter due to the conceptual similarities between TMCMC and simulated annealing approach.

1. The first intermediate PDF $p_0(\boldsymbol{x})$ is defined as the prior PDF of parameters $p(\boldsymbol{x}|M)$. It is assumed to be in a form to be sampled to obtain $\boldsymbol{x}_k^{(0)}, k = 1, ..., N_s$.

2. The first value of tempering parameter is chosen, such that the coefficient of variation for $p(D|\boldsymbol{x}_k^{(0)}, M)^{\beta_1}, k = 1, ..., N_s$ is equal to a prescribed value.

3. The importance weights $w(\boldsymbol{x}_k^{(0)}) = p(D|\boldsymbol{x}_k^{(0)}, M)^{\beta_1}$ are calculated for N_s samples. Accordingly, the sample mean $\boldsymbol{\mu}^{(0)} = \sum_{k=1}^{N_s} w(\boldsymbol{x}_k^{(0)})\boldsymbol{x}_k^{(0)}$ is estimated.

4. Samples, $\boldsymbol{x}_k^{(1)}, k = 1, ..., N_s$ are generated using MH algorithm. This algorithm draws the k-th sample from a Markov chain that starts with a sample called leader, denoted by $\boldsymbol{x}_{leader}$ which is equal to one of the samples $\boldsymbol{x}_i^{(0)}, i = 1, ..., N_s$. The probability of $\boldsymbol{x}_{leader}$ to be $\boldsymbol{x}_i^{(0)}$ is in turn given by $w(\boldsymbol{x}_i^{(0)}/\sum_{j=1}^{N_s} w(\boldsymbol{x}_j^{(0)}))$. The MH algorithm is applied using a Gaussian proposal PDF centered at the current sample in i-th chain with the covariance matrix Σ_m, i.e. $\mathbb{N}(\boldsymbol{x}_i^{(0)}, c_m^2\Sigma_m)$. The covariance matrix is given by

$$\Sigma_m = \sum_{i}^{N_s} w(\boldsymbol{x}_i^{(0)})(\boldsymbol{x}_i^{(0)} - \boldsymbol{x}^{(0)})(\boldsymbol{x}_i^{(0)} - \boldsymbol{x}^{(0)})^{\mathrm{T}} \tag{8.33}$$

   where

$$\boldsymbol{x}^{(0)} = \sum_{j}^{N_s} w(\boldsymbol{x}_j^{(0)})\boldsymbol{x}_j^{(0)} / \sum_{l}^{N_s} w(\boldsymbol{x}_l^{(0)}) \tag{8.34}$$

   The c_m^2 is a user selected parameter scaling the covariance matrix and balance the potential for large MCMC moves with maintaining a reasonable rejection rate.

5. Step 2 through 4 are repeated until N where $\beta_N = 1$ and full available data is plugged into the posterior distribution update.

The TMCMC algorithm can be used to obtain the unknown parameters of the model based on the measurements (observations). These parameters can be formulated in a FE model of the physical system. However, since the TMCMC

algorithm involves many simulations, adopting a time-consuming FE model is inapplicable, specially if the parameter estimation must be carried out several times. To this aim, recourse can be made to constructing a fast-computing, robust and accurate approximation the FE model using the earlier introduced POD-kriging method, allowing for unknown parameters to be incorporated.

8.7 POD-kriging TMCMC: Application to electromechanical problem

In this section, we adopt the POD-kriging method to drastically reduce the computation time of the numerical model developed in Chapter 4. This model is able to predict the electromechanical response (i.e. $C - V$ curves) of the test devices presented in Chapter 3. The reduction of the computation time is a preliminary step necessary for parameter estimation approaches such as the TMCMC, where a huge number of system responses needs to be evaluated varying the model parameters. In this case, a numerical model such as the FE model is completely inapplicable. For instance, the FE model of the test devices which can take up to 30 minutes of computation time (since the problem is multi-DOF and multi-physics, see Chapter 4) on a personal computer with an Intel®Core™i7 3.00 GHz processor, can be reduced to just few milliseconds[1] on the same computer using the POD-kriging method. Here, we use the TMCMC approach for estimating the parameters of a reduced model as a simple exemplary case to demonstrate the effectiveness of the proposed framework.

The FE model of the test device, similar to the analytical model in Chapter 6, considers the over-etch O and the Young's modulus E as the input parameters. It is worth noting that, based on the results of Chapter 6, the measured scattering cannot be explained simply by considering the variation of these two parameters. Even though this conclusion has been made using the analytical model, due to the analogies between the analytical and the FE model models (shown in Chapter 4), the conclusion is likely to hold true. However, we examine the application of the POD-kriging TMCMC using the numerical model considering these two

[1] The reduction in this context regards the emulating stage, rather than the training stage which is computationally time consuming.

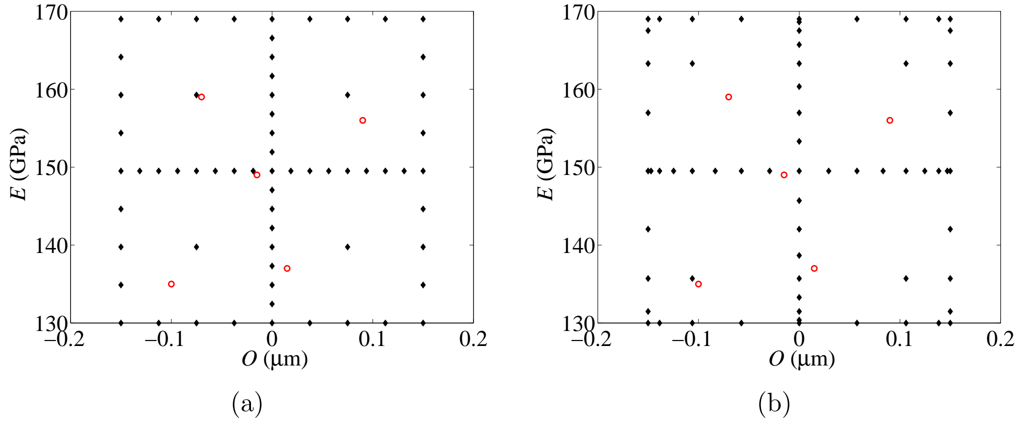

Figure 8.4: Ilustration of verification points (red circles) along the (**a**) Clenshaw-Crutis, and (**b**) Chebyshev sample points distribution (black dots).

parameters only, aiming at the exemplification of the framework more than to the actual device characterization.

The snapshot matrix for the POD-kriging reduction has been obtained through Clenshaw-Curtis and Chebyshev sparse grids up to level 4, which accounts for 65 simulations. The level of sparse grids is chosen based on a test on the accuracy constructed POD-kriging model. The response of the system for five extra sets of parameters (i.e. 5 sets of FE simulations), not exploited in training, are used for verification purposes; the POD-kriging output is compared with that provided by the corresponding FE direct analysis. Figure 8.4 illustrates these points in the parameter space sampled by the two types of sparse grids. These verification points are selected so that they explore different regions of the space while being different from the training points.

The comparison between the FEM output and that of the POD-kriging approach can be seen for the LL case in Figure 8.5. The two reduced models are obtained using 65 training simulations distributed according to Clenshaw-Curtis and Chebyshev sparse grids. As it can be seen, they perform well at reproducing the output of the FE model, at a much lower on-line[1] computational cost, on

[1] In the realm of MOR techniques, the training stage which involves the expensive FE simulations is often called off-line stage; the cheap calculation reproducing the response by the reduced model is instead called on-line stage. These two definitions should not be confused with the

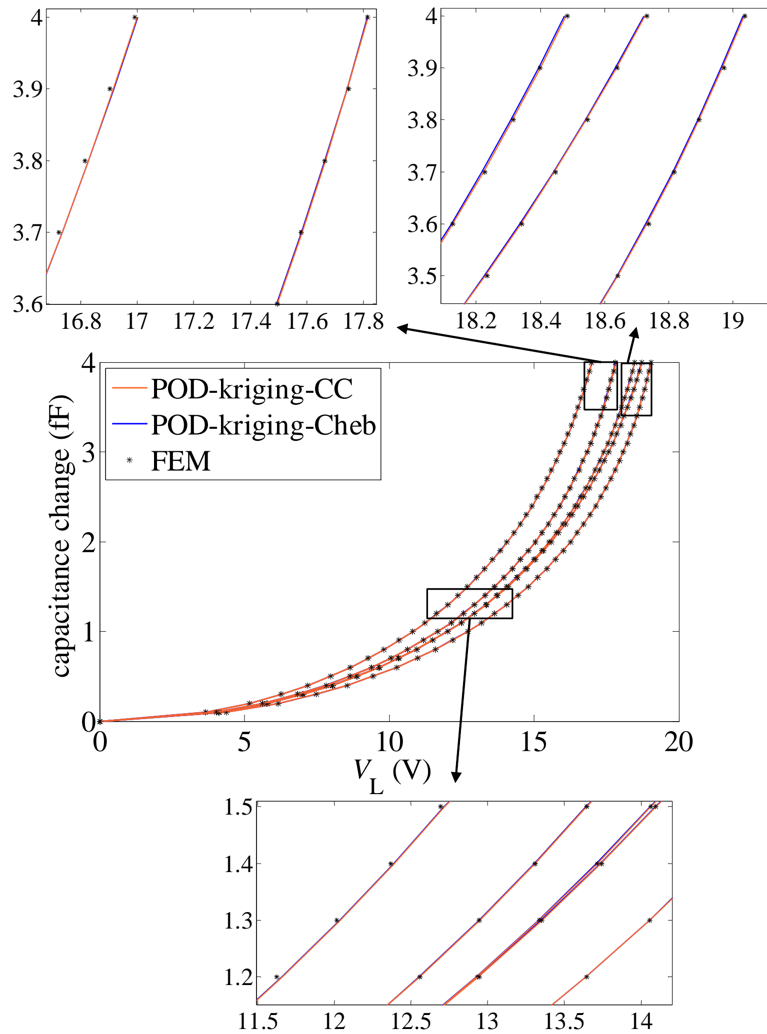

Figure 8.5: Comparison between the output of direct FE model and its POD-kriging approximation using two different sparse grids; Clenshaw-Curtis (CC) and Chebyshev (Cheb).

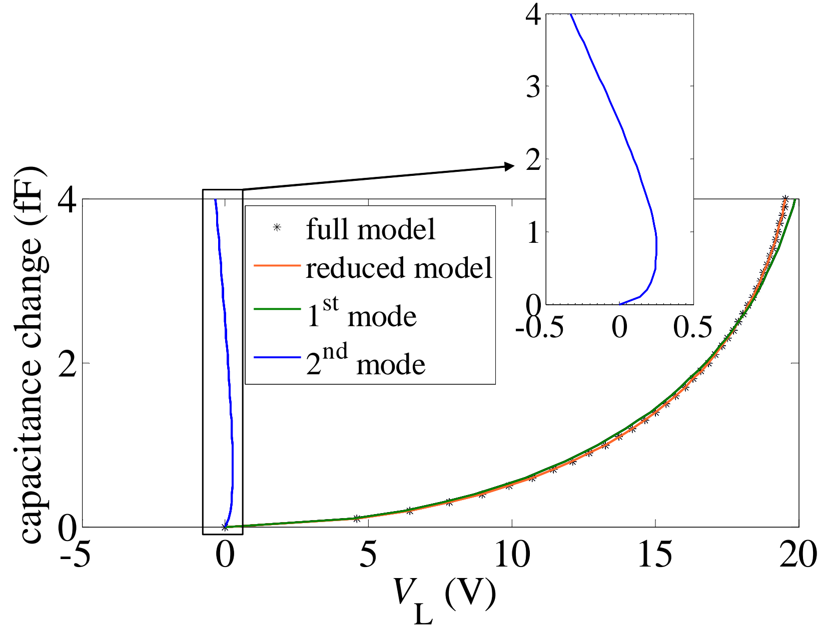

Figure 8.6: Comparison between a FE model output and its POD representation by the first two prevailing modes.

the order of few milliseconds. The maximum approximation error between the reduced models and FE model (i.e. the maximum relative error observed in the value of the capacitance change predicted by the reduced model with respect to the FE model output) is 0.08% and 0.29% for Clenshaw-Curtis and Chebyshev grids, respectively. Both grids perform well at sampling the parameter space; however, the Clenshaw-Curtis performs slightly better than the Chebyshev grids. It is worth mentioning that, this observation is limited to the present case and this verification must be carried out if a new application/problem is of concern.

Regarding the POD stage, the resulting bases matrix $\mathbf{\Phi}$ of the SVD is truncated by keeping only two first POMs. The truncation error, the ratio between the sum of the singular values of the kept POMs and the sum of all the singular values, for both the sparse grids is lower than 1%, which shows the high correlation between columns of the snapshot matrix, i.e. the system responses at varying

terms off-line/on-line in the jargon of system identification.

the two model parameters. This issue is illustrated in Figure 8.6, where one of the training FE simulations (whose parameters are $O = 0.15$ μm and $E = 169$ GPa) and its POD representation are compared. The two constituent modes of the POD representation are also presented; the importance of the first mode with respect to the second mode is visible. Adding extra POMs to this representation will not add useful information to reproduce the FE responses. Similar behaviour exists for other values of O and E. Thus, we consider, in all the following simulations, the first two POMs to be fed into the kriging algorithm with the training points distributed according to the Clenshaw-Curtis sparse grid method, without sacrificing the accuracy of the electromechanical response.

We construct the reduced model of the device response for the cases RR and LL, and we estimate the unknown parameters (e.g. O and E) based on one of the measurements reported in Chapter 3. We select specimen #2 (the same specimen whose parameter estimation is shown in Figure 6.4 and 6.5) and feed its two responses to the TMCMC algorithm featuring 10000 samples per each TMCMC stage. Thanks to the low computational effort associated to the reduced model, whole parameter estimation process by TMCMC takes up to 9 minutes on a personal computer with an Intel®Core™i7 3.00 GHz processor. The assumed distribution of the measurement noise is assigned Gaussian, whose covariance is defined by $\sigma_R^2 = \sigma_L^2 = 10^{-3}$ fF^2, similar to the analyses in Chapter 6. The *a priori* distribution of parameters is considered uniform and samples from the posterior distribution of the parameters are plotted in Figure 8.7(a) and 8.7(b) for RR and LL cases, respectively. The joint probability distribution of the estimated parameters is shown in 8.8(a) and 8.8(b) in more details along side with the parameters histograms. Comparing the prior and posterior distributions, it is evident how the samples cluster around the target region.

The joint probability of the parameters gives a complete statistical insight into the possible correlation between them which can be consistent with the measured data (i.e. larger values for O correspond to lower values for E and vice versa). As for reporting the inferred parameters, one might use the mean (or sometimes the median) of the output distributions as the “best” estimates and then the covariance would allow one to establish confidence intervals for them. However, mean and median can be particularly influenced by the presence of outliers and

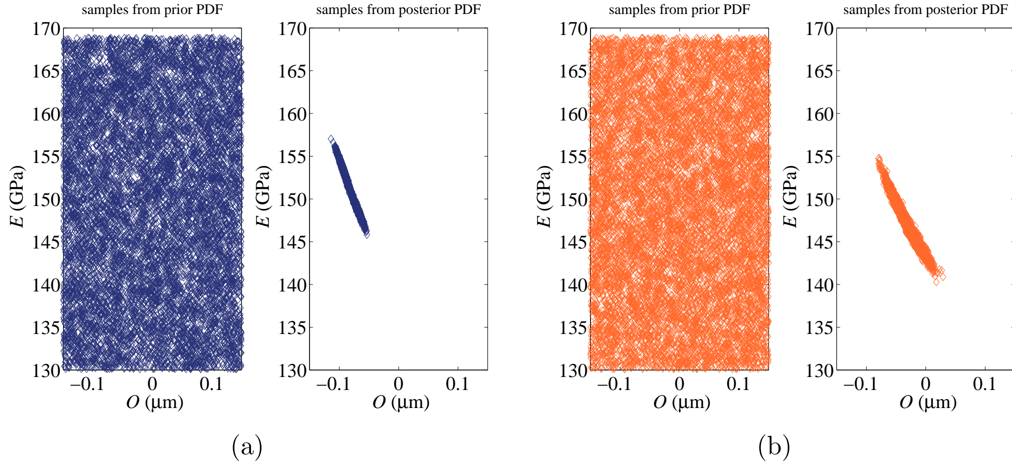

Figure 8.7: TMCMC samples generated from the prior (left hand side) and posterior (right hand side) PDF of (**a**) RR case, and (**b**) LL case for the specimen #2.

be entirely misleading in case of multi-modal or heavily skewed distributions. One might instead adopt the mode (which is the value at which a PDF is maximized, in other words, the value that appears most often in a set of data) of the posterior parameter distribution. Therefore, the estimates for the unknown parameters (in terms of the mode of the PDF) are [O = -0.09 μm, E = 153.3 GPa] and [O = -0.03 μm, E = 147.1 GPa], respectively from RR and LL measurements. In comparison to the estimations for the specimen #2 reported in Chapter 6, the present results show moderately smaller values for O and considerably higher values for E. The difference in the estimations of E can be mainly related to the assumption of perfect anchor in the analytical model used in the analyses of Chapter 6; therefore, the elasticity of anchor is reflected in the smaller values of E. The anchor elasticity can be easily taken into account by the FE model. The advantage of POD-kriging is that it allows to reduce the computational effort of such model so that it can be then plugged into the TMCMC method at an affordable computation effort and accuracy.

To see the effectiveness of the TMCMC approach, the measured response of specimen #2 is confronted in Figure 8.9(a) and 8.9(b) with the model response

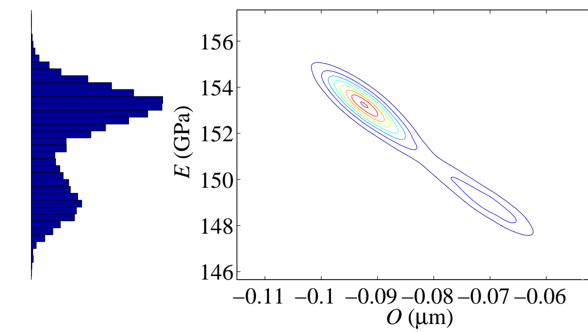

(a)

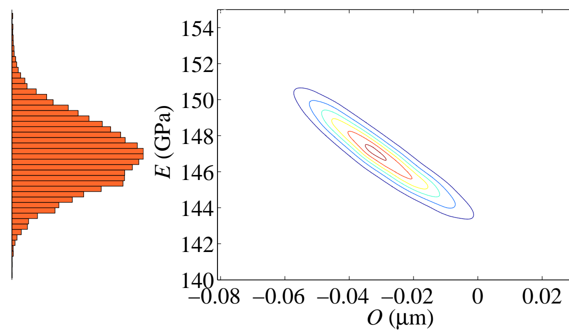

(b)

Figure 8.8: Contour plot of the posterior PDF and corresponding histograms of (**a**) RR case, and (**b**) LL case for the specimen #2.

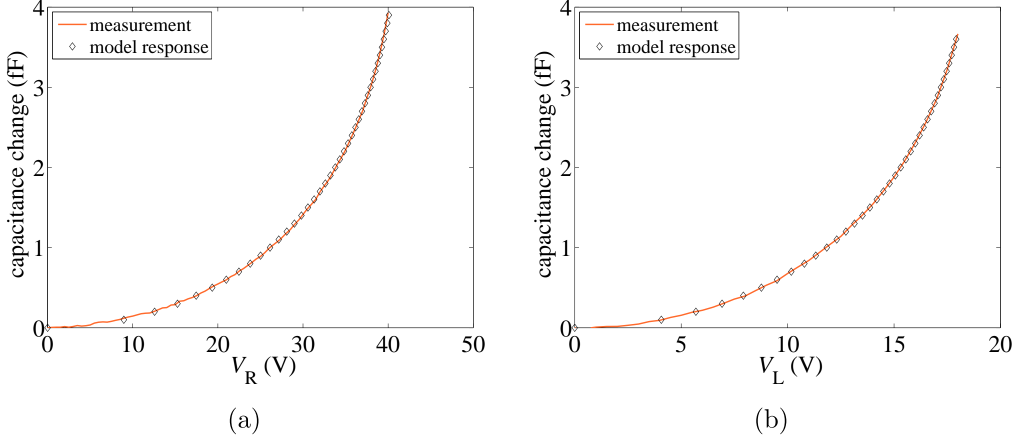

Figure 8.9: Comparison between the measured response of specimen #2 and model response using the estimated parameters by TMCMC for (**a**) RR case, and (**b**) LL case.

using the mode of the distributions. The estimated values can perfectly reproduce the measurements for both RR and LL cases. These graphs clearly show that the TMCMC algorithm using the POD-kriging reduction technique is able to infer the parameter sets based on the measured data.

Similar to Chapter 6, the results of the parameter estimation process is reported also for specimen #5, in Figure 8.10 and 8.11. It can be seen that the TMCMC has been again successful at sampling from the posterior PDFs and at providing the detailed joint probability distribution of the parameters. In the earlier study using analytical model and particle filtering (Chapter 6), the estimated parameters for this specimen have been non consistent; they have featured completely different values depending on the actuation type (i.e. lateral or rotational). Using the POD-kriging TMCMC the estimated parameters (in terms of the mode of the PDFs) are: [O = -0.12μm, E = 153.1 GPa] and [O = -0.04μm, E = 161.9 GPa], respectively from RR and LL measurements. These estimations are more consistent with each other compared to the results of Chapter 6. Confronting the experimentally obtained $C - V$ curves for this specimen and those calculated by the reduced model using these sets of parameters in Figure 8.12, it can be seen that the TMCMC method has been successful at inferring parameters

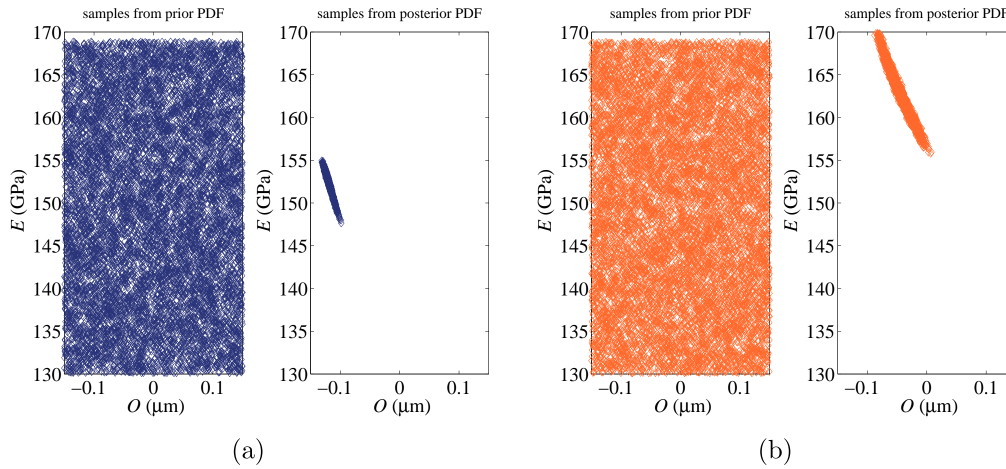

Figure 8.10: TMCMC samples generated from the prior (left hand side) and posterior (right hand side) PDF of (**a**) RR case, and (**b**) LL case for the specimen #5.

to reproduce the measurements.

It should be noted that the posterior distributions of RR and LL case do not perfectly superpose (for both specimens); this was expected since the FE model is not a perfect representation of the actual physical system; therefore, it is not capable at explaining measured scatterings appropriately. Based on the findings of Chapter 7, it is expected that by enhancing the FE model through allowing for other parameters to vary (the rotation offset, in particular), the parameter estimation procedure yields more consistent results, i.e. the posterior distributions of RR and LL get closer to one another.

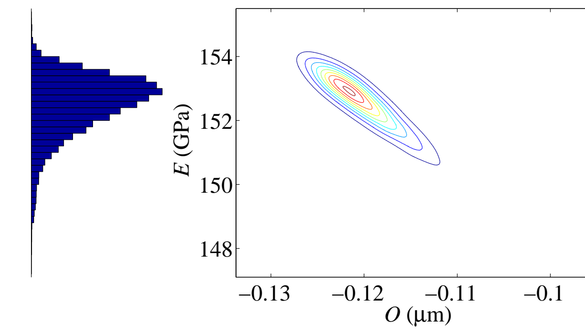

(a)

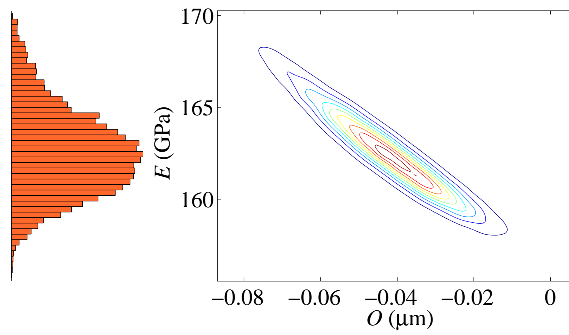

(b)

Figure 8.11: Contour plot of the posterior PDF and corresponding histograms of (**a**) RR case, and (**b**) LL case for the specimen #5.

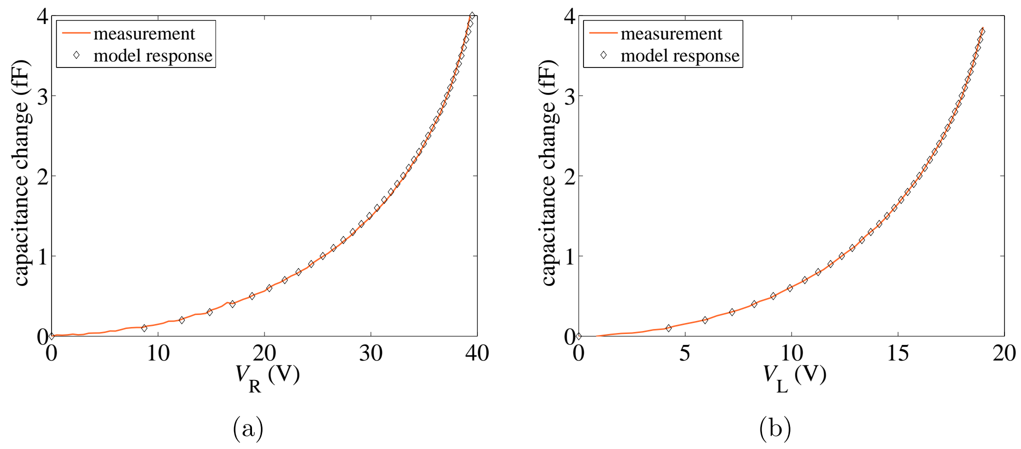

Figure 8.12: Comparison between the measured response of specimen #5 and model response using the estimated parameters by TMCMC for (**a**) RR case, and (**b**) LL case.

page intentionally left blank

9 Conclusions

9.1 Summary of contributions

The main objective of the current study has been the comprehension of uncertainty origins affecting the MEMS performance when the desired dimensions of components of MEMS devices are on the order of the material length scale (e.g. grain size for polycrystalline materials) or of the fabrication tolerances. Such goal is obtained through the comparison made between the experiments and modelling results. Moreover, parameter estimation techniques have been developed to help new MEMS designs. This research contributes mainly to four different research areas: i) on-chip testing for MEMS devices, ii) investigation into the uncertainties linked to the material properties at the micro scale, iii) uncertainty assessment and parameter estimation methods, and iv) reduced order modelling of nonlinear coupled-field problems which often involves time consuming numerical approaches.

The principal contributions and major findings of this work can be summarized as follows.

- A simple on-chip test device, featuring micro beams of polysilicon at different lengths, based on standard MEMS fabrication techniques, has been proposed. Different beam lengths allow to study the effects of geometry on the variations of device responses which might occur at the micro scale. The actuation/sensing has been realized using the conventional electrostatic

method (i.e. capacitors) to resemble the commercial MEMS devices. Four testing configurations have been incorporated in the design to allow for result redundancy and to provide a cross-validation scheme for further system identification purposes. The dimensions of the device components (i.e. the micro beam width and the capacitor gap) have been designed to be comparable to the grain size and the fabrication tolerances. This permits to exhibit the effects of uncertainty sources (related either to the material properties or the geometry) on the electromechanical response of these devices.

- As for the electromechanical response of the devices, a large scattering has been observed among nominally identical devices. Two sets of Monte Carlo simulations have been carried out to relate the scattering of the responses to the random morphology of polysilicon. In these analyses, the measured responses of two specimens featuring different beam lengths have been considered, thus highlighting the relation between the geometry of a critical detail at the grain size length-scale and scatterings in the measurements. It has been noted that the effects of the material properties variation (due to the random morphology) on the responses increase as the beam length decreases. It has been also observed that the role of these uncertainties is not generally as significant as the fabrication inaccuracies.

- Large scatterings in the electromechanical responses of nominally identical devices have been observed experimentally. Among the possible uncertainty sources, the important ones have been analyzed in this work through parametric modelling. It has been shown that allowing for variations at i) the over-etch, ii) the Young's modulus and iii) the rotational offset at the specimen, the experimental scattering can be properly explained.

- Uncertainty quantification for the MEMS devices, a crucial result in an industrial context for the development of new MEMS, has been carried out in this work through parameter estimation methods. The unknown value of the three parameters has been estimated for each specimen according to the measurements. To validate this procedure, the parameter estimation has been individually carried out twice, using two sets of measurements (for each

specimen). By comparing the results from the two calculations, a reasonable degree of consistency has been observed for the estimated parameters.

- For these MEMS devices, particle filtering can be used for parameter estimation. This stochastic method takes the measurement errors into account and provides, rather than a single value for the parameter, the PDF of the parameters. This approach is often used in on-line parameter estimation of dynamic systems; it has been shown that this filtering procedure can be robust and stable in the case of this electromechanical problem.

- As a parameter estimation framework for nonlinear coupled-field systems, a Bayesian-based approach has been proposed. The transitional Markov chain Monte Carlo (TMCMC) method is adopted, because not only it takes the measurement errors into account, but also it is an off-line method which is a more suitable method for parameter estimation at static problems like the problem in hand. This stochastic approach is effective at providing the PDF of high-dimensional or multi-modal unknown parameters. Due to the large of number of simulations involved in the TMCMC, the strategy to deal with the computational effort of the physical system parametric model is crucial. Since analytical modelling is often limited to simple geometries, a synergy between the proper orthogonal decomposition (POD) and kriging metamodelling is proposed to reduce the computational burden of numerical models (e.g. FE model). This approach yields high computing speedup while maintaining the accuracy of the model reasonably high. The method can be easily coupled with any high-fidelity model (e.g. commercial codes), and it has been successfully applied to construct the reduced model of the FE model of the MEMS device. The use of the POD-kriging has allowed to obtain a huge computational gain; the original FE model requires up to 30 minutes of computation time, while the POD-kriging model takes just few milliseconds on the same computer[1]. The effectiveness of the method has been demonstrated by proper sampling of the joint probability distributions of the unknown parameters based on the experimental data.

[1] A personal computer with an Intel®Core™i7 3.00 GHz processor.

Finally, it is worth noting several other points. The test device proposed in this work features a simple geometry and actuation/sensing mechanism. These characteristics make it applicable for characterization of other fabrication techniques and different materials. Regarding the experimental scatterings observed in this work, it has been confirmed that considerable attention should be paid when dealing with polycrystalline components at the same scale of grain size. As a consequence, even with an ideal fabrication, polycrystalline anisotropy is expected to be an important issue in nanoelectromechanical systems (NEMS). Because of their submicron size, their mechanical characteristics must be described in statistical rather than deterministic terms, as also shown in [Cho and Chasiotis, 2007]. Even though the POD-kriging TMCMC has been applied here to a coupled electromechanical problem only, in the author's opinion, the application of this methodology in other engineering problems (e.g. fluid-solid interaction problems, often characterized by many DOFs and high computational effort) may bring promising outcomes.

9.2 Suggestions for future research

Based on the work presented in this thesis, several developments can be considered for further research.

- The size-dependent elastic behaviour of submicron objects has been widely investigated using higher order elasticity models, e.g. gradient or micropolar elasticity [Bruggi et al., 2016, Cordero et al., 2015], and also experimentally (see, for example [Liebold and Müller, 2016, Sadeghian et al., 2009, Agrawal et al., 2008]). The experimental campaign of this work can be further extended to different specimen geometries in order to shed more light on these microstructural effects on the actual system's response. To this aim, more samples (with different width or length) can be fabricated and tested to draw more reliable conclusions.

- A cross-validation scheme has been devised in the test device as an easy and affordable way to obtain more reliable estimates of the unknown parameters without damaging the specimens. Such technique can be interesting in an

industrial context. However, a further investigation can be carried out by removing the caps of the MEMS devices to confirm the estimated geometric parameters by visual observation of the actual specimen. Nevertheless, the removal process may be carried out with much attention so that the device would not be damaged.

- The POD-kriging reduction method can be further improved by implementing an adaptive and sequential sampling method (similar to the one proposed in [Braconnier et al., 2011]). Such method can perform the sampling process in a more robust and more efficient way with respect to the *a priori* method used in this work, thanks to its ability to assign more sampling points in the parameter space. The location of new sampling points must be chosen according to a criterion which depends on the accuracy of the reduced model at that location.

- Several classes of FE models can be adopted featuring different uncertainty sources. The TMCMC approach can be then employed to derive the evidence (normalizing constant in Bayes' Theorem) of each model in order to recognize the most suitable one (i.e. second level of Bayesian inference). Moreover, the Gaussian measurement noise can be considered with an unknown covariance; in this way, the noise level in the measurements is not known *a priori*. This unknown parameter can be subsumed into the uncertain parameters vector, and inferred along with the other parameters (see [Green and Worden, 2015]).

page intentionally left blank

References

[Agrawal et al., 2008] Agrawal, R., Peng, B., Gdoutos, E. E., and Espinosa, H. D. (2008). Elasticity size effects in ZnO nanowires- A combined experimental-computational approach. *Nano Letters*, 8(11):3668–3674. 9.2

[Alper et al., 2008] Alper, S., Temiz, Y., and Akin, T. (2008). A compact angular rate sensor system using a fully decoupled silicon-on-glass MEMS gyroscope. *Journal of Microelectromechanical Systems*, 17(6):1418–1429. 2.4, 2.4, 5.4.3

[Angelikopoulos et al., 2012] Angelikopoulos, P., Papadimitriou, C., and Koumoutsakos, P. (2012). Bayesian uncertainty quantification and propagation in molecular dynamics simulations: A high performance computing framework. *The Journal of Chemical Physics*, 137(14):144103. 8.6

[Angelikopoulos et al., 2015] Angelikopoulos, P., Papadimitriou, C., and Koumoutsakos, P. (2015). X-TMCMC: Adaptive kriging for Bayesian inverse modeling. *Computer Methods in Applied Mechanics and Engineering*, 289:409–428. 1.2

[Arulampalam et al., 2002] Arulampalam, M., Maskell, S., Gordon, N., and Clapp, T. (2002). A tutorial on particle filters for online nonlinear/non-Gaussian Bayesian tracking. *IEEE Transactions on Signal Processing*, 50(2):174–188. 6.2

[Au and Beck, 2003] Au, S. and Beck, J. (2003). Important sampling in high dimensions. *Structural Safety*, 25(2):139–163. 8.6

[Axerio et al., 2010] Axerio, J., Wang, Q., and Iaccarino, G. (2010). Constructing response surfaces using imperfect function evaluations. In *Proceedings of the Structures, Structural Dynamics, and Materials Conference*, page 2925. 8.5.1

[Bagley, 1967] Bagley, J. D. (1967). *The behavior of adaptive systems which employ genetic and correlation algorithms*. PhD thesis, University of Michigan. 7.3

[Balachandran et al., 2016] Balachandran, G. K., Petkov, V. P., Mayer, T., and Balslink, T. (2016). A 3-axis gyroscope for electronic stability control with continuous self-test. *IEEE Journal of Solid-State Circuits*, 51(1):177–186. 2.5.5

[Ballarini et al., 1999] Ballarini, R., Mullen, R., and Heuer, A. (1999). The effects of heterogeneity and anisotropy on the size effect in cracked polycrystalline films. In *Fracture Scaling*, pages 19–39. Springer. 2.4

[Bank et al., 1988] Bank, R. E., Dupont, T. F., and Yserentant, H. (1988). The hierarchical basis multigrid method. *Numerische Mathematik*, 52(4):427–458. 8.5.1

[Barthelmann et al., 2000] Barthelmann, V., Novak, E., and Ritter, K. (2000). High dimensional polynomial interpolation on sparse grids. *Advances in Computational Mathematics*, 12(4):273–288. 8.5.1

[Beck and Au, 2002] Beck, J. L. and Au, S.-K. (2002). Bayesian updating of structural models and reliability using Markov chain Monte Carlo simulation. *Journal of Engineering Mechanics*, 128(4):380–391. 8.6, 8.6

[Beck and Katafygiotis, 1998] Beck, J. L. and Katafygiotis, L. S. (1998). Updating models and their uncertainties. I: Bayesian statistical framework. *Journal of Engineering Mechanics*, 124(4):455–461. 8.6

[Bergers et al., 2014] Bergers, L. I. J. C., Hoefnagels, J. P. M., and Geers, M. G. D. (2014). On-wafer time-dependent high reproducibility nano-force tensile testing. *Journal of Physics D: Applied Physics*, 47(49):495306. 3.5

[Berghen, 2004] Berghen, F. V. (2004). Levenberg-Marquardt algorithms vs trust region algorithms. *IRIDIA, Université Libre de Bruxelles*. 1

[Berkooz et al., 1993] Berkooz, G., Holmes, P., and Lumley, J. L. (1993). The proper orthogonal decomposition in the analysis of turbulent flows. *Annual Review of Fluid Mechanics*, 25(1):539–575. 8.2

[Bissantz et al., 2004] Bissantz, N., Hohage, T., and Munk, A. (2004). Consistency and rates of convergence of nonlinear Tikhonov regularization with random noise. *Inverse Problems*, 20(6):1773. 7.4

[Bolzon and Buljak, 2011] Bolzon, G. and Buljak, V. (2011). An effective computational tool for parametric studies and identification problems in materials mechanics. *Computational Mechanics*, 48(6):675–687. 8.5.1

[Box et al., 1978] Box, G. E. P., Hunter, W. G., and Hunter, J. S. (1978). *Statistics for Experimenters: An Introduction to Design, Data Analysis, and Model Building*. John Wiley & Sons. 8.4

[Braconnier et al., 2011] Braconnier, T., Ferrier, M., Jouhaud, J.-C., Montagnac, M., and Sagaut, P. (2011). Towards an adaptive POD/SVD surrogate model for aeronautic design. *Computers & Fluids*, 40(1):195–209. 1.2, 8.3, 8.5.1, 9.2

[Brand et al., 2013] Brand, O., Fedder, G. K., Hierold, C., Korvink, J. G., Tabata, O., and Tsuchiya, T. (2013). *Reliability of MEMS: Testing of Materials and Devices*. John Wiley & Sons. 1.1, 2.4, 2.4

[Brantley, 1973] Brantley, W. (1973). Calculated elastic constants for stress problems associated with semiconductor devices. *Journal of Applied Physics*, 44(1):534–535. (document), 2.1

[Bromley et al., 1999] Bromley, S., Howell, L., and Jensen, B. (1999). Determination of maximum allowable strain for polysilicon micro-devices. *Engineering Failure Analysis*, 6(1):27–41. 2.4

[Bruggi et al., 2016] Bruggi, M., Zega, V., and Corigliano, A. (2016). Synthesis of auxetic structures using optimization of compliant mechanisms and a micropolar material model. *Structural and Multidisciplinary Optimization*, 55(1):1–12. 9.2

[Buljak and Maier, 2011] Buljak, V. and Maier, G. (2011). Proper orthogonal decomposition and radial basis functions in material characterization based on instrumented indentation. *Engineering Structures*, 33(2):492–501. 8.2, 8.3

[Bustillo et al., 1998] Bustillo, J. M., Howe, R. T., and Muller, R. S. (1998). Surface micromachining for microelectromechanical systems. *Proceedings of the IEEE*, 86(8):1552–1574. 2.2

[Cadini et al., 2009] Cadini, F., Zio, E., and Avram, D. (2009). Monte Carlo-based filtering for fatigue crack growth estimation. *Probabilistic Engineering Mechanics*, 24(3):367–373. 6.2, 6.3, 6.3, 6.4

[Capellari et al., 2015] Capellari, G., Eftekhar Azam, S., and Mariani, S. (2015). Damage detection in flexible plates through reduced-order modeling and hybrid particle-kalman filtering. *Sensors*, 16(1):2. 6.3

[Celeux et al., 2000] Celeux, G., Hurn, M., and Robert, C. P. (2000). Computational and inferential difficulties with mixture posterior distributions. *Journal of the American Statistical Association*, 95(451):957–970. 1

[Chen et al., 2015] Chen, S., Montgomery, J., and Bolufé-Röhler, A. (2015). Measuring the curse of dimensionality and its effects on particle swarm optimization and differential evolution. *Applied Intelligence*, 42(3):514–526. 7.4

[Chen et al., 2012] Chen, T., Tang, K., Chen, G., and Yao, X. (2012). A large population size can be unhelpful in evolutionary algorithms. *Theoretical Computer Science*, 436:54–70. 7.4

[Chen, 2013] Chen, Y. (2013). *Deformation Behavior of Thin Metallic Wires under Tensile and Torsional Loadings*, volume 26. KIT Scientific Publishing. 2.5.3

[Ching and Chen, 2007] Ching, J. and Chen, Y.-C. (2007). Transitional Markov chain Monte Carlo method for Bayesian model updating, model class selection, and model averaging. *Journal of Engineering Mechanics*, 133(7):816–832. 8.1, 8.6, 1, 8.6

[Ching and Wang, 2016] Ching, J. and Wang, J.-S. (2016). Application of the transitional Markov chain Monte Carlo algorithm to probabilistic site characterization. *Engineering Geology*, 203:151–167. 8.6

[Cho et al., 2005] Cho, S., Cárdenas-García, J. F., and Chasiotis, I. (2005). Measurement of nanodisplacements and elastic properties of MEMS via the microscopic hole method. *Sensors and Actuators A: Physical*, 120(1):163–171. 1.2, 2.3

[Cho and Chasiotis, 2007] Cho, S. and Chasiotis, I. (2007). Elastic properties and representative volume element of polycrystalline silicon for MEMS. *Experimental Mechanics*, 47(1):37–49. 1.2, 2.4, 2.4, 6.4, 9.1

[Choudhary and Iniewski, 2013] Choudhary, V. and Iniewski, K. (2013). *MEMS: Fundamental Technology and Applications*. CRC Press. 1.1

[Cohen and Kalfon-Cohen, 2013] Cohen, S. R. and Kalfon-Cohen, E. (2013). Dynamic nanoindentation by instrumented nanoindentation and force microscopy: A comparative review. *Beilstein Journal of Nanotechnology*, 4(1):815–833. 2.5.4

[Comi et al., 2010] Comi, C., Corigliano, A., Langfelder, G., Longoni, A., Tocchio, A., and Simoni, B. (2010). A resonant microaccelerometer with high sensitivity operating in an oscillating circuit. *Journal of Microelectromechanical Systems*, 19(5):1140–1152. 3.2

[Confalonieri, 2013] Confalonieri, F. (2013). *A domain decomposition approach for the simulation of fracture phenomena in polycrystalline microsystems*. PhD thesis, Politecnico di Milano. 8.2

[Confalonieri et al., 2014] Confalonieri, F., Ghisi, A., Cocchetti, G., and Corigliano, A. (2014). A domain decomposition approach for the simulation of fracture phenomena in polycrystalline microsystems. *Computer Methods in Applied Mechanics and Engineering*, 277:180–218. 8.2

[Congdon, 2014] Congdon, P. (2014). *Applied Bayesian Modelling*. John Wiley & Sons. 6.2

[Cordero et al., 2015] Cordero, N. M., Forest, S., and Busso, E. P. (2015). Second strain gradient elasticity of nano-objects. *Journal of the Mechanics and Physics of Solids*. 9.2

[Corigliano et al., 2005] Corigliano, A., Cacchione, F., De Masi, B., and Riva, C. (2005). On-chip electrostatically actuated bending tests for the mechanical characterization of polysilicon at the micro scale. *Meccanica*, 40:485–503. (document), 2.5, 2.9

[Corigliano et al., 2004] Corigliano, A., De Masi, B., Frangi, A., Comi, C., Villa, A., and Marchi, M. (2004). Mechanical characterization of polysilicon through on-chip tensile tests. *Journal of Microelectromechanical Systems*, 13(2):200–219. 2.2.1, 2.2.1

[Corigliano et al., 2010] Corigliano, A., Domenella, L., and Langfelder, G. (2010). On-chip mechanical characterization using an electro-thermo-mechanical actuator. *Experimental Mechanics*, 50(6):695–707. (document), 2.4, 2.7, 2.5.2, 2.6

[Corigliano et al., 2013] Corigliano, A., Dossi, M., and Mariani, S. (2013). Domain decomposition and model order reduction methods applied to the simulation of multi-physics problems in MEMS. *Computers & Structures*, 122:113–127. 8.2

[Corigliano et al., 2015] Corigliano, A., Dossi, M., and Mariani, S. (2015). Model order reduction and domain decomposition strategies for the solution of the dynamic elastic–plastic structural problem. *Computer Methods in Applied Mechanics and Engineering*, 290:127–155. 8.2

[Costa et al., 1999] Costa, J.-P., Pronzato, L., and Thierry, E. (1999). A comparison between kriging and radial basis function networks for nonlinear prediction. In *Proceedings of the IEEE Workshop on Nonlinear Signal and Image Processing*, pages 726–730. 8.3

[de Laat et al., 2016] de Laat, M., Pérez Garza, H., Herder, J., and Ghatkesar, M. (2016). A review on *in situ* stiffness adjustment methods in MEMS. *Journal of Micromechanics and Microengineering*, 26:063001. 2.4

[Deb and Blanton, 2002] Deb, N. and Blanton, R. (2002). Built-in self test of CMOS-MEMS accelerometers. In *Proceedings of the IEEE International Test Conference*, pages 1075–1084. 2.5.5

[Deparis et al., 2004] Deparis, S., Discacciati, M., and Quarteroni, A. (2004). A domain decomposition framework for fluid-structure interaction problems. In *Proceedings of the International Conference on Computational Fluid Dynamics*, pages 41–58. Springer. 8.2

[Der Kiureghian and Ditlevsen, 2009] Der Kiureghian, A. and Ditlevsen, O. (2009). Aleatory or epistemic? Does it matter? *Structural Safety*, 31(2):105–112. 1

[Djuric et al., 2003] Djuric, P. M., Kotecha, J. H., Zhang, J., Huang, Y., Ghirmai, T., Bugallo, M. F., and Miguez, J. (2003). Particle filtering. *IEEE Signal Processing Magazine*, 20(5):19–38. 6.1

[Douc et al., 2005] Douc, R., Cappè, O., and Moulines, E. (2005). Comparison of resampling schemes for particle filtering. In *Proceedings of the International Symposium on Image and Signal Processing and Analysis*, pages 64–69. 6.3

[Doucet, 1997] Doucet, A. (1997). *Monte Carlo methods for Bayesian estimation of hidden Markov models. Application to radiation signals.* PhD thesis, University Paris-Sud Orsay. 6.3

[Doucet et al., 2000] Doucet, A., Godsill, S., and Andrieu, C. (2000). On sequential Monte Carlo sampling methods for Bayesian filtering. *Statistics and Computing*, 10(3):197–208. 6.1, 6.3

[Doucet and Johansen, 2009] Doucet, A. and Johansen, A. (2009). A tutorial on particle filtering and smoothing: Fifteen years later. *Handbook of Nonlinear Filtering*, 12. 6.3, 6.3

[Du et al., 1999] Du, Q., Faber, V., and Gunzburger, M. (1999). Centroidal Voronoi tessellations: applications and algorithms. *SIAM Review*, 41(4):637–676. 2.3.2, 8.5.1

[Dubourg et al., 2011] Dubourg, V., Sudret, B., and Bourinet, J.-M. (2011). Reliability-based design optimization using kriging surrogates and subset simulation. *Structural and Multidisciplinary Optimization*, 44(5):673–690. 8.4, 8.4

[Eftekhar Azam, 2014] Eftekhar Azam, S. (2014). *Online Damage Detection in Structural Systems: Applications of Proper Orthogonal Decomposition, and Kalman and Particle Filters.* Springer Science & Business Media. 6.2

[Eftekhar Azam et al., 2012] Eftekhar Azam, S., Bagherinia, M., and Mariani, S. (2012). Stochastic system identification via particle and sigma-point Kalman filtering. *Scientia Iranica*, 19(4):982–991. 6.2

[Eftekhar Azam and Mariani, 2012] Eftekhar Azam, S. and Mariani, S. (2012). Dual estimation of partially observed nonlinear structural systems: A particle filter approach. *Mechanics Research Communications*, 46:54–61. 6.2

[Eftekhar Azam and Mariani, 2013] Eftekhar Azam, S. and Mariani, S. (2013). Investigation of computational and accuracy issues in POD-based reduced order modeling of dynamic structural systems. *Engineering structures*, 54:150–167. 8.3

[Espinosa et al., 2012] Espinosa, H. D., Bernal, R. A., and Filleter, T. (2012). *In situ* TEM electromechanical testing of nanowires and nanotubes. *Small*, 8(21):3233–3252. 2.5.1

[Espinosa et al., 2007] Espinosa, H. D., Zhu, Y., and Moldovan, N. (2007). Design and operation of a MEMS-based material testing system for nanomechanical characterization. *Journal of Microelectromechanical Systems*, 16(5):1219–1231. 2.4

[Fachin, 2007] Fachin, F. (2007). Un approccio multi-scala per l'analisi di affidabilit di sensori MEMS per applicazioni spaziali. Master's thesis, Politecnico di Milano. (document), 2.1

[Feeny and Kappagantu, 1998] Feeny, B. and Kappagantu, R. (1998). On the physical interpretation of proper orthogonal modes in vibrations. *Journal of Sound and Vibration*, 211(4):607–616. 1

[Fleck et al., 1994] Fleck, N., Muller, G., Ashby, M., and Hutchinson, J. (1994). Strain gradient plasticity: Theory and experiment. *Acta Metallurgica et Materialia*, 42(2):475–487. 2.5.3

[Flury and Shephard, 2009] Flury, T. and Shephard, N. (2009). *Learning and Filtering via Simulation: Smoothly Jittered Particle Filters.* Technical report. University of Oxford. 6.3

[Fossati and Habashi, 2013] Fossati, M. and Habashi, W. G. (2013). Multiparameter analysis of aero-icing problems using proper orthogonal decomposition and multidimensional interpolation. *AIAA Journal*, 51(4):946–960. 8.1

[Fragakis and Papadrakakis, 2003] Fragakis, Y. and Papadrakakis, M. (2003). The mosaic of high performance domain decomposition methods for structural mechanics: Formulation, interrelation and numerical efficiency of primal and dual methods. *Computer Methods in Applied Mechanics and Engineering*, 192(35):3799–3830. 8.2

[Frangi et al., 2013] Frangi, A., Cremonesi, M., Jaakkola, A., and Pensala, T. (2013). Analysis of anchor and interface losses in piezoelectric MEMS resonators. *Sensors and Actuators, A: Physical*, 190:127–135. 6.4

[Gad-el Hak, 2001] Gad-el Hak, M. (2001). *The MEMS handbook*. CRC Press. 1.1, 2.2, 2.4, 5.4.3

[Geers et al., 2010] Geers, M. G., Kouznetsova, V. G., and Brekelmans, W. (2010). Multi-scale computational homogenization: Trends and challenges. *Journal of Computational and Applied Mathematics*, 234(7):2175–2182. 8.2

[Ghahramani et al., 1999] Ghahramani, Z., Beal, M. J., et al. (1999). Variational inference for bayesian mixtures of factor analysers. In *Advances in Neural Information Processing Systems*, volume 12, pages 449–455. 8.6

[Ghanem and Spanos, 2003] Ghanem, R. G. and Spanos, P. D. (2003). *Stochastic Finite Elements: A Spectral Approach*. Springer. 8.4

[Gibson, 2014] Gibson, R. F. (2014). A review of recent research on nanoindentation of polymer composites and their constituents. *Composites Science and Technology*, 105:51–65. 2.5.4

[Goller et al., 2011] Goller, B., Broggi, M., Calvi, A., and Schueller, G. (2011). A stochastic model updating technique for complex aerospace structures. *Finite Elements in Analysis and Design*, 47(7):739–752. 8.6

[Gosselet and Rey, 2006] Gosselet, P. and Rey, C. (2006). Non-overlapping domain decomposition methods in structural mechanics. *Archives of Computational Methods in Engineering*, 13(4):515–572. 8.2

[Gravier et al., 2009] Gravier, S., Coulombier, M., Safi, A., Andr, N., Bo, A., Raskin, J.-P., and Pardoen, T. (2009). New on-chip nanomechanical testing laboratory - Applications to aluminum and polysilicon thin films. *Journal of Microelectromechanical Systems*, 18(3):555–569. 2.4

[Green, 2015a] Green, P. (2015a). Bayesian system identification of a nonlinear dynamical system using a novel variant of simulated annealing. *Mechanical Systems and Signal Processing*, 52:133–146. 1

[Green, 2015b] Green, P. (2015b). Bayesian system identification of dynamical systems using large sets of training data: A MCMC solution. *Probabilistic Engineering Mechanics*, 42:54–63. 1

[Green and Worden, 2015] Green, P. and Worden, K. (2015). Bayesian and Markov chain Monte Carlo methods for identifying nonlinear systems in the presence of uncertainty. *Philosophical Transactions of the Royal Society A: Mathematical, Physical and Engineering Sciences*, 373(2051):20140405. 1.2, 8.6, 8.6, 9.2

[Green, 1995] Green, P. J. (1995). Reversible jump Markov chain Monte Carlo computation and Bayesian model determination. *Biometrika*, 82(4):711–732. 8.6

[Green et al., 2015] Green, P. L., Hendijanizadeh, M., Simeone, L., and Elliott, S. (2015). Probabilistic modelling of a rotational energy harvester. *Journal of Intelligent Material Systems and Structures*, 27(4):528–536. 8.6

[Haasdonk, 2013] Haasdonk, B. (2013). Convergence rates of the POD–greedy method. *Mathematical Modelling and Numerical Analysis*, 47(3):859–873. 8.5.1

[Halton, 1960] Halton, J. H. (1960). On the efficiency of certain quasi-random sequences of points in evaluating multi-dimensional integrals. *Numerische Mathematik*, 2(1):84–90. 8.5.1

[Hanhijrvi et al., 2012] Hanhijrvi, K., Kassamakov, I., Heikkinen, V., Aaltonen, J., Sainiemi, L., Grigoras, K., Franssila, S., and Haeggstrm, E. (2012). Stroboscopic supercontinuum white-light interferometer for MEMS characterization. *Optics Letters*, 37(10):1703–1705. 2.6

[Hardy, 1971] Hardy, R. L. (1971). Multiquadric equations of topography and other irregular surfaces. *Journal of Geophysical Research*, 76(8):1905–1915. 8.4

[Hart et al., 2000] Hart, M., Conant, R., Lau, K., and Muller, R. (2000). Stroboscopic interferometer system for dynamic MEMS characterization. *Journal of Microelectromechanical Systems*, 9(4):409–418. 2.6

[Hastings, 1970] Hastings, W. K. (1970). Monte Carlo sampling methods using Markov chains and their applications. *Biometrika*, 57(1):97–109. 8.6

[Hol et al., 2006] Hol, J., Schön, T., and Gustafsson, F. (2006). On resampling algorithms for particle filters. In *Proceedings of the IEEE Nonlinear Statistical Signal Processing Workshop*, pages 79–82. 6.3

[Holland, 1975] Holland, J. H. (1975). *Adaptation in Natural and Artificial Systems: An Introductory Analysis with Applications to Biology, Control, and Artificial Intelligence.* University of Michigan Press. 7.3, 7.3

[Hong et al., 2000] Hong, Y., Lee, J., and Kim, S. (2000). Laterally driven symmetric micro-resonator for gyroscopic applications. *Journal of Micromechanics and Microengineering*, 10(3):452–458. 2.4, 2.4, 5.4.3

[Hopcroft et al., 2010] Hopcroft, M., Nix, W., and Kenny, T. (2010). What is the Young's modulus of silicon? *Journal of Microelectromechanical Systems*, 19(2):229–238. (document), 2.2, 2.4, 6.4

[Hsu, 2008] Hsu, T.-R. (2008). *MEMS and Microsystems: Design, Manufacture, and Nanoscale Engineering.* John Wiley & Sons. 1.1

[Hukushima and Nemoto, 1996] Hukushima, K. and Nemoto, K. (1996). Exchange Monte Carlo method and application to spin glass simulations. *Journal of the Physical Society of Japan*, 65(6):1604–1608. 1

[Jang et al., 2012] Jang, Y.-H., Kim, J.-W., Kim, J.-M., and Kim, Y.-K. (2012). Engineering design guide for etch holes to compensate spring width loss for reliable resonant frequencies. In *Proceedings of the IEEE International Conference on Micro Electro Mechanical Systems*, pages 424–427. 2.4

[Jin et al., 2003] Jin, R., Du, X., and Chen, W. (2003). The use of metamodeling techniques for optimization under uncertainty. *Structural and Multidisciplinary Optimization*, 25(2):99–116. 8.3

[Kamiya et al., 2007] Kamiya, S., Kuypers, J. H., Trautmann, A., Ruther, P., and Paul, O. (2007). Process temperature–dependent mechanical properties of polysilicon measured using a novel tensile test structure. *Journal of Microelectromechanical Systems*, 16(2):202–212. 2.4

[Kanit et al., 2003] Kanit, T., Forest, S., Galliet, I., Mounoury, V., and Jeulin, D. (2003). Determination of the size of the representative volume element for random composites: Statistical and numerical approach. *International Journal of Solids and Structures*, 40(13):3647–3679. 2.4

[Kawai et al., 2006] Kawai, Y., Ono, T., Meyers, E., Gerber, C., and Esashi, M. (2006). Piezoelectric actuator integrated cantilever with tunable spring constant for atom probe. In *Proceedings of the IEEE International Conference on Micro Electro Mechanical Systems*, pages 778–781. 2.4

[Kerschen et al., 2005] Kerschen, G., Golinval, J.-C., Vakakis, A. F., and Bergman, L. A. (2005). The method of proper orthogonal decomposition for dynamical characterization and order reduction of mechanical systems: An overview. *Nonlinear Dynamics*, 41(1-3):147–169. 8.2, 8.3

[Kirkpatrick, 1984] Kirkpatrick, S. (1984). Optimization by simulated annealing: Quantitative studies. *Journal of Statistical Physics*, 34(5-6):975–986. 8.6

[Kişi and Uncuoglu, 2005] Kişi, Ö. and Uncuoglu, E. (2005). Comparison of three back-propagation training algorithms for two case studies. *Indian Journal of Engineering & Materials Sciences*, 12(5):434–442. 7.2

[Klimke, 2007] Klimke, A. (2007). *Sparse Grid Interpolation Toolbox–user's guide*. IANS Report. 8.5.1

[Kouznetsova et al., 2002] Kouznetsova, V., Geers, M. G. D., and Brekelmans, W. A. M. (2002). Multi-scale constitutive modelling of heterogeneous materials with a gradient-enhanced computational homogenization scheme. *International Journal for Numerical Methods in Engineering*, 54(8):1235–1260. 8.2

[Lam et al., 2003] Lam, D. C. C., Yang, F., Chong, A., Wang, J., and Tong, P. (2003). Experiments and theory in strain gradient elasticity. *Journal of the Mechanics and Physics of Solids*, 51(8):1477–1508. 4.2.2, 4.4

[Lam et al., 2015] Lam, H.-F., Yang, J., and Au, S.-K. (2015). Bayesian model updating of a coupled-slab system using field test data utilizing an enhanced Markov chain Monte Carlo simulation algorithm. *Engineering Structures*, 102:144–155. 8.6

[Laurenceau and Sagaut, 2008] Laurenceau, J. and Sagaut, P. (2008). Building efficient response surfaces of aerodynamic functions with kriging and cokriging. *AIAA journal*, 46(2):498–507. 8.4, 8.5.1

[Leblond and Sigrist, 2016] Leblond, C. and Sigrist, J.-F. (2016). A reduced basis approach for the parametric low frequency response of submerged viscoelastic structures. *Finite Elements in Analysis and Design*, 119:15–29. 8.5.1

[Legendre et al., 2013] Legendre, O., Bertin, H., Mathias, H., Megherbi, S., Juillard, J., Colinet, E., and Jafari, K. (2013). A low-cost built-in self-test method for thermally actuated resistive MEMS sensors. *Sensors and Actuators A: Physical*, 194:8–15. 2.5.5

[Li et al., 2012] Li, T., Sattar, T., and Sun, S. (2012). Deterministic resampling: Unbiased sampling to avoid sample impoverishment in particle filters. *Signal Processing*, 92(7):1637–1645. 6.3

[Li et al., 2014] Li, T., Sun, S., Sattar, T., and Corchado, J. (2014). Fight sample degeneracy and impoverishment in particle filters: A review of intelligent approaches. *Expert Systems with Applications*, 41(8):3944–3954. 6.3

[Liang et al., 2002] Liang, Y., Lee, H., Lim, S., Lin, W., Lee, K., and Wu, C. (2002). Proper orthogonal decomposition and its applications Part I: Theory. *Journal of Sound and Vibration*, 252(3):527–544. 8.3, 1

[Liebold and Müller, 2016] Liebold, C. and Müller, W. H. (2016). Applications of higher-order continua to size effects in bending: Theory and recent experimental results. In *Generalized Continua as Models for Classical and Advanced Materials*, pages 237–260. Springer. 9.2

[Liu et al., 2012] Liu, D., He, Y., Tang, X., Ding, H., Hu, P., and Cao, P. (2012). Size effects in the torsion of microscale copper wires: Experiment and analysis. *Scripta Materialia*, 66(6):406–409. (document), 2.5.3, 2.10

[Liu et al., 2001] Liu, J., Chen, R., and Logvinenko, T. (2001). A theoretical framework for sequential importance sampling with resampling. In *Sequential Monte Carlo Methods in Practice*, pages 225–246. Springer. 6.3

[Lophaven et al., 2002] Lophaven, S. N., Nielsen, H. B., and Søndergaard, J. (2002). Dace-A Matlab Kriging toolbox, version 2.0. Technical report. 8.4

[Lucon, 2014] Lucon, E. (2014). Testing of small-sized specimens. *Comprehensive Materials Processing*, 1:135–163. 2.5

[Maday and Stamm, 2013] Maday, Y. and Stamm, B. (2013). Locally adaptive greedy approximations for anisotropic parameter reduced basis spaces. *SIAM Journal on Scientific Computing*, 35(6):2417–2441. 8.5.1

[Manzoni et al., 2012] Manzoni, A., Quarteroni, A., and Rozza, G. (2012). Computational reduction for parametrized PDEs: Strategies and applications. *Milan Journal of Mathematics*, 80(2):283–309. 1, 8.3

[Marelli and Sudret, 2014] Marelli, S. and Sudret, B. (2014). *UQLab: A Framework for Uncertainty Quantification in MATLAB*. ETH-Zürich. 8.4

[Margheri and Sagaut, 2014] Margheri, L. and Sagaut, P. (2014). An uncertainty quantification analysis in a simplified problem of urban pollutant dispersion by means of ANOVA-POD/Kriging-based response surfaces. In *Proceedings*

of the ASME International Conference on Nanochannels, Microchannels, and Minichannels, pages 3–7. 8.5.1

[Margheri and Sagaut, 2016] Margheri, L. and Sagaut, P. (2016). A hybrid anchored-ANOVA–POD/Kriging method for uncertainty quantification in unsteady high-fidelity CFD simulations. *Journal of Computational Physics*, 324:137–173. 1.2, 8.5.1

[Mariani et al., 2009] Mariani, S., Ghisi, A., Corigliano, A., and Zerbini, S. (2009). Modeling impact-induced failure of polysilicon MEMS: A multi-scale approach. *Sensors*, 9(1):556–567. 8.2

[Mariani et al., 2011] Mariani, S., Martini, R., Ghisi, A., Corigliano, A., and Beghi, M. (2011). Overall elastic properties of polysilicon films: A statistical investigation of the effects of polycrystal morphology. *International Journal for Multiscale Computational Engineering*, 9(3):327–346. 2.3, 2.4, 4.1.1, 5.2, 5.4.1, 6.4, 6.4

[Marinari and Parisi, 1992] Marinari, E. and Parisi, G. (1992). Simulated tempering: A new Monte Carlo scheme. *Europhysics Letters*, 19(6):451. 1

[Martini, 2008] Martini, R. (2008). Multi-scale finite element anlaysis of shock-induced MEMS failure, allowing for randomness at micro-scale. Master's thesis, Politecnico di Milano. 2.3.2, 2.3.2

[Matabosch et al., 2014] Matabosch, N. T., Coccetti, F., Kaynak, M., Espana, B., Tillack, B., and Cazaux, J.-L. (2014). Equivalent circuit model of reliable RF-MEMS switches for component synthesis, fabrication process characterization and failure analysis. *International Journal of Microwave and Wireless Technologies*, 6(01):73–81. 2.5.5

[McKay et al., 2000] McKay, M. D., Beckman, R. J., and Conover, W. J. (2000). A comparison of three methods for selecting values of input variables in the analysis of output from a computer code. *Technometrics*, 42(1):55–61. 8.5.1

[Mees et al., 1987] Mees, A., Rapp, P., and Jennings, L. (1987). Singular-value decomposition and embedding dimension. *Physical Review A*, 36(1):340. 1

[Metropolis et al., 1953] Metropolis, N., Rosenbluth, A. W., Rosenbluth, M. N., Teller, A. H., and Teller, E. (1953). Equation of state calculations by fast computing machines. *The journal of chemical physics*, 21(6):1087–1092. 8.6

[Mir et al., 2006] Mir, S., Rufer, L., and Dhayni, A. (2006). Built-in-self-test techniques for MEMS. *Microelectronics Journal*, 37(12):1591–1597. (document), 2.5.5, 2.11

[Mirzazadeh et al., 2015] Mirzazadeh, R., Ghisi, A., and Mariani, S. (2015). Assessment of overetch and polysilicon film properties through on-chip tests. In *Proceedings of the International Electronic Conference on Sensors and Applications*, pages 1–7. 6.4

[Mol et al., 2008] Mol, L., Rocha, L., Cretu, E., and Wolffenbuttel, R. (2008). Read-out calibration of a SOI capacitive transducer using the pull-in voltage. *Journal of Micromechanics and Microengineering*, 18:064009. 6.4

[Mullen et al., 1997] Mullen, R., Ballarini, R., Yin, Y., and Heuer, A. (1997). Monte Carlo simulation of effective elastic constants of polycrystalline thin films. *Acta Materialia*, 45(6):2247–2255. 2.4

[Muto and Beck, 2008] Muto, M. and Beck, J. L. (2008). Bayesian updating and model class selection for hysteretic structural models using stochastic simulation. *Journal of Vibration and Control*, 14(1-2):7–34. 8.6

[Nathanson et al., 1967] Nathanson, H. C., Newell, W. E., Wickstrom, R. A., and Davis, J. R. (1967). The resonant gate transistor. *IEEE Transactions on Electron Devices*, 14(3):117–133. 2.2

[Oh et al., 2005] Oh, C.-S., Lee, H.-J., Ko, S.-G., Kim, S.-W., and Ahn, H.-G. (2005). Comparison of the Young's modulus of polysilicon film by tensile testing and nanoindentation. *Sensors and Actuators A: Physical*, 117(1):151–158. 2.4

[Okada and Sekino, 2003] Okada, K. and Sekino, T. (2003). *Impedance Measurement Handbook*, volume 128. Agilent Technologies. 3.2, 1

[Oliver et al., 2015] Oliver, J., Caicedo, M., Roubin, E., Huespe, A. E., and Hernández, J. (2015). Continuum approach to computational multiscale modeling of propagating fracture. *Computer Methods in Applied Mechanics and Engineering*, 294:384–427. 8.2

[Ortiz et al., 2015] Ortiz, G. A., Alvarez, D. A., and Bedoya-Ruíz, D. (2015). Identification of Bouc–Wen type models using the transitional Markov chain Monte Carlo method. *Computers & Structures*, 146:252–269. 8.6

[Ostrowski et al., 2005] Ostrowski, Z., Białecki, R. A., and Kassab, A. J. (2005). Estimation of constant thermal conductivity by use of proper orthogonal decomposition. *Computational Mechanics*, 37(1):52–59. 8.2, 8.3

[Ozisik, 2000] Ozisik, M. N. (2000). *Inverse Heat Transfer: Fundamentals and Applications*. CRC Press. 7.2

[Pantano et al., 2012] Pantano, M. F., Espinosa, H. D., and Pagnotta, L. (2012). Mechanical characterization of materials at small length scales. *Journal of Mechanical Science and Technology*, 26(2):545–561. (document), 1.1, 2.4, 2.5, 2.8, 2.5.2

[Pantrigo et al.,] Pantrigo, J., Sánchez, A., Montemayor, A., and Kostas, G. Combining particle filter and population-based metaheuristics for visual articulated motion tracking. In *Progress In Computer Vision And Image Analysis*, pages 301 – 320. World Scientific. 6.3

[Patelli et al., 2014] Patelli, E., Alvarez, D. A., Broggi, M., and Angelis, M. d. (2014). Uncertainty management in multidisciplinary design of critical safety systems. *Journal of Aerospace Information Systems*, 12(1):140–169. 7.4

[Paul-Dubois-Taine and Amsallem, 2015] Paul-Dubois-Taine, A. and Amsallem, D. (2015). An adaptive and efficient greedy procedure for the optimal training of parametric reduced-order models. *International Journal for Numerical Methods in Engineering*, 102(5):1262–1292. 8.2

[Petersen, 1982] Petersen, K. E. (1982). Silicon as a mechanical material. *Proceedings of the IEEE*, 70(5):420–457. 2.2

[Radermacher and Reese, 2015] Radermacher, A. and Reese, S. (2015). POD-based model reduction with empirical interpolation applied to nonlinear elasticity. *International Journal for Numerical Methods in Engineering*. 8.2

[Ramadoss et al., 2008] Ramadoss, R., Dean, R., and Xiong, X. (2008). MEMS testing. In *System-on-Chip Test Architectures: Nanometer Design for Testability*, pages 591–646. 2.5.5

[Razavi et al., 2012] Razavi, S., Tolson, B. A., and Burn, D. H. (2012). Review of surrogate modeling in water resources. *Water Resources Research*, 48(7). 8.4

[Rechenberg, 1973] Rechenberg, I. (1973). *Evolutionsstrategie Optimierung Technischer Systeme nach Prinzipien der biologischen Evolution*. Friedrich Frommann Verlag Stuttgart. 7.3

[Reedy et al., 2011] Reedy, E. D., Boyce, B. L., Foulk, J. W., Field, R. V., de Boer, M. P., and Hazra, S. S. (2011). Predicting fracture in micrometer-scale polycrystalline silicon MEMS structures. *Journal of Microelectromechanical Systems*, 20(4):922–932. 2.4

[Robert, 2007] Robert, C. (2007). *The Bayesian Choice: From Decision-Theoretic Foundations to Computational Implementation*. Springer Science & Business Media. 6.2

[Rocha et al., 2011] Rocha, L., Dias, R., Cretu, E., Mol, L., and Wolffenbuttel, R. (2011). Auto-calibration of capacitive MEMS accelerometers based on pull-in voltage. *Microsystem Technologies*, 17(3):429–436. 6.4

[Rocha et al., 2008] Rocha, L., Mol, L., Cretu, E., Wolffenbuttel, R., and Machado da Silva, J. (2008). A pull-in based test mechanism for device diagnostic and process characterization. *VLSI Design*, 2008:1–7. 2.5.5, 6.4

[Rouquette et al., 2007] Rouquette, S., Guo, J., and Le Masson, P. (2007). Estimation of the parameters of a Gaussian heat source by the Levenberg–Marquardt method: Application to the electron beam welding. *International Journal of Thermal Sciences*, 46(2):128–138. 7.2

[Rudnyi and Korvink, 2002] Rudnyi, E. B. and Korvink, J. G. (2002). Review: Automatic model reduction for transient simulation of MEMS-based devices. *Sensors Update*, 11(1):3–33. 8.2

[Sacks et al., 1989a] Sacks, J., Schiller, S. B., and Welch, W. J. (1989a). Designs for computer experiments. *Technometrics*, 31(1):41–47. 1.2, 8.4

[Sacks et al., 1989b] Sacks, J., Welch, W. J., Mitchell, T. J., and Wynn, H. P. (1989b). Design and analysis of computer experiments. *Statistical science*, 4:409–423. 8.4

[Sadeghian et al., 2009] Sadeghian, H., Yang, C., Goosen, J., Van Der Drift, E., Bossche, A., French, P., and Van Keulen, F. (2009). Characterizing size-dependent effective elastic modulus of silicon nanocantilevers using electrostatic pull-in instability. *Applied Physics Letters*, 94(22). 2.4, 9.2

[Saif and MacDonald, 1998] Saif, M. and MacDonald, N. (1998). Microinstruments for submicron material studies. *Journal of Materials Research*, 13(12):3353–3356. 2.5.3

[Santner et al., 2013] Santner, T. J., Williams, B. J., and Notz, W. I. (2013). *The Design and Analysis of Computer Experiments*. Springer Science & Business Media. 8.4, 8.4

[Sharpe, 2008] Sharpe, W. (2008). Mechanical property measurement at the micro/nano-scale. *Strain*, 44(1):20–26. 2.5

[Sharpe Jr. et al., 2001] Sharpe Jr., W., Jackson, K., Hemker, K., and Xie, Z. (2001). Effect of specimen size on Young's modulus and fracture strength of polysilicon. *Journal of Microelectromechanical Systems*, 10:317–326. 2.4

[Simpson et al., 2001] Simpson, T. W., Poplinski, J., Koch, P. N., and Allen, J. K. (2001). Metamodels for computer-based engineering design: Survey and recommendations. *Engineering with Computers*, 17(2):129–150. 8.4

[Sipos et al., 2012] Sipos, M., Paces, P., Rohac, J., and Novacek, P. (2012). Analyses of triaxial accelerometer calibration algorithms. *IEEE Sensors Journal*, 12(5):1157–1165. 7.2

[Sirovich, 1987] Sirovich, L. (1987). Turbulence and the dynamics of coherent structures. I: Coherent structures. *Quarterly of Applied Mathematics*, 45(3):561–571. 1.2, 8.3

[Skilling, 2004] Skilling, J. (2004). Nested sampling. In *Proceedings of the AIP Conference on Bayesian Inference and Maximum Entropy Methods in Science and Engineering*, volume 735, pages 395–405. 8.6

[Sloggett et al., 1986] Sloggett, G., Barton, N., and Spencer, S. (1986). Fringing fields in disc capacitors. *Journal of Physics A: Mathematical and General*, 19(14):2725. 4.2.2

[Smolyak, 1963] Smolyak, S. A. (1963). Quadrature and interpolation formulas for tensor products of certain classes of functions. In *Doklady Akademii Nauk SSSR*, volume 4, page 123. 1.2, 8.5.1

[Sobol, 1967] Sobol, I. M. (1967). On the distribution of points in a cube and the approximate evaluation of integrals. *Zhurnal Vychislitel'noi Matematiki i Matematicheskoi Fiziki*, 7(4):784–802. 8.5.1

[Stefanou et al., 2015] Stefanou, G., Savvas, D., and Papadrakakis, M. (2015). Stochastic finite element analysis of composite structures based on material microstructure. *Composite Structures*, 132:384–392. 8.2

[Syms, 1998] Syms, R. R. (1998). Electrothermal frequency tuning of folded and coupled vibrating micromechanical resonators. *Journal of Microelectromechanical Systems*, 7(2):164–171. 2.4

[Timoshenko and Woinowsky-Krieger, 1959] Timoshenko, S. P. and Woinowsky-Krieger, S. (1959). *Theory of Plates and Shells*. McGraw-Hill. 4.2.1

[Ting et al., 2010] Ting, J.-A., D'Souza, A., Vijayakumar, S., and Schaal, S. (2010). Efficient learning and feature selection in high-dimensional regression. *Neural Computation*, 22(4):831–886. 8.4

[Torun et al., 2007] Torun, H., Sarangapani, K., and Degertekin, F. (2007). Spring constant tuning of active atomic force microscope probes using electrostatic spring softening effect. *Applied Physics Letters*, 91(25):253113. 2.4

[Tsuchiya et al., 2005] Tsuchiya, T., Hirata, M., Chiba, N., Udo, R., Yoshitomi, Y., Ando, T., Sato, K., Takashima, K., Higo, Y., and Saotome, Y. (2005). Cross comparison of thin-film tensile-testing methods examined using single-crystal silicon, polysilicon, nickel, and titanium films. *Journal of Microelectromechanical Systems*, 14(5):1178–1186. 2.4

[Vadakkepat and Jing, 2006] Vadakkepat, P. and Jing, L. (2006). Improved particle filter in sensor fusion for tracking randomly moving object. *IEEE Transactions on Instrumentation and Measurement*, 55(5):1823–1832. 6.3

[Viana et al., 2013] Viana, F. A., Haftka, R. T., and Watson, L. T. (2013). Efficient global optimization algorithm assisted by multiple surrogate techniques. *Journal of Global Optimization*, 56(2):669–689. 8.4

[Volkwein, 2011] Volkwein, S. (2011). Model reduction using proper orthogonal decomposition. Lecture Notes, Institute of Mathematics and Scientific Computing, University of Graz. Graz. Austria. 8.3

[Walter and Kraft, 2011] Walter, M. and Kraft, O. (2011). A new method to measure torsion moments on small-scaled specimens. *Review of Scientific Instruments*, 82(3):035109. 2.5.3

[Wang and Shan, 2007] Wang, G. G. and Shan, S. (2007). Review of metamodeling techniques in support of engineering design optimization. *Journal of Mechanical Design*, 129(4):370–380. 8.4

[Wu et al., 2003] Wu, C., Liang, Y., Lin, W., Lee, H., and Lim, S. (2003). A note on equivalence of proper orthogonal decomposition methods. *Journal of Sound and Vibration*, 265(5):1103–1110. 1

[Xiong et al., 2005] Xiong, X., Wu, Y.-L., and Jone, W.-B. (2005). A dual-mode built-in self-test technique for capacitive MEMS devices. *IEEE Transactions on Instrumentation and Measurement*, 54(5):1739–1750. 2.4, 2.5.5

[Yagnamurthy et al., 2015] Yagnamurthy, S., Boyce, B. L., and Chasiotis, I. (2015). Role of microstructure and doping on the mechanical strength and

toughness of polysilicon thin films. *Journal of Microelectromechanical Systems*, 24(5):1436–1452. 2.3, 2.4, 2.5.1

[Yuan, 2000] Yuan, Y.-X. (2000). A review of trust region algorithms for optimization. In *Proceedings of the International Congress on Industrial and Applied Mathematics*, pages 271–282. 1

[Yuen, 2010] Yuen, K.-V. (2010). *Bayesian Methods for Structural Dynamics and Civil Engineering*. John Wiley & Sons. 1.2, 6.2

[Zhang et al., 2013] Zhang, H., Dai, H., Beer, M., and Wang, W. (2013). Structural reliability analysis on the basis of small samples: An interval quasi-Monte Carlo method. *Mechanical Systems and Signal Processing*, 37(1):137–151. 4.1.1

[Zhong et al., 2013] Zhong, Z.-Y., Zhang, W.-M., and Meng, G. (2013). Dynamic characteristics of micro-beams considering the effect of flexible supports. *Sensors*, 13(12):15880–15897. 6.4

[Zhu and Chang, 2015] Zhu, Y. and Chang, T.-H. (2015). A review of microelectromechanical systems for nanoscale mechanical characterization. *Journal of Micromechanics and Microengineering*, 25(9):093001. 2.4

[Zine-El-Abidine and Yang, 2009] Zine-El-Abidine, I. and Yang, P. (2009). A tunable mechanical resonator. *Journal of Micromechanics and Microengineering*, 19(12):125004. 2.4